

# Development of a Mixed-Flow Compressor Impeller for Micro Gas Turbine Application

by  
Olaf Herbert Ferdinand Diener

*Thesis presented in partial fulfilment of the requirements for the degree  
of Master of Engineering (Mechanical) in the Faculty of Engineering at  
Stellenbosch University*



Supervisor: Dr. S.J. van der Spuy  
Co-supervisor: Dr. T. Hildebrandt  
Co-supervisor: Prof. T.W. von Backström

March 2016

## **DECLARATION**

By submitting this thesis electronically, I declare that the entirety of the work contained therein is my own, original work, that I am the sole author thereof (save to the extent explicitly otherwise stated), that reproduction and publication thereof by Stellenbosch University will not infringe any third party rights and that I have not previously in its entirety or in part submitted it for obtaining any qualification.

March 2016

Copyright © 2016 Stellenbosch University  
All rights reserved

## ABSTRACT

### **Development of a Mixed-Flow Compressor Impeller for Micro Gas Turbine Application**

O.H.F. Diener

*Department of Mechanical and Mechatronic Engineering, Stellenbosch  
University,  
Private Bag XI, Matieland 7602, South Africa  
Thesis: M. Eng. (Mech)*

March 2016

This thesis details the development of a mixed-flow compressor impeller to be used in a micro gas turbine (MGT) delivering 600 N thrust. Today's unmanned aerial vehicles (UAVs) demand high thrust-to-weight ratios and low engine frontal area. This combination may be achieved using mixed-flow compressors. The initial mixed-flow compressor impeller design was obtained using a 1-dimensional turbomachinery layout tool. A multi-point optimization of the impeller aerodynamic performance was completed. Thereafter a mechanical optimization was conducted to reduce mechanical stresses in the impeller. A coupled aero-mechanical (multi-disciplinary) optimization was concluded with the purpose of increasing the choke limit and reducing stresses while conserving aero-performance. Finally, a modal analysis was conducted and the rotor Campbell diagram was analysed to identify potential resonant conditions. The optimization process was set up and controlled in an integrated environment that includes a 3-dimensional Navier-Stokes flow solver and a 3-dimensional finite element (FE) structural solver. An artificial neural network (ANN) was used to generate a response surface based on a database of performance and geometric information. A genetic algorithm (GA) was applied to the response surface for optimization. The overall optimization process achieved an increase in total-to-total pressure ratio of 30.6% compared to the initial design while the isentropic total-to-total efficiency was increased by 5% at design conditions. The choke limit of the initial design was improved meaningfully. These values were obtained while also decreasing the peak von Mises stress to 30% below the material yield limit. Recommendations were made regarding the structural surroundings of the compressor and the operating speeds based on the Campbell diagram.

Keywords: micro gas turbine, mixed-flow compressor, multi-disciplinary optimization, Campbell diagram

## UITTREKSEL

### Ontwerp van 'n Gemengde-Vloei Mikrogasturbine Kompressorrotor

("Development of a Mixed-Flow Compressor Impeller for  
Micro Gas Turbine Application")

O.H.F. Diener

*Departement Meganiese en Megatroniese Ingenieurswese,  
Universiteit van Stellenbosch,  
Privaatsak XI, Matieland 7602, Suid-Afrika  
Tesis: M. Eng. (Meg)*

Maart 2016

Hierdie tesis beskryf die ontwikkeling van 'n gemengde-vloei kompressorrotor vir 'n mikrogasturbine wat 600 N dryfkrag lewer. Hedendaagse onbemande vliegtuie vereis 'n hoë dryfkrag-tot-gewig verhouding en 'n lae enjin frontale area. Hierdie kombinasie kan bereik word met behulp van gemengde-vloei kompressors. Die aanvanklike gemengde-vloei kompressorrotor-ontwerp is verkry deur 'n 1-dimensionale ontwerpkode. 'n Multi-punt optimering van die rotor se aerodinamiese vermoë is voltooi. Daarna is 'n meganiese optimering uitgevoer om spanning in die rotor te verminder. 'n Aero-meganiese (multidissiplinêre) optimering van die rotor is gedoen met die doel om die smoorperk te verhoog en die spanning te verminder, terwyl die aerodinamiese vermoë behoue bly. Laastens is 'n modale analise uitgevoer en die rotor se Campbell diagram geanaliseer om potensiële resonante toestande te identifiseer. Die optimeringsproses is opgestel en beheer in 'n geïntegreerde omgewing wat 3-dimensionale berekenings vloeidynamika en 3-dimensionale eindige element strukturele berekeninge uitvoer. 'n Kunsmatige neurale netwerk is gebruik om 'n reaksieoppervlakte te skep, gebaseer op 'n databasis van rotor vermoë en geometriese inligting. 'n Genetiese algoritme is toegepas op die reaksieoppervlakte vir die optimering. Die algehele optimeringsproses het 'n toename in die totaal-tot-totale drukverhouding van 30.6% in vergelyking met die aanvanklike ontwerp bereik, terwyl die isentropiese totaal-tot-totale benuttingsgraad verhoog was met 5%. Die smoorperk van die aanvanklike ontwerp is noemenswaardig verhoog. Hierdie waardes is behaal gesamentlik met die vermindering van die piek von Mises spanning tot 30% laer as die materiaal swiglimiet. Aanbevelings is gemaak ten opsigte van die strukturele omgewing van die kompressor en die bedryfspoed gebaseer op die resultate van die modale analise.

Sleutelwoorde: mikrogasturbine, gemengde-vloei compressor, multidissiplinêre optimering, Campbell diagram

## ACKNOWLEDGEMENTS

First and foremost, I would like to thank my supervisor, Dr van der Spuy, for his support and guidance I received during the course of this study. Additionally, I would like to thank him for providing me with the opportunity to travel to Germany as part of the thesis.

I gratefully acknowledge the experienced and insightful opinions, comments and tips I received from my co-supervisors, Prof. von Backström and Dr Hildebrandt, that allowed this thesis to be successful. Special thanks go to Dr Hildebrandt, for not only allowing me to complete part of the research at his company office in Germany, but also for welcoming me and inviting me to experience German hospitality. Furthermore, I thank him for making it possible for me to obtain a unique view of the CFD industry and also to gain some insight into the world of professional engineering.

Mr Sven Albert contributed a great deal to this research through his advice and insight, which is highly appreciated. I would also like thank the entire NIB team, who welcomed me in their ranks and made the research period in Germany such a great experience.

I would like to express my appreciation to CFturbo for allowing me to use their software for this research.

My thanks go to the CSIR; more specifically to Mr Radeshen Moodley, for his time and advice regarding the design of micro gas turbines and compressors.

Thank you to my friends in “die Lasraam” for the laughs and great discussions we had during tea time and any other random time.

This research would not have been possible without the funding I received. Many thanks go to the University Centre for Studies in Namibia (TUCSIN), who, in co-operation with the German Academic Exchange Service (DAAD), chose to support me and my research.

Finally, to my parents, my sincere appreciation, for their support provided during my time at Stellenbosch, and proof-reading the thesis.

**TABLE OF CONTENTS**

	<b>Page</b>
<b>DECLARATION .....</b>	<b>I</b>
<b>ABSTRACT.....</b>	<b>II</b>
<b>UITTREKSEL .....</b>	<b>III</b>
<b>ACKNOWLEDGEMENTS .....</b>	<b>IV</b>
<b>LIST OF FIGURES .....</b>	<b>IX</b>
<b>LIST OF TABLES .....</b>	<b>XII</b>
<b>NOMENCLATURE.....</b>	<b>XIV</b>
<b>1. INTRODUCTION .....</b>	<b>1</b>
1.1. BACKGROUND .....	1
1.2. OBJECTIVES .....	1
1.3. MOTIVATION .....	2
1.4. THESIS OUTLINE.....	2
<b>2. THEORY .....</b>	<b>3</b>
2.1. MICRO GAS TURBINES .....	3
2.2. MIXED-FLOW COMPRESSORS.....	4
2.2.1. <i>Pressure Ratio and Efficiency</i> .....	10
2.2.2. <i>Surge and Choke</i> .....	11
<b>3. THE COMPRESSOR DESIGN PROCESS .....</b>	<b>12</b>
<b>4. LITERATURE OVERVIEW .....</b>	<b>14</b>
4.1. MIXED-FLOW COMPRESSORS.....	14
4.2. COMPRESSOR ANALYSIS AND DESIGN .....	15
4.2.1. <i>Mean-Line Performance Analysis</i> .....	15
4.2.2. <i>3-dimensional Aerodynamic, Structural and Multi-disciplinary Analysis</i> .....	15
4.2.3. <i>3-dimensional Aerodynamic, Structural and Multi-disciplinary Optimization</i> .....	16
4.2.4. <i>3-dimensional Modal Analysis</i> .....	17
4.3. PREVIOUS WORK AT STELLENBOSCH UNIVERSITY (SU) .....	17
<b>5. REFERENCE MIXED-FLOW COMPRESSOR ANALYSIS.....</b>	<b>18</b>
5.1. GEOMETRY .....	18
5.2. COMPUTATIONAL DOMAIN AND DISCRETIZATION .....	19
5.3. CFD MODEL.....	21
5.3.1. <i>Fluid and Flow Model</i> .....	22

5.3.2.	<i>Boundary Conditions</i> .....	22
5.3.3.	<i>Numerical Model</i> .....	23
5.3.4.	<i>Initial Solution, Output and Convergence Criteria</i> .....	24
5.3.5.	<i>Post-processing</i> .....	25
5.4.	RESULTS .....	25
<b>6.</b>	<b>INITIAL IMPELLER DESIGN .....</b>	<b>26</b>
6.1.	PERFORMANCE AND SIZE SPECIFICATIONS .....	26
6.2.	MEAN-LINE DESIGN .....	27
6.2.1.	<i>Approach</i> .....	28
6.2.2.	<i>Computational Domain and Discretization</i> .....	29
6.2.3.	<i>Impeller Performance Evaluation</i> .....	31
6.2.4.	<i>CFD Model</i> .....	31
6.2.5.	<i>Results</i> .....	32
6.3.	CONCLUSION .....	34
<b>7.</b>	<b>AERODYNAMIC OPTIMIZATION .....</b>	<b>35</b>
7.1.	THE OPTIMIZATION PROCESS .....	35
7.2.	PARAMETERIZATION.....	37
7.2.1.	<i>Endwalls</i> .....	38
7.2.2.	<i>Stream Surfaces</i> .....	38
7.2.3.	<i>Stacking Laws</i> .....	38
7.2.4.	<i>Main Blade Camber Curve and Side Curves</i> .....	39
7.3.	FITTING .....	40
7.4.	PARAMETER VALUE BOUNDS .....	41
7.5.	OPERATING POINTS .....	42
7.6.	POST-PROCESSING .....	44
7.7.	DATABASE GENERATION .....	44
7.7.1.	<i>Grid Toughness and Quality</i> .....	44
7.7.2.	<i>Numerical Model</i> .....	46
7.7.3.	<i>Results</i> .....	46
7.8.	OPTIMIZATION.....	48
7.8.1.	<i>Optimization Settings and Objective Function Definition</i> .....	48
7.8.2.	<i>Numerical Model</i> .....	50
7.8.3.	<i>Results</i> .....	50
7.9.	CONCLUSION .....	53
<b>8.</b>	<b>MECHANICAL OPTIMIZATION .....</b>	<b>54</b>
8.1.	PARAMETERIZATION.....	55
8.2.	DISCRETIZATION .....	56

8.3.	FE MODEL.....	57
8.4.	IMPELLER BACKFACE AND BORE.....	57
8.4.1.	<i>Database Generation</i> .....	58
8.4.2.	<i>Results</i> .....	58
8.5.	IMPELLER BLADE .....	59
8.5.1.	<i>Database Generation</i> .....	59
8.5.2.	<i>Optimization Settings and Objective Function Definition</i> .....	59
8.5.3.	<i>Optimization and Results</i> .....	60
8.6.	CONCLUSION .....	62
<b>9.</b>	<b>COUPLED AERO-MECHANICAL OPTIMIZATION.....</b>	<b>63</b>
9.1.	DATABASE GENERATION .....	63
9.2.	OPTIMIZATION SETTINGS AND OBJECTIVE FUNCTION DEFINITION .....	64
9.3.	RESULTS .....	65
9.4.	ERRORS AND UNCERTAINTY .....	70
9.5.	CONCLUSION .....	71
<b>10.</b>	<b>ROTOR DYNAMIC ANALYSIS.....</b>	<b>72</b>
10.1.	LINEAR STATIC FEA VALIDATION .....	72
10.1.1.	<i>SimXpert FE Model and Simulation Procedure</i> .....	72
10.1.2.	<i>Results</i> .....	73
10.2.	MODAL ANALYSIS .....	75
10.2.1.	<i>FE Model</i> .....	75
10.2.2.	<i>Results</i> .....	75
<b>11.</b>	<b>CONCLUSION AND RECOMMENDATIONS.....</b>	<b>79</b>
11.1.	RECOMMENDATIONS .....	80
11.2.	FUTURE WORK.....	81
	<b>REFERENCES.....</b>	<b>82</b>
	<b>APPENDIX A: THEORY AND SOFTWARE.....</b>	<b>87</b>
A.1	COMPUTATIONAL FLUID DYNAMICS (CFD) .....	87
A.1.1	<i>Reynolds-Averaged Navier-Stokes (RANS) Equations</i> .....	87
A.1.2	<i>Turbulence Modelling</i> .....	87
A.2	FINITE ELEMENT ANALYSIS (FEA) .....	88
A.2.1	<i>Linear Static Analysis</i> .....	88
A.2.2	<i>Rotor Dynamics and Modal Analysis</i> .....	88
A.3	SOFTWARE .....	91
A.3.1	<i>CFturbo</i> .....	91
A.3.2	<i>NUMECA</i> .....	91

A.3.3 MSC SimXpert and Nastran.....	94
<b>APPENDIX B: MATLAB IN-HOUSE CODE FLOWCHART .....</b>	<b>95</b>
<b>APPENDIX C: CFTURBO SETTINGS .....</b>	<b>96</b>
<b>APPENDIX D: COMPRESSOR IMPELLER PERFORMANCE                   EVALUATION .....</b>	<b>98</b>
<b>APPENDIX E: CFD AND FEA GRID DETAILS AND DEPENDENCY ...</b>	<b>100</b>
E.1 REFERENCE COMPRESSOR STAGE GRID .....	100
E.2 GRID USED FOR THE INITIAL CFTURBO DESIGN AS WELL AS DB01 AND DB02 .....	101
E.3 DB03, AERODYNAMIC OPTIMIZATION AND COUPLED OPTIMIZATION CFD GRID.....	103
E.4 HEXPRESS <sup>TM</sup> /HYBRID FEA GRID SETTINGS .....	104
<b>APPENDIX F: Y-PLUS VALUES .....</b>	<b>106</b>
<b>APPENDIX G: NUMECA AUTOBLADE DESIGN SPACE.....</b>	<b>107</b>
<b>APPENDIX H: DOE IMPELLER PARAMETERS .....</b>	<b>108</b>
H.1 PARAMETRIC MODEL OVERVIEW .....	108
H.2 AERODYNAMIC OPTIMIZATION: FREE PARAMETERS.....	108
H.3 AERODYNAMIC OPTIMIZATION: FROZEN PARAMETERS .....	109
<b>APPENDIX I: OBJECTIVE FUNCTIONS .....</b>	<b>111</b>
<b>APPENDIX J: SHAFT STRESS CALCULATIONS .....</b>	<b>112</b>
<b>APPENDIX K: MERIDIONAL VELOCITIES AND B2B RELATIVE                   MACH NUMBERS IN COMPARISON.....</b>	<b>113</b>
<b>APPENDIX L: PROCESSOR MANAGEMENT AND CPU TIME.....</b>	<b>115</b>
L.1 CFD DATABASE AND OPTIMIZATION .....	115
L.1.1 Database .....	115
L.1.2 Optimization.....	115
L.2 OOFELIE FEA.....	116
L.3 COUPLED OPTIMIZATION.....	116
<b>APPENDIX M: BLADE CAMBER ANGLE COMPARISON .....</b>	<b>117</b>
<b>APPENDIX N: FINAL IMPELLER PERFORMANCE MAP .....</b>	<b>118</b>
<b>APPENDIX O: INITIAL AND FINAL IMPELLER RENDER .....</b>	<b>119</b>

**LIST OF FIGURES**

	<b>Page</b>
Figure 1: Micro gas turbine components (Pichlmeier, 2010) .....	3
Figure 2: Mollier diagram of a typical centrifugal compressor stage (adapted from Dixon, 1998) .....	5
Figure 3: Different compressor rotor types (CFturbo, 2015).....	7
Figure 4: Compressor components in the meridional plane .....	8
Figure 5: Velocity triangles of a mixed-flow compressor impeller.....	9
Figure 6: Typical compressor map (Dixon, 1998).....	11
Figure 7: Compressor impeller design procedure.....	13
Figure 8: Reference compressor stage meridional contours and traces.....	18
Figure 9: 3D grid lines on hub and blades of the reference stage (2 <sup>nd</sup> multigrid level) .....	21
Figure 10: Boundary patches of the reference compressor stage .....	23
Figure 11: Reference stage performance curves in contrast .....	25
Figure 12: Mean-line calculations according to Aungier (2000) compared with CFD results of a mixed-flow impeller design obtained from the in-house MATLAB code .....	28
Figure 13: Meridional view of a CFturbo design with hub nose and diffuser passage.....	30
Figure 14: Computational domain enclosed by hub, shroud, inlet and outlet .....	30
Figure 15: 3-dimensional grid projections on the 2 <sup>nd</sup> multi-grid level of a CFturbo design.....	31
Figure 16: Results of designs generated using CFturbo .....	33
Figure 17: The optimization process in FINE <sup>TM</sup> /Design3D .....	37
Figure 18: Parameterization of the hub and shroud contours (endwalls) .....	39
Figure 19: Section 1 and 2 camber Bézier points and associated freedom.....	40
Figure 20: Meridional contours and traces of randomly generated geometries ....	42
Figure 21: B2B views of possible blade shapes at section 1 (hub).....	42
Figure 22: CFturbo compressor performance curves and chosen operating points for optimization (evaluation at $r = 55.5$ mm) .....	43
Figure 23: Comparison of mass-averaged total pressures at different radii with different TE topology .....	45

Figure 24: Results of the designs from the final CFD database .....	47
Figure 25: ANN convergence of the CFD optimization.....	51
Figure 26: Initial fitted and optimized blade geometry at section 1 and 2 .....	51
Figure 27: Comparison of initial and optimized meridional contours and locations .....	52
Figure 28: Initial and optimized design performance curves at design speed .....	53
Figure 29: Parameterization of the impeller solid sector in the meridional plane .....	55
Figure 30: Various geometries obtained in the impeller backface database.....	58
Figure 31: Initial backface design (left) and best database result.....	59
Figure 32: Hub and shroud blade thickness of the aero-optimized and mechanically optimized designs .....	61
Figure 33: VM stresses of the aero-optimized design (left) and the mechanically optimized design with $r_{fil} = 1.85$ mm .....	61
Figure 34: Relative Mach number distribution in the meridional plane at choke .....	65
Figure 35: Final design vs. CFturbo and aero-optimized designs at 95 krpm .....	67
Figure 36: The mechanically optimized design with $r_{fil} = 1.85$ mm (left) compared to the design resulting from the shroud camber and backface optimization .....	67
Figure 37: Blade profiles of the aero-optimized design and the aero-mechanically optimized design.....	69
Figure 38: Relative Mach number contours of the CFturbo design (left) and the final optimized design at 90% span and design conditions .....	69
Figure 39: Comparison of OOFELIE (left) and SimXpert equivalent stress results .....	74
Figure 40: Different mode shape groups: main blade (left), splitter blade (middle) and combined.....	76
Figure 41: Compressor rotor Campbell diagram (SimXpert 2).....	77
Figure 42: Campbell diagram and associated damped vibration amplitude (Boyce, 2002).....	90
Figure 43: Construction of the $dm/r-\theta$ plane (Verstraete <i>et al.</i> , 2010) .....	93
Figure 44: Flow chart of the in-house mean-line compressor design code (van der Merwe, 2012) .....	95
Figure 45: Inlet bulb mesh topology of the reference stage .....	100
Figure 46: Main blade (top) and splitter blade grid points of reference impeller .....	101
Figure 47: Grid point distribution of reference diffuser .....	101

Figure 48: Main blade (top) and splitter blade grid points of initial design, database and optimization grid .....	102
Figure 49: CFturbo (initial) impeller design grid independence study results ....	103
Figure 50: Grid independence study results of the grid used for DB03, OPT14 and all subsequent CFD simulations .....	104
Figure 51: NUMECA AutoBlade™ design space .....	107
Figure 52: Meridional velocity contours of the CFturbo (left) and final design .	113
Figure 53: Relative Mach number contours at design conditions and 10% span of the CFturbo design (left) and the final design .....	113
Figure 54: Relative Mach number contours at design conditions and 50% span of the CFturbo design (left) and the final optimized design .....	114
Figure 55: Blade camber angles of the initial, aero-optimized and aeromechanically optimized design .....	117
Figure 56: Compressor map of the final compressor impeller design .....	118
Figure 57: Side view of the baseline (left) and final impeller design (not to scale) .....	119
Figure 58: Isometric view of the baseline (left) and final impeller designs .....	119

**LIST OF TABLES**

	<b>Page</b>
Table 1: Important grid defining dimensions of the reference stage .....	19
Table 2: Reference compressor stage mesh quality .....	20
Table 3: Ideal (perfect) gas properties of air.....	22
Table 4: Boundary conditions of the reference compressor stage .....	23
Table 5: Reference stage numerical model details .....	24
Table 6: Compressor stage specifications and anticipated impeller specifications .....	26
Table 7: Machine type according to specific speed (CFturbo, 2014).....	29
Table 8: Boundary conditions used for the CFturbo designs.....	32
Table 9: Comparison of various mixed-flow compressor impellers.....	34
Table 10: Operating points chosen for the CFD database and optimization .....	44
Table 11: Final CFD database grid quality .....	45
Table 12: Numerical model for databases DB01, DB02 and DB03 .....	46
Table 13: Imposed quantity values for the CFD optimization objective function.....	49
Table 14: CFturbo, best database design and optimized design performance comparison at HEP.....	52
Table 15: Various potential impeller materials and their properties .....	57
Table 16: Summary of design steps and effects on performance .....	62
Table 17: Imposed quantity values for the coupled optimization objective function .....	64
Table 18: Summary of important design parameters.....	68
Table 19: SimXpert linear static FEA mesh independence study results .....	73
Table 20: Linear static simulation result comparison.....	73
Table 21: Pre-stressed modal analysis results at 95 krpm .....	76
Table 22: Possible resonant conditions obtained from the Campbell diagram.....	78
Table 23: Specified and obtained impeller performance quantities .....	80
Table 24: Important grid defining dimensions of the initial design .....	102
Table 25: Final CFturbo design mesh quality.....	103
Table 26: Automatic grid generation settings in FINE <sup>TM</sup> /Design3D .....	105
Table 27: Maximum wall-y +values for important impeller designs at HEP .....	106

Table 28: Parametric model overview .....	108
Table 29: Objective function definition of the aerodynamic optimization with balanced penalty values according to the given quantity value .....	111
Table 30: Objective function definition of the coupled optimization with penalty values according to the given quantity value .....	111
Table 31: CFD database and optimization computational time.....	116

**NOMENCLATURE****Symbols**

$A$	Area perpendicular to the flow	(m <sup>2</sup> )
$b$	Hub-to-shroud height	(m)
$C$	Absolute fluid velocity	(m/s)
$c$	Speed of sound	(m/s)
$c_p$	Specific heat at constant pressure	(J/kg.K)
$dm$	Meridional length along meridional co-ordinate $m$	(-)
$\overrightarrow{dS}$	Surface vector differential	(m <sup>2</sup> )
$F$	Objective function value	(-)
$f$	Frequency	(Hz)
$H$	Head	(m)
$h$	Specific enthalpy	(J/kg)
$I$	Rothalpy	(J/kg)
$k$	Penalty term exponent	(-)
$Ma$	Mach number	(-)
$m$	Meridional co-ordinate, mass flow rate	(-), (kg/s)
$N$	Rotational speed	(rpm)
$n$	Station or state, engine order	(-), (-)
$p$	Pressure	(Pa)
$Q$	Volumetric flow rate	(m <sup>3</sup> /s)
$q$	Quantity value	()
$R$	Specific gas constant	(J/kg.K)
$Re$	Reynolds number	(-)
$r$	Radius, radial co-ordinate	(m), (-)
$s$	Entropy	(J/kg.K)
$T$	Temperature	(K)
$U$	Blade velocity	(m/s)
$V$	Velocity	(m/s)
$W$	Relative fluid velocity	(m/s)

$\dot{W}$	Work done	(W)
$w$	Weight factor	(-)
$\vec{w}$	Weight vector	(-)
$y^+$	Dimensionless wall distance	(-)
$z$	Axial co-ordinate	(-)
$x$ - $y$ - $z$	Cartesian co-ordinates	(-)

### Greek symbols

$\alpha_{c2}$	Impeller meridional exit angle	(°)
$\beta$	Blade camber angle	(°)
$\gamma$	Specific heat ratio	(-)
$\eta$	Isentropic efficiency	(-)
$\theta$	Tangential co-ordinate	(°)
$\nu$	Kinematic viscosity	(m <sup>2</sup> /s)
$\nu_t$	Turbulent kinematic viscosity	(m <sup>2</sup> /s)
$\Pi$	Pressure ratio	(-)
$\rho$	Density	(kg/m <sup>3</sup> )
$\sigma_{VM,max}$	Maximum von Mises stress	(MPa)
$\tau_A$	Torque around an axis A-A	(N.m)
$\omega$	Rotational speed	(rad/s)

### Subscripts

0	Compressor inlet
0n	Stagnation condition
1	Impeller inlet
2	Impeller outlet
3	Diffuser outlet
<i>choke</i>	Choke conditions
<i>design</i>	Specified design condition
<i>fil</i>	Fillet
<i>HEP</i>	Highest efficiency point
h	Hub

<i>imp</i>	Impeller, imposed value
<i>m – l</i>	Mean-line
<i>o</i>	Highest efficiency point on operating line
<i>out</i>	Domain outlet
<i>in</i>	Domain inlet
<i>ref</i>	Reference quantity
<i>T – T</i>	Total-to-total
<i>s</i>	Shroud, isentropic process, stall condition
<i>stage</i>	Quantity evaluated across the compressor stage
<i>r, <math>\theta</math>, z</i>	Cylindrical co-ordinates

### **Abbreviations**

ANN	Artificial neural network
ASME	American Society of Mechanical Engineers
B2B	Blade-to-blade
BC	Boundary condition
CAD	Computer aided design
CFD	Computational fluid dynamics
CFL	Courant-Friedrichs-Lewi
CP	Choke point
CPU	Central processing unit
CSIR	Council for Scientific and Industrial Research
DoE	Design of experiments
DP	Design point
EO	Engine order
FE	Finite element
FEA	Finite element analysis
FEM	Finite element method
FV	Finite volume
GA	Genetic algorithm
GUI	Graphical user interface
HEP	Highest efficiency point

LE	Leading edge
MB	Main blade
SB	Splitter blade
SP	Surge point
SST	Shear stress transport
MDO	Multi-disciplinary optimization
MGT	Micro gas turbine
MSC	MacNeil-Schwendler Corporation
NACA	National Advisory Committee for Aeronautics
NASA	National Aeronautics and Space Administration
NIB	NUMECA Ingenieurbüro
NINT	NUMECA International
RAM	Random access memory
RANS	Reynolds-averaged Navier-Stokes
SA	Spalart-Allmaras
SM	Surge margin
TE	Trailing edge
UAV	Unmanned aerial vehicle
VM	Von Mises

## 1. INTRODUCTION

Micro gas turbines (MGTs) find increased interest in application for the propulsion of unmanned aerial vehicles (UAVs) due to their high thrust-to-weight-ratio (Benini and Giacometti, 2007). Especially in the United States (US) a large demand exists for economical MGTs designed to power UAVs, according to the US National Research Council (2010), citing an investment of US\$50 billion to US\$100 billion in gas turbine research and investment over the past five decades. The application of MGTs in portable and backup power generation is also becoming attractive (Vick *et al.*, 2010).

This thesis aimed to develop a mixed-flow compressor impeller (rotor) to be used in a MGT providing 600 N thrust. Mixed-flow compressors share the advantages of axial and centrifugal compressors: a relatively high mass flow rate per unit frontal area may be achieved along with a high pressure ratio in a single stage (Eisenlohr and Benfer, 1993). These characteristics may be exploited for use in MGTs powering UAVs, where size and weight play an important role along with performance.

The initial impeller design is obtained using a 1-dimensional turbomachinery layout tool. An optimization of the impeller aerodynamic performance using computational fluid dynamics (CFD) follows. Finite element methods (FEM) are consequently applied to optimize the mechanical stresses in the impeller. A coupled aero-mechanical optimization is completed to ensure that an increase in aero-performance does not lead to higher mechanical stresses and aero-performance is not sacrificed when stresses are reduced. Finally, a modal analysis of the rotor is conducted and a Campbell diagram of the rotor is analysed to identify potential resonant conditions.

### 1.1. Background

The LEDGER university research program was introduced by the South African Department of Defence to revive defence-related research at tertiary institutions. The aeronautics branch of LEDGER is made up of two projects. One project, called BALLAST, aims to attend to the advancement of skills in gas turbine technology (LEDGER University Research Program, 2014). This thesis falls under the BALLAST project. The project is managed by the Council for Scientific and Industrial Research (CSIR). The research presented herein was funded by the German Academic Exchange Service (DAAD) in partnership with the University Centre for Studies in Namibia (TUCSIN).

### 1.2. Objectives

The main objectives of the project are the following:

- Complete an extensive literature study on the design of mixed-flow compressors.
- Formulate a design approach.
- Optimise a mixed-flow compressor impeller design obtained from a 1-dimensional mean-line design code using CFD.
- Verify the structural integrity of the impeller using FEA.

### 1.3. Motivation

An increased interest in the application of MGTs to the military and civil sectors makes the development of such an engine and its components a viable project. The success experienced by the Hamilton Sundstrand TJ-50 MGT (Harris *et al.*, 2003) with its mixed-flow compressor stage adds to the motivation for the development of such a machine.

The development of small turbomachines has a distinct academic advantage: students have the possibility to be involved with the manufacture and testing of the parts, giving them exposure to the full product development cycle.

### 1.4. Thesis Outline

The thesis is divided into seven major parts:

- Theory
- Design process
- Literature
- Reference impeller analysis
- Initial design
- Optimization
- Rotor dynamic analysis

The applicable theory related to the activities in this thesis is illustrated in the first part. A general understanding of the function and theory of mixed-flow compressors is conveyed. An overview of the design process is presented next. Thereafter, the literature on the relevant themes is discussed. The performance of a reference mixed-flow compressor stage is consequently analysed using the CFD analysis tools chosen for the design presented in this thesis. This step proves the author's capability to operate the numerical analysis software.

Following the CFD analysis of the reference compressor stage, the initial impeller design is presented. It was generated using a 1-dimensional mean-line turbomachinery layout tool. Part 6 of the thesis is split into three design steps involving a 3-dimensional optimization: an aerodynamic, mechanical and a coupled aero-mechanical optimization are conducted. An investigation into the rotor dynamics using the results of a modal analysis concludes the thesis.

## 2. THEORY

A theoretical background regarding the operation of MGTs and the associated compressor stages is provided in this chapter. Different compressor impeller types and their associated differences are explained. Important geometric features of a mixed-flow compressor impeller are clarified. The physical laws governing the operation of the compressor are indicated. Theoretical analysis relations help to explain the operation of a compressor impeller.

### 2.1. Micro Gas Turbines

The compressor forms part of a micro gas turbine, which is a compact form of a jet engine. The fundamental mechanism of a jet engine can be explained using Newton's 2<sup>nd</sup> and 3<sup>rd</sup> law: conservation of momentum yields a net reactive force (thrust) acting on the given geometry due to combustion gases accelerating in the opposite direction (Hill and Peterson, 1992).

A compressor is responsible for increasing the pressure of air entering the machine and thereby making combustion more effective. Fuel is added to the air after exiting the compressor stage and the air-fuel mixture is ignited in the combustion chamber. The combustion gases enter a turbine which drives the compressor. A major part of the thrust is generated as the gases exit the turbine and accelerate through a nozzle, forming a jet. The aforementioned components are shown in Figure 1. In modern jet engines for airliners a large amount of air (by mass), circumvents the gas generator core. These engines are called by-pass engines in which the majority of thrust is generated through bypass air.

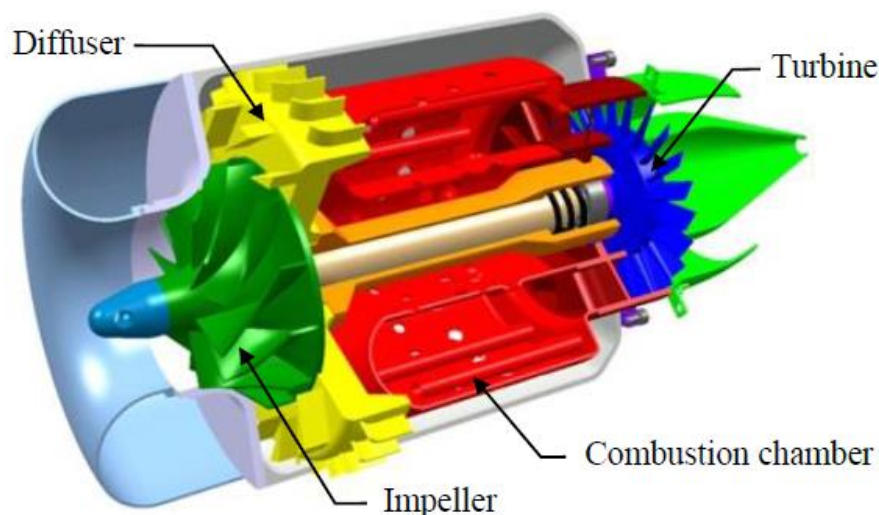


Figure 1: Micro gas turbine components (Pichlmeier, 2010)

## 2.2. Mixed-flow Compressors

The flow in a compressor rotor is governed by the following four physical laws:

- continuity (conservation of mass)
- Newton's 2<sup>nd</sup> law (conservation of momentum)
- the 1<sup>st</sup> law of thermodynamics (conservation of energy)
- the 2<sup>nd</sup> law of thermodynamics

The following summary of the governing equations was taken from Dixon (1998). In a 1-dimensional steady flow analysis the mass flow rate  $m$  is constant in the general flow direction from point 1 to point 2:

$$m = \rho_1 C_1 A_1 = \rho_2 C_2 A_2 \quad (2.1)$$

where  $C_1$  and  $C_2$  are the fluid velocities at point 1 and 2 respectively. In a control volume angular momentum around an arbitrary axis A-A is conserved:

$$\sum \tau_A = m(r_2 C_{\theta 2} - r_1 C_{\theta 1}) \quad (2.2)$$

$C_{\theta 1}$  and  $C_{\theta 2}$  represent the tangential velocity at point 1 and 2 respectively. The right-hand side of Equation 2.2 is a result of having assumed steady flow and uniform velocity at point 1 and 2. The work done on the fluid by a pump or compressor is then

$$\dot{W}_{comp} = \tau_A \omega = m(U_2 C_{\theta 2} - U_1 C_{\theta 1}) \quad (2.3)$$

where  $U = \omega r$  is the blade speed at radius  $r$ . Equation 2.3 is referred to as Euler's pump equation.

Under typical operating conditions the rothalpy,  $I$ , is conserved from entry to exit in a compressor:

$$I = h_1 + \frac{1}{2} C_1^2 - U_1 C_{\theta 1} = h_2 + \frac{1}{2} C_2^2 - U_2 C_{\theta 2} \quad (2.4)$$

For adiabatic flows (no heat transfer from or to the surroundings), in which a change in elevation is negligibly small, the steady flow energy equation boils down to:

$$\dot{W}_{comp} = m(h_{02} - h_{01}) \quad (2.5)$$

The 2<sup>nd</sup> law of thermodynamics states that, for a fluid undergoing a state change from state 1 to state 2 with the flow being steady and 1-dimensional, the process is reversible if the entropy stays constant:

$$s_1 = s_2 \quad (2.6)$$

A process behaving according to Equation 2.6 is called an isentropic process. In a real process some energy is always lost as energy not available to do any work, meaning there is an increase in entropy during the process. Figure 2 shows the changes in heat content (enthalpy) with entropy of a gas in a typical centrifugal compressor stage. This chart is commonly called a Mollier diagram. The bold, red line follows the static enthalpy states of the gas.

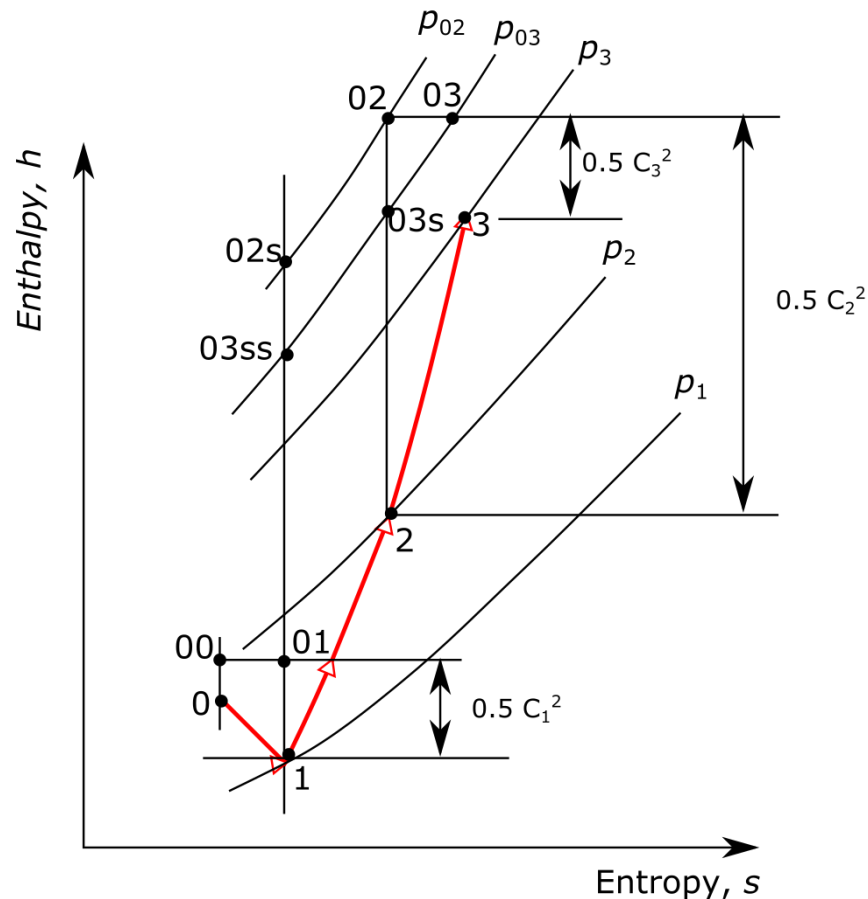


Figure 2: Mollier diagram of a typical centrifugal compressor stage (adapted from Dixon, 1998)

A stagnation condition is denoted by a subscript 0 which appears before the subscript number representing the state (or station). If only one subscript is present, it implies a static condition. It should be noted that in this study any differences in elevation can be ignored and thus the stagnation conditions equal the total (static, dynamic and hydrostatic part) conditions.

Stagnation enthalpy is defined at any state,  $n$ , as the sum of the static and dynamic of enthalpy components:

$$h_{0n} = h_n + \frac{1}{2} C_n^2 \quad (2.7)$$

The gas is accelerated in the inlet casing from state 0 to state 1, where the stagnation enthalpy stays constant. Next, the impeller imparts energy on the gas from state 1 to state 2, increasing static and stagnation enthalpy. Thereafter the diffuser recovers static pressure from state 2 to state 3 the while stagnation enthalpy does not change. The stagnation enthalpy stays constant from states 0 to 1 and 2 to 3 as no shaft work has been done and steady, adiabatic flow is assumed. For constant specific heats and a perfect gas behaving according to the ideal gas law

$$\frac{p}{\rho} = RT \quad (2.8)$$

the following is true

$$h_2 - h_1 = c_p(T_2 - T_1) \quad (2.9)$$

and the following equation relates the pressures at two different states (pressure ratio) to the temperatures at the same states if the process undergone from state 1 to state 2 was isentropic (Dixon, 1998:18):

$$\frac{p_{02}}{p_{01}} = \left( \frac{T_{02s}}{T_{01}} \right)^{\frac{\gamma}{\gamma-1}} \quad (2.10)$$

where  $\gamma$  is the specific heat ratio which can usually be safely taken as constant (White, 1998).

In a centrifugal compressor the pressure of a gas is raised significantly by increasing the radius of the mean flow-path (Eisenlohr and Benfer, 1993). The increased radius results in a higher blade speed  $U_2$  compared to  $U_1$  along the flow-

path, which leads to an increased circumferential speed  $C_{\theta 2}$  of the gas. Referring back to the Euler pump equation (Equation 2.3),  $U_2 C_{\theta 2}$  would be significantly larger than  $U_1 C_{\theta 1}$ , which leads to high work input and thus a high potential pressure ratio. This is not the case in an axial compressor rotor, where the radius of the mean flow-path does not change and therefore  $U_1$  and  $U_2$  stay constant along the flow path.

In an axial compressor the circumferential velocity  $C_{\theta 2}$  of the gas is increased only by turning the flow along a flow path. For an axial compressor to achieve an equivalent pressure ratio of a centrifugal compressor for the same frontal area, several compressor stages are necessary, where each stage comprises of a rotor and a stator. The axial length of an axial compressor is thus much larger than that of a centrifugal compressor with an equivalent pressure ratio. However, the radial space of a centrifugal machine required is larger due to the need for a diffuser downstream of the impeller. A diffuser decelerates the gas and has an increasing cross-sectional area along the flow path in order to obtain the maximum possible pressure rise before the gas enters the combustion chamber.

A compromise between the pressure ratio, radial and axial space and therefore the mass flow capabilities per unit frontal area can be found in a mixed-flow compressor impeller. A mixed-flow compressor directs the flow partly into the radial direction and partly into the axial direction, as shown in the meridional ( $z$ - $r$ ) plane in Figure 3.

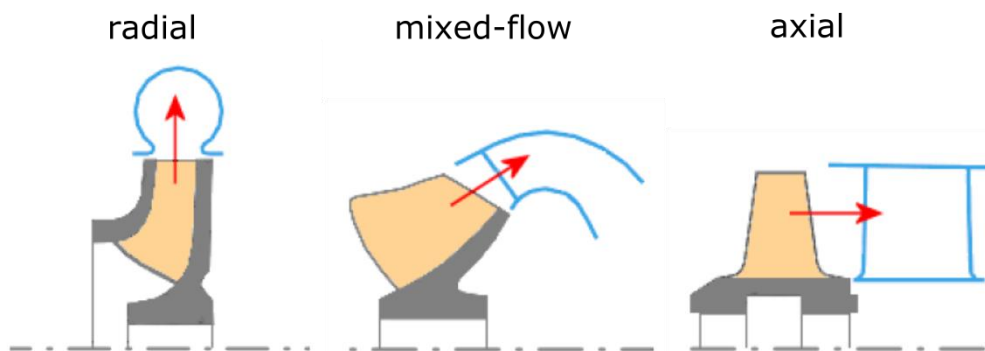


Figure 3: Different compressor rotor types (CFturbo, 2015)

The main entities of the geometry of a turbomachine are defined in the  $z$ - $r$  plane, which is also called the meridional plane. By revolving the curves defined in the  $z$ - $r$  plane around the axis of rotation ( $z$ -axis) the 3-dimensional shape of the turbomachine is formed. In the meridional plane the hub, shroud, main- and splitter blade leading edge (LE) and trailing edge (TE) shapes are defined. The blades are attached to the hub and span from the hub to the tip gap. The tip gap prevents the moving blades from coming into contact with the casing. The casing above the tip of the blades is called the shroud. Important features of a compressor impeller are shown in the meridional plane in Figure 4. Symbols defined are the

impeller tip hub-to-shroud height  $b_2$ , the meridional exit angle  $\alpha_{c2}$  and the hub (subscript h) and shroud (subscript s) radii at impeller inlet (subscript 1) and outlet (subscript 2).

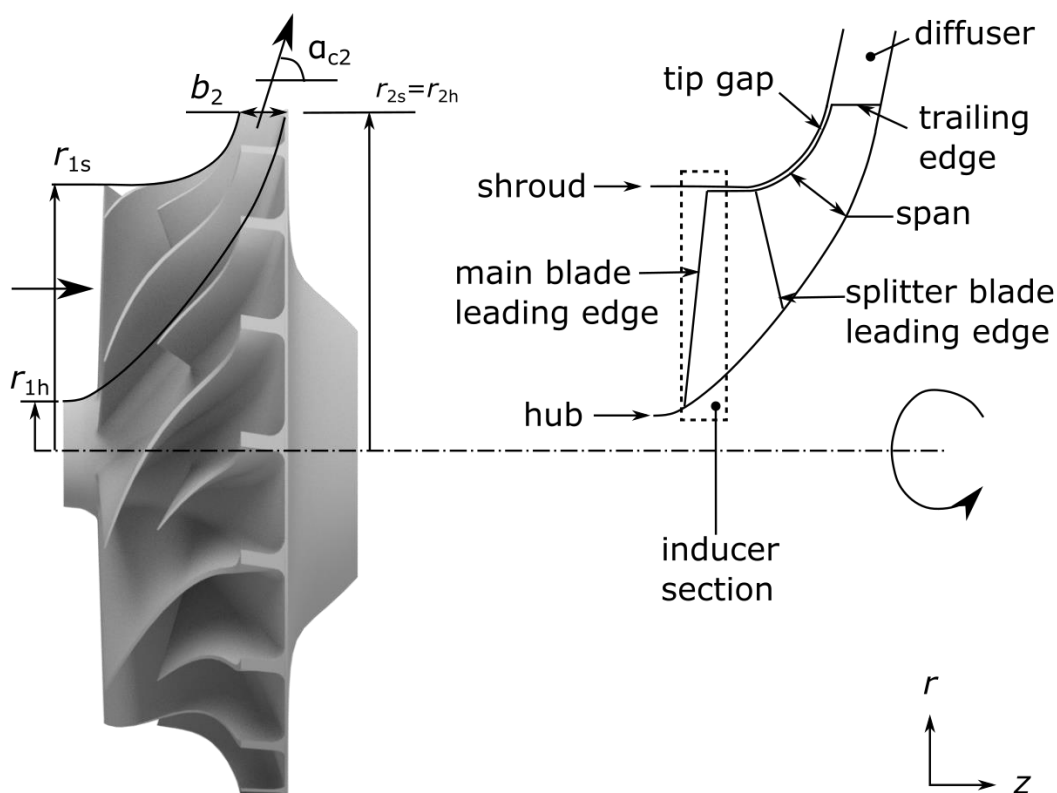


Figure 4: Compressor components in the meridional plane

The inlet section of the impeller is called the impeller eye or inducer. Here the leading edge of the main blade “scoops up” the atmospheric air at a relative fluid velocity  $W_1$ , an absolute velocity  $C_1$  and a blade tip velocity  $U_1$  and directs it towards the blade passage. The air may approach the inducer with a pure axial velocity ( $C_1 = C_{z1}$ ) or with an added tangential component (whirl). After the flow has been aligned with the blades it is accelerated and moves along the blade passage. The pressure and temperature experience an increase from inlet to outlet through the work imparted by the impeller.

At the impeller outlet the air leaves the TE blade surface and proceeds towards the diffusing section of the machine. In case of a mixed-flow compressor impeller, the absolute impeller exit velocity  $C_2$  has a radial ( $C_{r2}$ ), axial ( $C_{z2}$ ) and tangential ( $C_{\theta 2}$ ) component. The flow does not leave the blades exactly at the blade angle  $\beta_2$  due to a phenomenon called slip. Slip is responsible for decreasing the ideal  $C_{\theta 2}$  by  $\Delta C_{\theta 2}$ . The blade loading, which in a centrifugal impeller is mostly due to Coriolis acceleration, is required to shrink towards the TE. As a consequence there is no means to ensure that the flow is perfectly guided (Cumpsty, 1989). The velocity triangles of a mixed-flow impeller are shown in Figure 5.

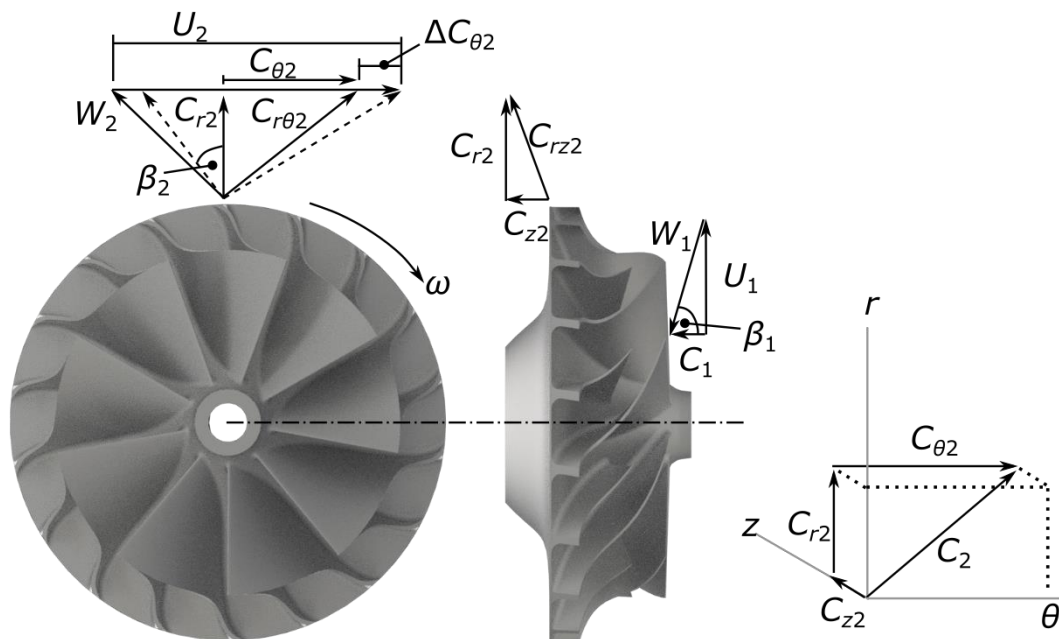


Figure 5: Velocity triangles of a mixed-flow compressor impeller

By changing the outlet angle from a radial direction (centrifugal impeller) to a mixed-flow scenario, the Coriolis force is relaxed, reducing slip. The degree to which the Coriolis force is relaxed depends on the change in radius of the mean flow path as well as the meridional exit angle  $\alpha_{C2}$ . In literature meridional exit angles of mixed-flow compressors range from  $22^\circ$  to  $65^\circ$  (Mönig *et al.*, 1993), (Kano *et al.*, 1984) (Harris *et al.*, 2003) (Cevic and Uzol, 2011) (Rajakumar *et al.*, 2013). The lean towards the axial direction means a lower frontal area may be achieved compared to centrifugal compressors, since it facilitates the transition of the flow channel towards the axial. The axial length of the mixed-flow impeller is, however, usually higher than that of a centrifugal impeller (Niculescu *et al.*, 2007).

Centrifugal impellers frequently feature main blades as well as splitter blades. Splitter blades are usually a truncated section of the main blade. They help reduce the blade loading on the individual blades towards the impeller outlet while potentially increasing the mass flow capabilities at the throat of the inducer (Cumpsty, 1989) (Japikse, 1996) (Aungier, 2000). The blade geometry cannot be fully defined in the meridional plane. At a specified span, the blade profile may be described by either using the pressure and suction side definitions in space or the camber line and a corresponding thickness distribution. In a NUMECA \*.geomTurbo file, which contains all the geometric data necessary for meshing, the blade pressure and suction sides are defined as points in  $x$ - $y$ - $z$  or  $r$ - $\theta$ - $z$  space. The camber line is usually defined in the  $dm/r$ - $\theta$  plane beforehand and mapped to  $x$ - $y$ - $z$  space. More information on the  $dm/r$ - $\theta$  plane, also called the blade-to-blade (B2B) plane, is given in Appendix A.

The blade profiles have to adhere to certain prerequisites of an acceptable flow field, for example gradual changes in camber curvature, which facilitate boundary layer attachment. Blade sweep is an important geometric feature of an impeller blade. The blade sweep angle  $\beta_2$  is the blade angle at the TE in the  $r-\theta$  (and  $dm/r-\theta$ ) plane at a specific span-wise location. It may be constant along the span, which is assumed in mean-line calculations, or differ along the span. Backsweep, meaning a sweep angle opposite to the direction of rotation, is likely to reduce impeller exit Mach number (Eisenlohr and Benfer, 1993) and ensure a higher efficiency and less work input necessary for the same mass flow rate (Cumpsty, 1989). Another geometric blade feature is the blade-lean. The blade-lean is defined by the angle of the blade cross-section to the tangential if viewed in the  $z-\theta$  plane.

### 2.2.1. Pressure Ratio and Efficiency

Considering that radial and mixed-flow compressors are used to increase the static and dynamic properties of the fluid, it is useful to define the total-to-total pressure ratio as an indicator of performance. A total-to-total measure implies a comparison of total conditions at station (or state) 1 to total conditions at station 2 as in Equation 2.11.

$$\Pi_{imp(T-T)} = \frac{p_{02}}{p_{01}} \quad (2.11)$$

Total-to-total measures are critical if the kinetic energy is exploited in the next part of the stage, as is the case in this study. Total-to-static measures are useful if the exit kinetic energy is wasted (Dixon, 1998).

The impeller tip speed,  $U_2$ , has a big influence on the pressure ratio that can be achieved. The higher the speed, the higher the pressure ratio. However, material stresses limit the tip speed, since the stresses increase approximately proportional to the tip speed squared (Eisenlohr and Benfer, 1993).

Gases inherently gain in temperature when undergoing a compression process. The compression process is not reversible, which is why more heat is generated than ideally predicted. A measure of efficiency of a compressor impeller is the isentropic efficiency. It is defined by the ratio of useful energy imparted to the fluid to the power supplied to the rotor (Dixon, 1998) which may be written as

$$\eta_{imp(T-T)} = \frac{h_{02s} - h_{01}}{h_{02} - h_{01}} = \frac{\left(\frac{p_{02}}{p_{01}}\right)^{\frac{\gamma-1}{\gamma}} - 1}{\left(\frac{T_{02}}{T_{01}}\right) - 1} \quad (2.12)$$

### 2.2.2. Surge and Choke

Surge and choke are the two extremes on the impeller performance curve. Stable operation of the compressor is achieved between these two extremes. When considering internal flow, the flow area exhibits a minimum at some point along a streamline. The location of this area is called the throat. If the Mach number reaches unity at the throat the mass flow rate is at its highest possible value and the flow is said to choke:  $m = m_{choke}$  (Dixon, 1998). Surge, on the other hand, represents the condition of unstable operation of the compressor at low flow rates. The instability is characterised by flow reversal connected with audible sounds and major mechanical vibration; the primary cause being aerodynamic stall (Boyce, 2002). Aerodynamic or blade stall occurs when the angle of attack exceeds its critical value such that the separation point moves far away from the TE, which causes the pressure drag to dominate and the lift to decrease drastically. In order to define the operating range of a compressor, Tamaki *et al.* (2009) describe a surge margin (SM) by

$$SM = \frac{m_s - m_o}{m_o} \quad (2.13)$$

where the subscript  $s$  denotes the point on the surge line and  $o$  the design point on the same operating line. Figure 6 depicts a typical compressor map of mass flow parameter  $\frac{m\sqrt{T_{01}}}{P_{01}}$  against pressure ratio showing the surge line, operating line and different corrected speed lines.

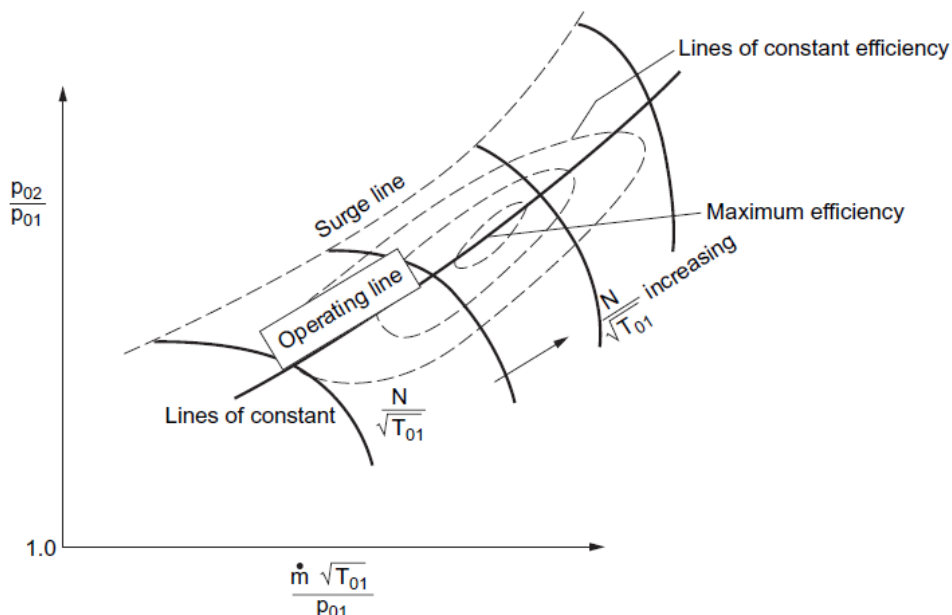


Figure 6: Typical compressor map (Dixon, 1998)

### 3. THE COMPRESSOR DESIGN PROCESS

In order to achieve the MGT thrust specification, it is necessary that the compressor stage design be integrated into the MGT layout and match the engine thermodynamic cycle. It is critical for an efficient engine design to consider all MGT components and their interaction with each other. Important factors to consider include the engine size, engine performance, global temperatures, engine and component layout, the materials, fitting and assembly of the components as well as the dynamic and thermodynamic behaviour and interaction of the different components. Additionally, it is important to consider off-design conditions such as operating points of mass flows and/or rotational speeds that differ from design conditions.

As the engine is in an early phase of development it was not possible to deliberate all factors. It would also have exceeded the scope of the thesis. The focus therefore lied in

- adhering to the given engine size specifications
- meeting the compressor performance requirements (aerodynamic and structural)
- considering off-design conditions and behaviour

In order to design a compressor, the performance and size specifications are needed. The engine size and compressor stage specifications were defined by the CSIR with help of an engine thermodynamic cycle analysis code. The design operational conditions as well as the thermodynamic conditions at the boundaries are transferred to a 1-dimensional mean-line compressor design code. This code generates the impeller geometry based on the performance predicted by turbomachinery theory and empirical methods applied to a mean flow path. The engine cycle analysis (ECA) and 1-dimensional performance prediction might have to be repeated based on the results of the 1-dimensional code.

Once a design has been found using 1-dimensional methods, the performance of the design needs to be confirmed using 3-dimensional flow simulation tools (CFD). If flow-related problems arise which were not predicted by the 1-dimensional mean-line analysis, the designer must go back to the ECA and mean-line design. If the performance of the mean-line design is satisfactory, the design may be optimized in three dimensions, as done in this thesis. The optimization may entail a CFD-chain coupled with an FEA (finite element analysis)-chain (aero-mechanical optimization) or the aerodynamic (CFD) and mechanical (FEA) optimization may be done independently.

In this thesis the original objective was to obtain a compressor impeller design using 1-dimensional methods and aerodynamically optimize this design using CFD. The optimized design was to be counter-checked for its structural integrity

thereafter, with small manual changes to be made, if necessary. However, initial FEA showed the structural performance was worse than anticipated and thus it was decided to look at the mechanical optimization routine as well. The resources were made available by the NUMECA Ingenieurbüro (NIB) (engineering office) to complete a mechanical optimization using FEA, which meant a coupled CFD-FEA optimization could also be completed.

The FEA chain implemented in the optimization only accommodates the application of radial acceleration loads. Aerodynamic loads are not included. A modal analysis is also not integrated in the software. The time and resources were available to complete a modal analysis using a different FEA package.

The ECA was conducted using GasTurb12. Initially it was planned to use the in-house 1-dimensional compressor performance prediction code to obtain an impeller design. For reasons that will be explained in the following chapters, it was decided to use the commercial layout-tool CFturbo instead. The subsequent CFD-, FEA- and coupled optimization were completed using NUMECA FINE™/Design3D. MSC SimXpert was implemented for the subsequent linear static FEA to validate FINE™/Design3D's FEA results and to complete a modal analysis of the rotor. A detailed explanation of the numerical methods and the software packages used to apply them can be found in Appendix A, along with the CFturbo layout methodology. The theory regarding linear static and modal analyses is also explained in Appendix A.

The design procedure conferred above is outlined in Figure 7. A solid line represents the path followed in this thesis and dotted lines represent possible alternatives. Shaded boxes denote the different software packages indicated in italics.

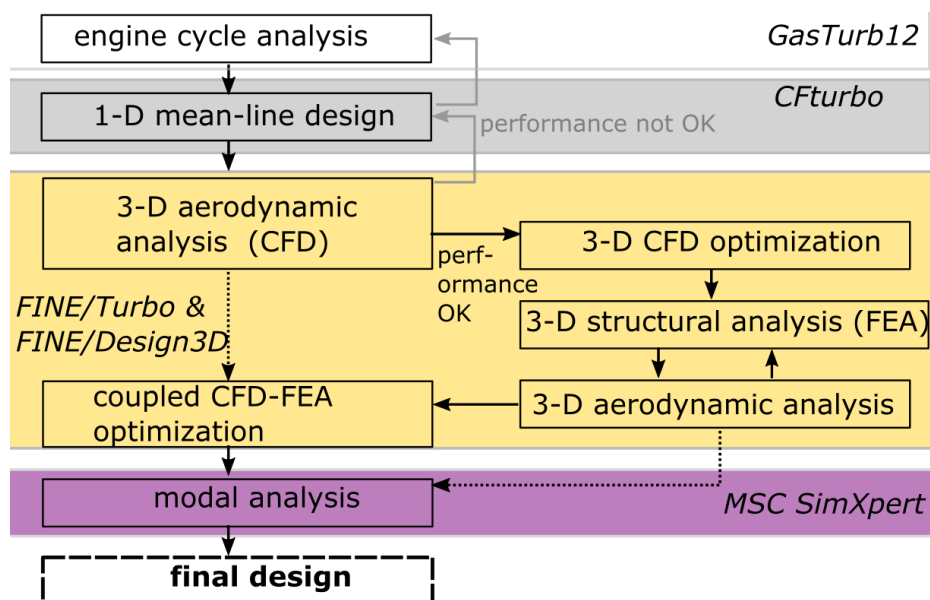


Figure 7: Compressor impeller design procedure

## 4. LITERATURE OVERVIEW

In this chapter the relevant literature concerning mixed-flow compressors is reviewed. This includes the design, analysis and optimization of this turbomachine.

### 4.1. Mixed-flow Compressors

Work on mixed-flow compressors began in the early 1940s at the National Advisory Committee for Aeronautics (NACA), the predecessor of the NASA. NACA mainly sought to apply the mixed-flow compressors in turbochargers for aircraft engines. Results by King and Glodeck (1942) revealed high impeller efficiency (0.92) and large losses in the diffuser.

Hindering the work on mixed-flow compressor stages in the '50s and '60s were the structural limitations, lack of an experimental database, restricted computational capability and difficulties with the development of the diffuser. Once compressor designers had produced a means of designing the compressor using computational tools, successful mixed-flow compressor designs started emerging (Musgrave and Plehn, 1987). In the '80s interest in mixed-flow impellers was revived, starting with Whitfield and Roberts (1981). Their testing of three mixed-flow impellers demonstrated that "overall flow stability between low and high rotational speeds is improved by using a mixed flow impeller whose vane tips are cut off horizontally". Musgrave and Plehn (1987) successfully designed a mixed-flow compressor stage with a pressure ratio of 3:1 and a rotor efficiency of 91%.

Mönig *et al.* (1987) discussed the possible application of mixed-flow compressors in small gas turbines due to the high mass flow and pressure ratio obtained in a single stage, which meant that a high power-to-weight ratio could be obtained. Six years later Mönig *et al.* (1993) had designed and experimentally tested a 5:1 mixed-flow supersonic compressor, focussing on shock-wave stabilization in the impeller. Eisenlohr and Benfer (1994) outlined the aerodynamic design and investigation of a 5.5:1 mixed-flow compressor stage to be used in a turbojet. The diffuser was responsible for a significant reduction in stage efficiency.

A two-stage mixed-flow/centrifugal compressor combination for a turbojet engine was patented by Youssef and Weir (2002). The authors noted that there was no production jet engine with a mixed-flow compressor to that date, although experimental results were well documented. The authors focused their design on subsonic flow. Hamilton and Sundstrand have successfully developed MGTs of mixed-flow design for thrusts between 200 and 450 N and revealed some details of their designs (Harris *et al.*, 2003). The Hamilton and Sundstrand TJ-50 demonstrated performance capabilities surpassing any other engine of its size in

the late '90s. Notable was that the engine had to operate amid two of the shaft critical modes and, at full power, it had to be kept stable near the 2<sup>nd</sup> eigenmode.

## 4.2. Compressor Analysis and Design

### 4.2.1. Mean-Line Performance Analysis

Mean-line theory as well as loss models and deviation angles provided by Aungier (2000) were successfully implemented by Benini and Giacometti (2007) to design a centrifugal impeller with radial blades. The compressor stage design was part of a MGT development for research purposes. The engine was tested and achieved the objective of 200 N thrust.

Fischer *et al.* (2014) designed a centrifugal compressor stage for a turbocharger using the layout tool CFturbo. The specified total stage pressure ratio was 4:1. CFD analyses were completed on different stages where the variation in targeted geometric features was performed. A design of the compressor stage was obtained which conformed to the specifications. Experimental results showed discrepancies in the mass flows predicted by the CFD analysis and the test data, which was attributed to the testing method and experimental ambient conditions.

### 4.2.2. 3-dimensional Aerodynamic, Structural and Multi-disciplinary Analysis

Numerical analyses and theoretical evaluations of mixed-flow compressor rotors were done by Niculescu *et al.* (2007) to try to diminish secondary flows. Niculescu *et al.* (2007) showed that swirl induced by inlet guide vanes reduce secondary flows in areas of axial to radial flow transition. Two years later Ramamurthy and Srharsha (2009) published their numerical work on a 60°-cone-angle compressor impeller to be used for a micro jet engine and confirmed that constant tip clearance compares favourably to varying tip clearance and also that the flow at impeller exit is uniform without the jet-wake flow pattern common in radial impellers.

Chen *et al.* (2011) successfully improved the performance of an existing 80 mm diameter transonic mixed-flow compressor via modifications to the splitter blades. CFD was used to help improve the design. The impeller is used in a micro jet engine producing 180 N thrust. In the same year Cevic and Uzol (2011) presented an optimized mixed-flow impeller design for a 220 N MGT. The optimization was applied to a neural network, which was trained using a database of two-dimensional performance prediction results. The constraints were specific thrust and thrust specific fuel consumption of the MGT. Initial CFD results of the optimized design illustrated shock structures potentially reducing the performance of the impeller.

Zheng *et al.* (2012) studied the effects of disk geometry on the strength of a centrifugal compressor impeller used for a high pressure turbocharger using FEA. Only centrifugal loads were considered. It was found that reduced disk tip thickness decreases bore and fillet stresses. With increase of the height of the hub step the fillet stresses were reduced, but the bore stresses passed a minimum and then increased. Increasing the bore radius also increased the bore stresses.

Ramesh Rajakumar *et al.* (2013a) detailed a CFD analysis done on the flow through a mixed-flow compressor under various operating conditions. The jet-wake pattern found in radial compressors was not observed in this analysis of the mixed-flow rotor. Ramesh Rajakumar *et al.* (2013b) investigated the effects of different tip clearances on the performance of a mixed-flow compressor impeller. CFD results showed that the performance deteriorates with increased tip clearance. In a very recent paper, Xuanyu *et al.* (2015) published their design and analysis results of three different mixed-flow compressor impellers using NUMECA CFD software in order to determine the effect of load distribution on the impeller performance. It was concluded that higher loading of the blade should occur near the “posterior area” (trailing edge) at the hub and, in case of the shroud, near the front of the blade (leading edge). The authors predicted an increased application of mixed-flow compressors in the future due to the demand for higher mass flow and performance.

#### 4.2.3. 3-dimensional Aerodynamic, Structural and Multi-disciplinary Optimization

The approach of constructing an approximate model (“response surface”) by using an artificial neural network (ANN) applied to a database with Navier-Stokes solutions, which is utilized by a genetic algorithm (GA) to optimize blade shapes, was proposed by Pierret *et al.* (2000). Demeulenaere *et al.* (2004) presented a 3-dimensional multipoint optimization process proposed by NUMECA International. A turbine rotor and a transonic compressor rotor blade were optimized.

Valakos *et al.* (2007) structurally optimized the backface geometry of a centrifugal compressor impeller using a differential evolution (DE) algorithm. The optimization was completed in the CATIA environment. A 68% improvement in stresses was obtained compared to the planar reference geometry. The DE algorithm produced better results than the simulated annealing algorithm.

A radial compressor stage for turbocharger application was optimized by Hildebrandt *et al.* (2009) using only CFD. The optimization was conducted at three operating points simultaneously. An increase of 20% in total pressure was achieved while conserving surge margin and choke limit. Numerics were validated via experiment. Verstraete *et al.* (2010) conducted a multi-disciplinary optimization of a radial compressor for MGT applications. A GA was implemented together with an ANN while combining CFD and FEA results. The authors report on the main parameters that allow the stresses to be reduced as:

- Blade thickness at hub
- Blade leading edge lean and height
- Trailing edge blade height
- Blade curvature

Similarly, Hildebrandt *et al.* (2011) completed a coupled aero-mechanical optimization of a centrifugal compressor impeller at multiple operating points. The performance map of the compressor was successfully widened. The diffuser geometry was kept constant. Numerical outcomes were confirmed by experimental results. In a comparable fashion Demeulenaere *et al.* (2015) redesigned a centrifugal compressor impeller utilizing a multi-point aero-mechanical optimization approach. Aerodynamic performance as well as the operating margin was improved while the peak stresses were reduced considerably. FINE<sup>TM</sup>/Design3D and the integrated OOFELIE kernel were used.

#### 4.2.4. 3-dimensional Modal Analysis

Kammerer (2009) analysed the vibrational characteristics of high-speed radial compressor blades. He investigated four forced-response scenarios: inlet flow distortion, unsteady blade excitation, damping and resonant response. The behaviour corresponding to the first two resonant blade modes were examined. FEA was used for the numerical analysis of the solid sector and was validated via experiment. Aerodynamic and material damping properties were found and it was concluded that aerodynamic damping is dominant.

### 4.3. Previous Work at Stellenbosch University (SU)

Research into the design of a centrifugal compressor (van der Merwe, 2012) as well as a radial diffuser (Krige, 2014) for MGT application was successfully completed at SU. Van der Merwe (2012) aero-optimized a mean-line compressor design obtained using an in-house 1-dimensional code adapted from de Wet (2011). He also analysed the structural integrity of the radial impeller design subject to centrifugal loads. By adding a curved back plate contour with a hub step to the impeller he reduced the bore stresses.

De Villiers (2014) designed a radial compressor stage focusing on impeller-diffuser matching. Basson (2014) presented a design methodology for axial flow turbine stages for MGT application. He conducted CFD analyses as well as linear static and modal FEA on different turbine designs. The design of a single blade-row radial-to-axial curved diffuser was completed but not yet published by Burger.

## 5. REFERENCE MIXED-FLOW COMPRESSOR ANALYSIS

In order to prove proficiency in using the CFD software, a reference mixed-flow impeller-diffuser stage was analysed. The geometry was made available by the NUMECA Ingenieurbüro (engineering office) (NIB), Germany, and the meshing, solving and post-processing was completed using NUMECA software. Numerical results for pressure ratio and efficiency were compared to those previously obtained by NIB. Experimental values from the DLR (Deutsches Zentrum für Luft und Raumfahrt) of the stage pressure ratio and efficiency at design speed were available.

### 5.1. Geometry

The geometry of the reference stage was obtained from NIB in the form of a \*.geomTurbo file. A meridional view of the geometry analysed is shown in Figure 8. The stage is designated SRV4-D104 by NIB.

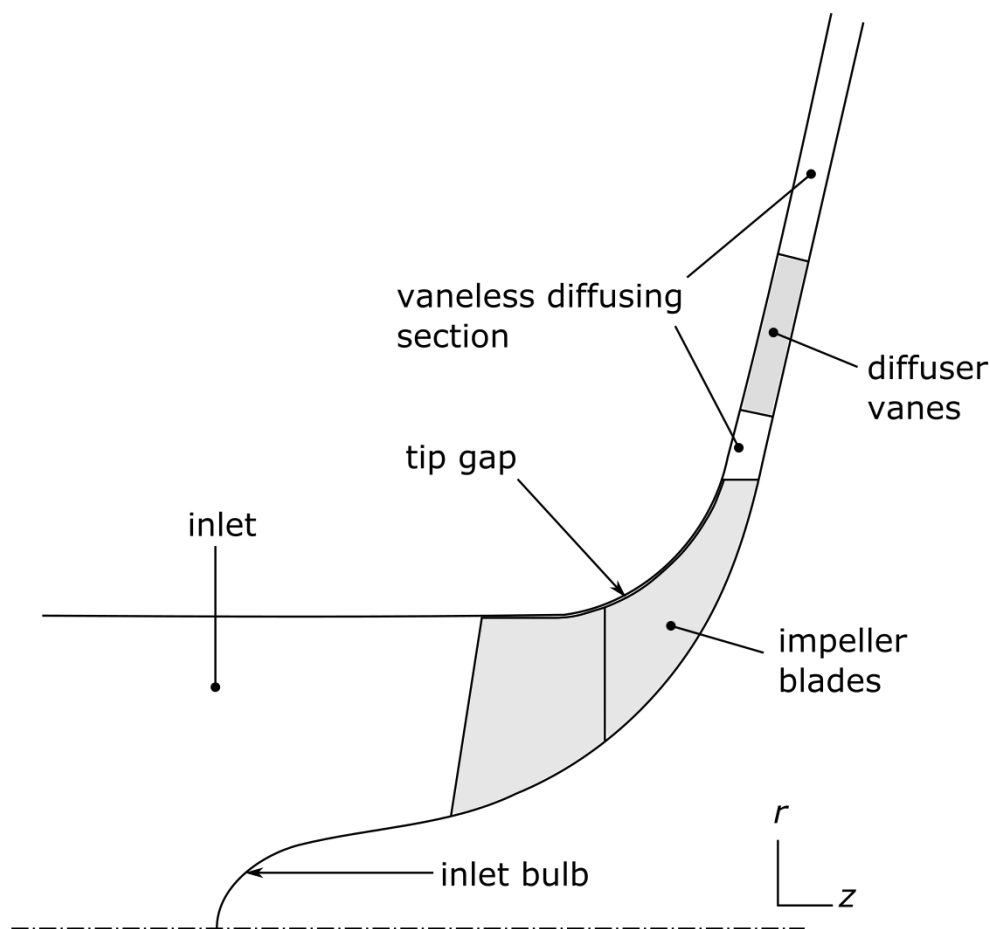


Figure 8: Reference compressor stage meridional contours and traces

The stage consists of an inlet bulb, an impeller with splitter blades and a vaned diffuser section, which is followed by a vaneless diffusing passage. The bladed sections are shaded to differentiate from the vaneless space. The stage has a meridional exit angle of  $\alpha_{C2} = 86.6^\circ$ .

## 5.2. Computational Domain and Discretization

AutoGrid5<sup>TM</sup> was used to generate the CFD-mesh. The following steps were followed to generate the grid:

- The \*.geomTurbo geometry file was imported.
- The row wizard was run to obtain an initial grid.
- Grid quality was improved by manually changing the B2B grid properties.
- The 3-dimensional grid was generated and the 3-dimensional properties were changed thereafter, if necessary.

The computational domain encompasses the surface of the hub, shroud and blades as well as the through-flow volume from inlet to outlet. Since the computation by NIB was completed without fillets, the computation in this project was run without fillets as well.

Grid defining parameters which are critical to the solution are given in Table 1. These include the cell width at the wall and TE, the number of flow paths from hub to shroud and the size of the tip gap, which was constant from leading to trailing edge and was specified by NIB.

Table 1: Important grid defining dimensions of the reference stage

Cell width at wall and TE ( $\mu\text{m}$ )	# of flow paths	Tip gap (mm)
2.5	73 (17 in tip gap)	0.5

The cell width at the wall is a parameter used to calculate the dimensionless wall-distance  $y^+$ . The dimensionless wall-distance needs to have a value below 10 at the wall (NUMECA International, 2014b) for the model to accurately resolve the boundary layer when implementing the Spalart-Allmaras (SA) turbulence model (Appendix A). The wall- $y^+$  values can only be confirmed after a simulation has been run, but a first guess of  $5 \mu\text{m}$  was shown by experience to yield wall- $y^+$  close to the required range. However, after investigating preliminary results, the wall- $y^+$  values were too high and the cell width at the wall was halved, which resulted in acceptable wall- $y^+$  values. The maximum wall- $y^+$  values of the reference stage are given in Appendix F.

The B2B grid is formed by combining mesh blocks of (typically) H- and O-topology. Different combinations are suitable for different geometries. For

impellers with splitter blades the H&I-topology ensures better mesh quality (Numeca International, 2014a). This topology consists of three H-blocks and one skin O-block for each blade, where the O-block and two H-blocks are optional. The H&I topology was used for all impeller CFD grids in this thesis. The distribution of the grid points of the reference impeller is shown in Appendix E. The H-topology at inlet and outlet was disabled. *High Staggered Blade Optimization* was enabled for main blade and splitter, where the main blade inlet type was set to *high angle* and the outlet type to *low angle*. Splitter blade inlet type was *normal* and outlet type *low angle*. The diffuser was meshed using the default O4H-topology and a butterfly-topology was selected for the inlet bulb, which extended to a radius of 0 mm (Appendix E). In the *3-D mesh control* tab, the inlet and outlet were not untwisted. The *cell width at the blade wall* was enforced. A *Span interpolation* of 5% yielded acceptable grid quality. This means the mesh optimization was done on 20 layers or flow paths (0%, 5%, 10%, etc...) and was interpolated in-between the layers.

A grid must be of a certain quality in order to ensure solver stability and a converged solution. Major quality criteria are skewness (orthogonality), expansion ratio, aspect ratio and angular deviation. They can be applied to surface or volumetric cells.

- Orthogonality is a 2-dimensional measure of the minimum angle between cell edges. It is in the range of 0° to 90°.
- Comparing the size of two adjacent cells produces the expansion ratio of a range between 1 and 100.
- Aspect ratio is defined by the ratio of height to width of the same cell and is in the range of 1-50,000.
- A contrast of the deviation in angle between two adjacent cells produces the 3-dimensional angular deviation. It is in the range of 0° to 90°.

The quality of the final grid used for the reference stage is summarized in Table 2. The suggested range is based on values obtained from NIB by van der Merwe (2012). The values are a guideline, but should be enforced if solver instabilities and solution inaccuracies are to be prevented. Depending on the blade geometry, this might be difficult to realize; a maximum expansion ratio of less than 2.5 is especially difficult to achieve without compromising the angular skewness.

Table 2: Reference compressor stage mesh quality

Criterion	Critical value	Suggested range	% bad cells
Angular skewness (deg)	21.7	>20	0
Aspect ratio	1 705	<10 000	0
Expansion ratio	2.78	<2.5	0.02
Angular deviation (deg)	35.5	<45	0

The AutoGrid<sup>TM</sup>5 grid optimizer aims to optimize the grid quality and generates the B2B mesh. If the grid quality is not acceptable when comparing values to the suggested limits in Table 2, the user has to look for ways of improving the quality manually, like changing the number of grid points along a block or the number of grid *optimization* steps. In this case 200 *optimization* steps along with 100 *gap optimization* steps produced the best grid quality.

The entire final mesh consisted of 4.9 million cells. The inlet bulb consisted of 230,000, the impeller of 3.7 million and the diffuser of 1 million cells. A comparison of final results with those of NIB showed that a grid independence study was unnecessary. The grid at the 2<sup>nd</sup> grid level (1-1-1) is presented in Figure 9. A close-up of the TE is also shown. The structured grid shows minimal cell clustering and a uniform cell distribution. Refinements at the walls of the blade can also be seen.

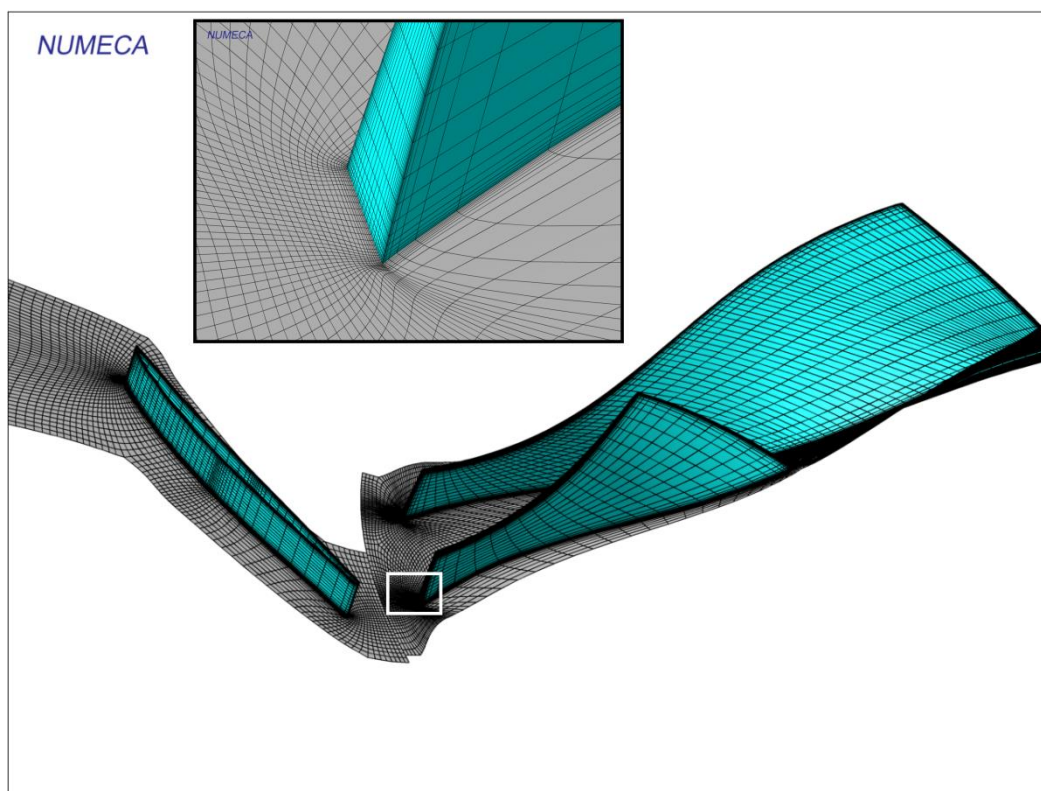


Figure 9: 3D grid lines on hub and blades of the reference stage (2<sup>nd</sup> multigrid level)

### 5.3. CFD Model

Modelling of the flow of gas through a compressor stage comprises the definition of a gas model reflecting the behaviour of the gas, the turbulence model, the rotor/stator (R/S) interface, boundary conditions of the flow domain and the

details of the numerical method and solver. An initial solution from 1-dimensional methods is commonly used when running the first computation of the performance curve. These tasks were completed using FINE<sup>TM</sup>/Turbo v. 9-1.3.

### 5.3.1. Fluid and Flow Model

Air was modelled as a *perfect gas*, which improves CPU time compared to the *real gas* model (NUMECA International, 2014b). This meant the air behaved according to Equation 2.8 with its property values as given in Table 3. The specific heat  $c_p$  and specific heat ratio  $\gamma$  were constants, which is an adequate assumption for the relatively small temperature changes in the compressor (White, 1998).

Table 3: Ideal (perfect) gas properties of air

$c_p$ (J/kg.K)	$\gamma$	$\nu @ T = 293.11\text{K}$ (m <sup>2</sup> /s)	Viscosity law
1,006	1.4	$1.716 \cdot 10^{-5}$	Sutherland

The RANS equations were selected to govern the steady-flow physics. To model the effects of turbulence the SA model was implemented (Xuanyu *et al.*, 2015). Gravity forces and preconditioning for low-speed flows was disabled. The R/S interface chosen for the computation was the *non-reflecting 1-D* R/S interface with the expert parameter LOCCOR enabled to improve mass conservation. LOCCOR “applies corrections for the entropy and the stagnation enthalpy in case of using a non-reflecting R/S interface” (NUMECA International, 2014b).

### 5.3.2. Boundary Conditions

In Figure 10 the boundary patches of the CFD model are depicted. Different colours represent different boundary types. Only the periodic boundaries have not been shaded. Periodic boundaries are present at the left and right confines of the domain, where the pressures on the one surface are aligned with those of the other periodic surface to model periodicity.

The boundary conditions (BCs) applied at the different patches are shown in Table 4. At the inlet total conditions were imposed and the inlet velocity was assumed purely axial (in the  $z$ -direction). For a complete performance curve in the stable operating region the outlet static pressures varied from 390 kPa (choke) to 600 kPa (surge). The blades were set to rotate at 50 krpm while the shroud was fixed. An area was defined, which enclosed the rotating part of the hub, by entering a lower and upper bound for the  $z$  and  $r$ -values. The rectangular area covered the hub curve from inlet bulb to the TE of the blades. This ensured a fixed hub upstream of the impeller.

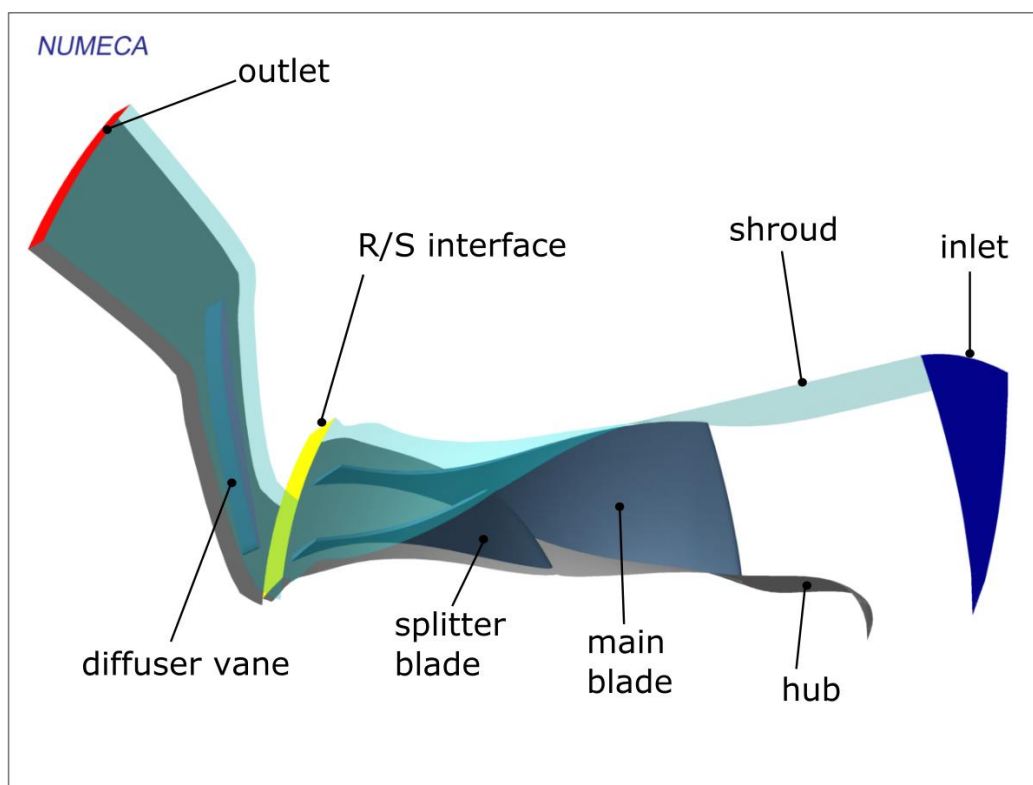


Figure 10: Boundary patches of the reference compressor stage

Table 4: Boundary conditions of the reference compressor stage

<b>Inlet</b>	<i>Total Quantities Imposed</i>	<i>Angle from axial direction</i>	$p_{01}$ (kPa)	$T_{01}$ (K)	Turbulent viscosity, $\nu_t$ ( $\text{m}^2/\text{s}$ )
			103.25	288.15	0.0001
<b>Outlet</b>	<i>Pressure Imposed</i>	Averaged Static Pressure (kPa)			
		390...610			
<b>Hub, shroud, blades</b>	<i>Solid (no-slip condition)</i>	Shroud	Blades	Hub: area defined rotation speed	
		0 rpm	50,000 rpm	50,000 rpm	

### 5.3.3. Numerical Model

The so-called CPU booster, a convergence acceleration algorithm, was enabled. It reduces computational time significantly while increasing the risk of computational instability. The NUMECA flow solver EURANUS makes use of a

multi-grid technique allowing the solution to converge faster by first running on coarse grids and subsequently transferring the data to a finer grid. The current grid level was set to be the finest (0-0-0) and the number of grid levels was 3. Table 5 contains the details of the numerical model.

Table 5: Reference stage numerical model details

<b>Sweeps</b>	Scheme definition	# of sweeps on successive grid levels
	Increase on higher level	1 2 16
	Spatial discretization scheme	Time stepping technique
	Central	Local
<b>Full multigrid parameters</b>	Max. # of cycles per grid level	Convergence criteria on each grid level
	25	-3

#### 5.3.4. Initial Solution, Output and Convergence Criteria

A mean-line analysis is performed by the code prior to the first iteration. The 1-dimensional results are then extrapolated on the 3-dimensional mesh, applying radial equilibrium. For the solver to calculate the initial solution *for turbomachinery*, the inlet static pressure was defined to be of constant distribution with a value of 90 kPa. Similarly, at the R/S interface a value of 300 kPa was defined.

The quantities to be written to the solution file (\*.cgns) can be selected in the *Output* window. The pressure, temperature, velocity, Mach number, density, entropy and wall- $y^+$  values were selected to be recorded. Circumferentially-averaged solutions were set to be calculated for the meridional view.

While monitoring the simulation status, the convergence of the global residual, total pressure ratio, isentropic efficiency as well as inlet and outlet mass flow rates may be observed. The mass-averaged weighted integral as described in Appendix D is used at inlet and outlet of the domain to calculate these quantities. Convergence is said to be satisfactory when the following criteria have been met (NUMECA International, 2014b):

- the residuals have decreased by at least three orders of magnitude
- the global performance has completely stabilized
- the mass flow in and out have converged to a difference of less than 1%

The convergence criteria were set to be a decrease of seven orders of magnitude such that the solver does not exit prematurely.

### 5.3.5. Post-processing

To evaluate the results the NUMECA result file (\*.mf) was used. The relevant performance parameters as well as the mass flow at the inlet and outlet of the flow domain are listed here. This was convenient, as the stage performance was to be compared and not the impeller performance only. Hence no post-processing macro needed to be written and the evaluation was consistent with the results evaluation procedure by NIB.

## 5.4. Results

The pressure ratio, efficiency and mass flow rate were normalized using the design point value of the stage pressure ratio and efficiency obtained by NIB. Hence the normalized value is the operating value divided by the value at design point. The performance curves are given in Figure 11. The curves obtained by this investigation as well as the curves obtained by NIB are shown in addition to the experimental results.

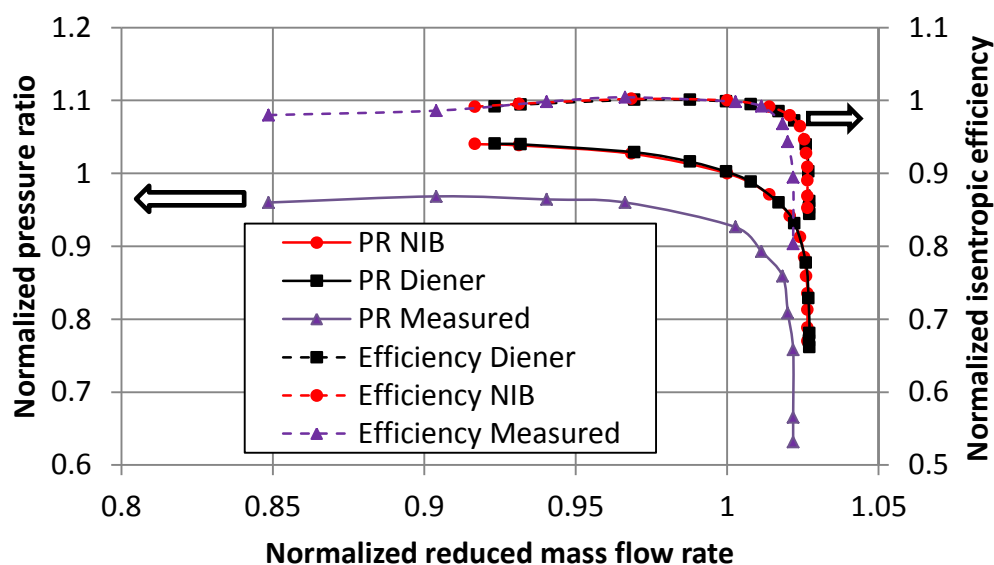


Figure 11: Reference stage performance curves in contrast

The CFD results compare very well with those obtained by NIB, a relative indication already given in the figure due to the normalization. Experimental values show a deviation of around 7% in pressure ratio at design point. Proficiency in the use of the NUMECA CFD software has now been proven and a mixed-flow compressor impeller may now be analysed using the software.

## 6. INITIAL IMPELLER DESIGN

This chapter details the initial 1-dimensional mean-line design of the impeller, the strategy followed to obtain a well-performing design and the CFD analysis of some of the designs that were generated using 1-dimensional methods.

### 6.1. Performance and Size Specifications

The size and performance specifications of the MGT and compressor were obtained from the CSIR. The engine diameter was limited to 180 mm, and the engine length to 400 mm. A thrust of 600 N at design conditions was the target. This target was to be met at an actual design mass flow rate of  $m_{design} = 0.85$  kg/s and a rotational speed of  $N_{design} = 95,000$  rpm. The total inlet conditions were specified as  $T_{01} = 300$  K and  $p_{01} = 100$  kPa.

The gas turbine cycle results performed in GasTurb12 by the CSIR yielded the following performance specifications for the compressor stage: a compressor stage pressure ratio of  $\Pi_{stage(T-T)} = 3.83$  and a compressor stage efficiency of  $\eta_{stage(T-T)} = 0.85$ . The target efficiency was 85% and it was not allowed to drop below 70%. The targets were to be reached at the point of highest efficiency. These values were calculated using a turbine inlet temperature of 1150 K. Using this temperature equates to 520 N thrust only. The thrust is meant to be improved by increasing the burner exit temperature which should be possible when using a ceramic turbine. The temperature increase may be achieved by raising the fuel mass flow rate.

The impeller performance has to surpass that of the stage, as no more energy is delivered to the system in the diffusing passage while the total quantities will only incur losses in the diffuser. Therefore the impeller pressure ratio was estimated by transferring the total pressure loss in percent from the reference stage. This loss was approximately 8%, meaning with a stage pressure ratio of 3.83 the impeller pressure ratio should be at least 4.15. The target efficiency a designer strives for is as close to unity as possible. Given a stage target of 85%, the impeller had to demonstrate an even higher value. Table 6 summarizes the performance specifications.

Table 6: Compressor stage specifications and anticipated impeller specifications

Quantity	$\Pi_{stage(T-T)}$	$\Pi_{imp(T-T)}$	$\eta_{stage(T-T)}$	$\eta_{imp(T-T)}$
Specification	3.83	>4.15	85%	>85%

Given the criteria, a first estimate of the necessary impeller tip radius along a mean-line  $r_{2(m-l)}$  was calculated using the theory described in Chapter 2. The

calculation was completed using an estimated impeller efficiency of  $\eta_{imp(T-T)} = 85\%$ , an impeller pressure ratio of  $\Pi_{imp(T-T)} = 4.15$ , the assumption of axial entry ( $C_1 = C_{z1}$ ) and radial discharge ( $C_{z2} = 0$ ), neglecting slip and assuming no backsweep ( $C_{\theta 2} = U_2$ ). This yielded  $r_{2(m-l)} = 42.4$  mm.

## 6.2. Mean-Line Design

Performance of compressors may be roughly estimated by implementation of turbomachinery theory along a mean-line through the machine. The physical properties are assumed constant perpendicular to the direction of motion and change only in the direction of motion (Whitfield and Baines, 1990:43). The flow along the mean-line is modelled using continuity, Euler's turbomachinery equation, the 1<sup>st</sup> law of thermodynamics and the 2<sup>nd</sup> law of thermodynamics. Losses incurred in the machine that cannot be predicted using these equations are defined through analytically and empirically determined relations.

Students from SU have previously developed a 1-dimensional mean-line compressor design code for centrifugal compressors in MATLAB (de Wet, 2009) (van der Merwe, 2012). The method of performance prediction is based on the theory described by Aungier (2000). A flow-chart of this code is given in Appendix B. An attempt was made to adapt this code to support the performance prediction of mixed-flow compressors. This was done by changing the mean-line to be at an angle of  $\alpha_{c2}$  at the impeller outlet and including the resulting axial velocity component in all calculations. It was, however, not possible to obtain a performance curve of a mixed-flow compressor based on only the geometric relations and optimization that are integrated in the code.

An indication of the range of certain geometric parameters was needed for the mean-line code to work. The CSIR was also conducting a 1-dimensional analysis of a mixed-flow compressor impeller at the time. Using preliminary general dimensions obtained from the CSIR, the MATLAB code was able to generate an impeller performance curve. A CFD analysis of the design generated by the in-house code was completed thereafter. The results were evaluated at the impeller tip and are shown in Figure 12. The potential of the MATLAB code is evident: the highest efficiency point (HEP) is at the specified mass flow rate and the efficiency value at the HEP also compares very well with CFD results. There is, however, a significant difference (22%) between the mean-line and the CFD pressure ratio results. Surge and choke are seen to be predicted very conservatively, with a smaller stable region of operation.

It is clear that the pressure ratio, with a value of 2.63 at HEP, was well below the specified value of 4.15 (-36%). This was a problem with all the attempts at a mean-line design in MATLAB. Given that a well-performing design could not be obtained from the 1-dimensional in-house code, time constraints forced the use of a different 1-dimensional layout tool. CFturbo was selected for this purpose.

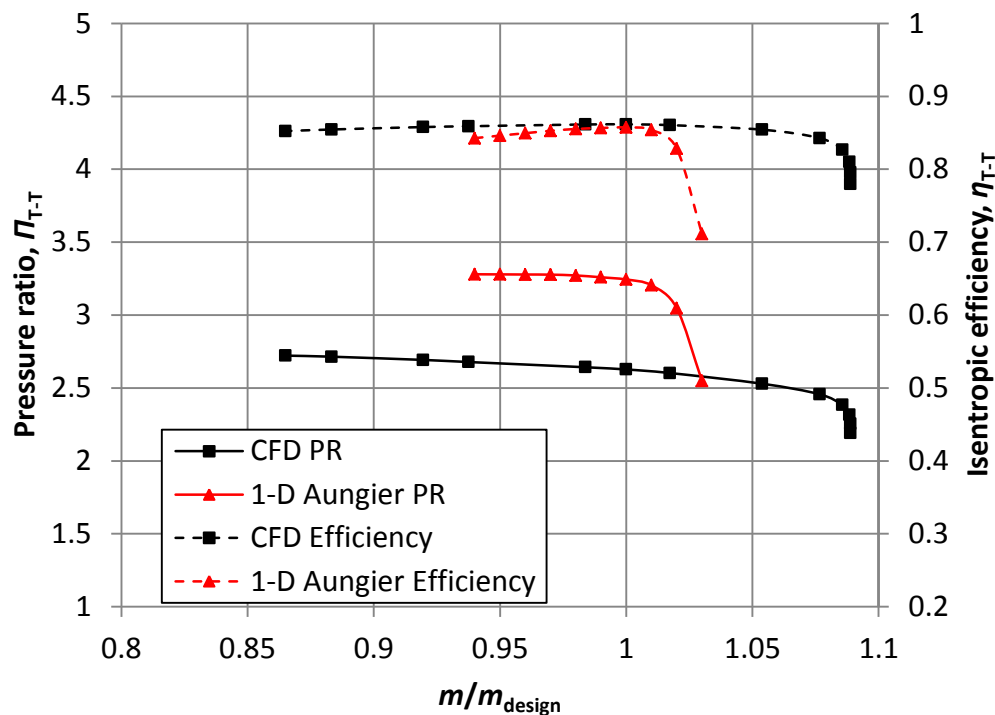


Figure 12: Mean-line calculations according to Aungier (2000) compared with CFD results of a mixed-flow impeller design obtained from the in-house MATLAB code

### 6.2.1. Approach

First, the design point specifications were defined as input for CFturbo. CFturbo then generated a geometry based on the given specifications. Next, the geometry was adapted such that the meridional exit angle  $\alpha_{C2}$  was as suggested by preliminary CSIR results ( $55^\circ$ ). The TE meridional trace was set to be perpendicular to the flow direction. These manual changes in the suggested CFturbo design, however, lead to inferior performance and very high mass flow rates at the HEP ( $>1.2$  kg/s).

Considering the above, the design point pressure ratio, mass flow rate and tip gap entered in CFturbo was changed in order to allow CFturbo to generate a design adhering to the specifications. A value of 0.2 mm was assigned to the tip gap which was suggested by the CSIR. This meant the tip gap represented 3.1% of the impeller tip hub-to-shroud height  $b_2$ . Van der Merwe's (2012) value of 4.5% compares relatively well. A smaller tip gap results in better performance as shown for a mixed-flow impeller by Ramesh Rajakumar *et al.* (2013b), but increases the risk of interference of the blades with the shroud during operation.

The meridional outlet angle  $\alpha_{C2}$  defines the machine type and was selected by CFturbo based on the specific speed of the machine, the European definition being

$$n_q = N * \frac{\sqrt{Q}}{H^{3/4}} \quad (6.1)$$

In Equation 6.1  $N$  is the number of revolutions per minute,  $Q$  is the volumetric flow rate in  $\text{m}^3/\text{s}$  and  $H$  is the head in m. Table 7 displays the different ranges of  $n_q$  associated with the different compressor types. The ranges of the specific speed associated with each machine type in CFturbo are according to the ‘‘Taschenbuch für den Maschinenbau’’ (Pocketbook for Mechanical Engineering) by Dubbel (1997).

Table 7: Machine type according to specific speed (CFturbo, 2014)

	Radial	Mixed-Flow	Axial
Specific speed (EU), $n_q$	10...40	40...140	140...400

The only change in the meridional contour was  $\alpha_{C2}$  at the shroud, which was set to be equal to  $\alpha_{C2}$  at the hub. The TE was at a constant radius by default, which, following the recommendation by Whitfield and Roberts (1981), was not changed. The CFturbo settings used in this study are listed in Appendix C.

### 6.2.2. Computational Domain and Discretization

Before the CFturbo designs were simulated using CFD, a ‘‘nose’’ was added to the hub contour using CFturbo. Furthermore, a vaneless diffuser passage was added to observe the flow behaviour under deceleration in a straight diffuser passage at the same outlet angle  $\alpha_{C2}$ . A constriction towards the outlet served to accelerate the flow to prevent any recirculation or backflow across the outlet. In Figure 13 the meridional contours as well as the traces of the main blade and splitter blade leading edge can be seen. Arrows are used to show the flow direction.

Figure 14 shows the computational domain enclosed by the inlet, outlet, hub, shroud and periodic boundary patches. The 3-dimensional grid on the 2<sup>nd</sup> multi-grid level (1-1-1) is shown in Figure 15. The refinement at the blade TE is also shown in Figure 15. It can be seen that some grid lines cluster together towards the shroud on the main blade. This is not desirable; nevertheless, the overall grid quality was still within acceptable limits as shown in Appendix E. Grid generation settings as well as the grid point distribution and the results of a grid independence study are also given in Appendix E. The resultant total number of cells amounted to 3.13 million on the finest grid level.

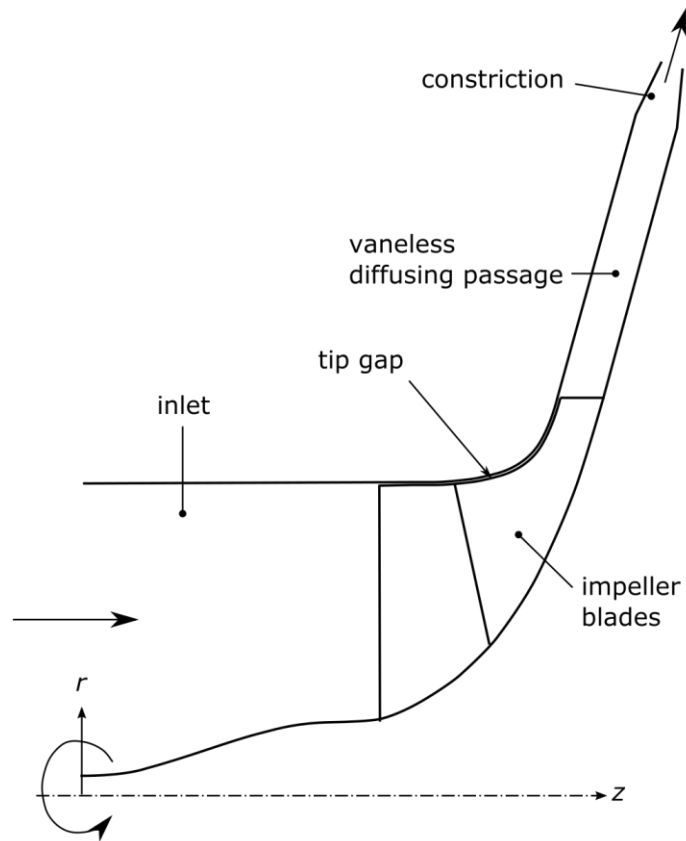


Figure 13: Meridional view of a CFturbo design with hub nose and diffuser passage

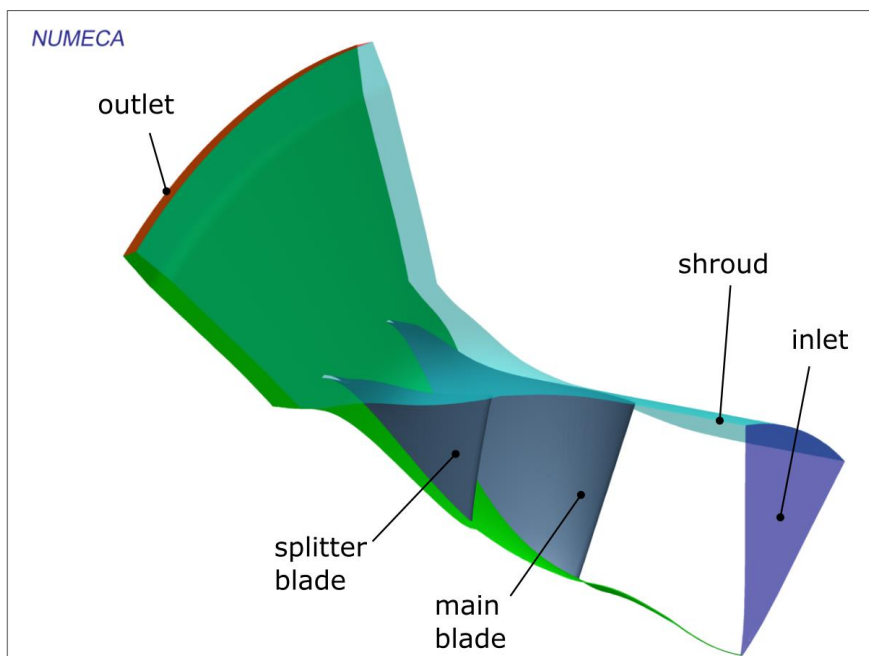


Figure 14: Computational domain enclosed by hub, shroud, inlet and outlet

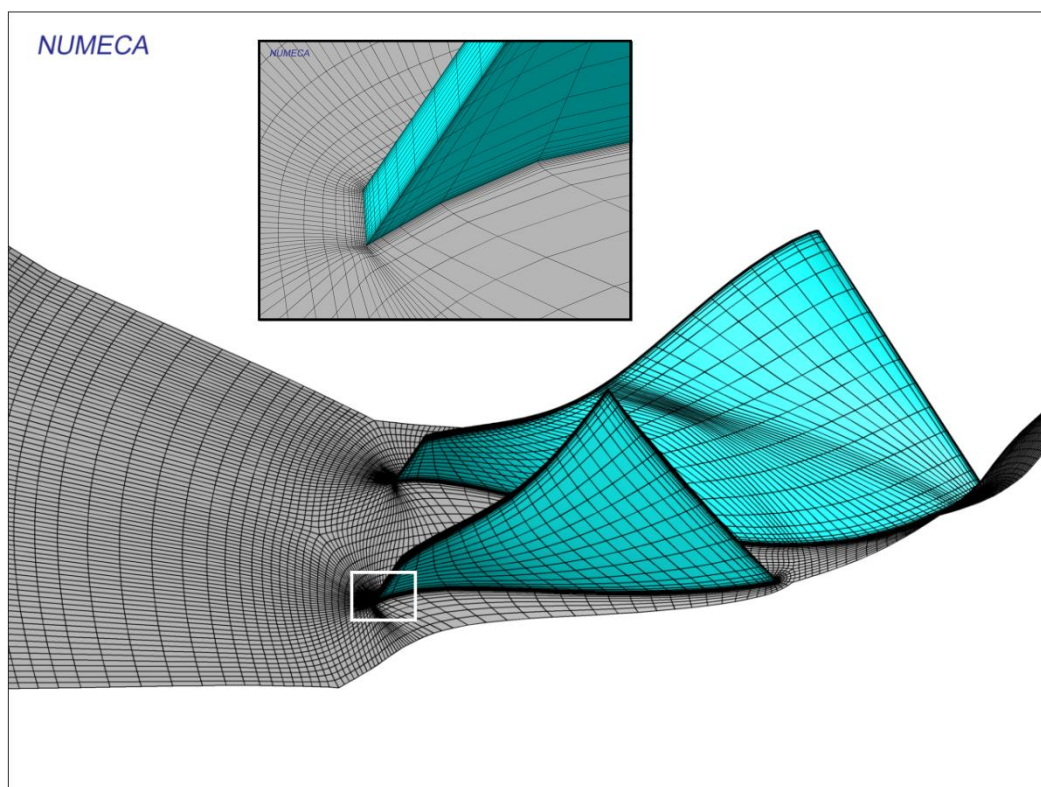


Figure 15: 3-dimensional grid projections on the 2<sup>nd</sup> multi-grid level of a CFturbo design

### 6.2.3. Impeller Performance Evaluation

In the mean-line approach the performance of the impeller is estimated by calculating the theoretical pressure ratio and temperature ratio between inlet of the impeller and the impeller tip. Evaluation of the CFD results was therefore initially also performed at the impeller tip, along the meridional TE position. This was the case for the MATLAB and CFturbo designs. At a later stage in the design (Chapter 7), the evaluation plane had to be shifted 2.5 mm downstream of the impeller tip. To prevent confusion, a quantity evaluated on a plane of constant  $r$  is designated by a subscript which includes  $r$  in brackets, for example the total pressure ratio at  $r = 58$  mm would be  $\Pi_{T-T(58)}$ . A detailed explanation on the post-processing realized in CFView<sup>TM</sup> is given in Appendix D.

### 6.2.4. CFD Model

Fluid and flow model settings were carried over from the CFD analysis of the reference stage. No R/S interface was necessary since the impeller was modelled with a vaneless diffuser passage only. These settings also applied to the CFD simulations completed for the optimization routines discussed in the subsequent Chapters.

The BCs in the CFD model (Table 8) of the mean-line designs were similar to the BCs in the reference stage. The air was to enter axially and the specified total inlet conditions were entered. Discrete values between 150 kPa (choke) and 330 kPa (surge) were assigned to the outlet static pressure to calculate the performance curve.

Table 8: Boundary conditions used for the CFturbo designs

<b>Inlet</b>	<i>Total Quantities Imposed</i>	<i>Velocity direction</i>	$\frac{V_r}{ V }$	$\frac{V_\theta}{ V }$	$\frac{V_z}{ V }$	$p_{01}$ (kPa)	$T_{01}$ (K)	Turbulent viscosity, $\nu_t$ (m <sup>2</sup> /s)
			0	0	1	100	300	0.0001
<b>Outlet</b>	<i>Pressure Imposed</i>	Averaged Static Pressure (kPa)						
		150...330						
<b>Hub, shroud, blades</b>	<i>Solid (no-slip)</i>	shroud	blades		Hub: area defined rotation speed			
		0 rpm	95,000 rpm		95,000 rpm			

The same numerical model was used as in the CFD analysis of the reference stage. The initial solution for the first computation at lowest backpressure was the calculated solution for turbomachinery. The subsequent computations were given the initial solution from the previous computation. For the 1-dimensional solution the inlet initial condition was set to a constant static pressure distribution with a value of 90 kPa. Again the rotating part of the hub was enclosed by a pre-defined area.

### 6.2.5. Results

It was found that the HEP of the original CFturbo design (“design\_5”) features a mass flow at HEP ( $m_{HEP}$ ) around 30% above design specification, as shown in Figure 16. Thus an iterative approach was formulated for the impeller characteristic to reach the required mass flow rate at HEP. The options were to directly scale the model in FINE<sup>TM</sup>/Turbo or to change the design point parameter values entered in CFturbo. Design “d\_5\_scaled\_0925” was obtained by directly scaling “design\_5” in FINE<sup>TM</sup>/Turbo by a factor of 0.925. This design displayed an acceptable  $m_{HEP}$  but a substantial reduction in pressure ratio. The decision then lay between the two designs in which the CFturbo input parameters were changed. The “d\_5\_065” design had a design mass flow defined as 0.65 kg/s instead of 0.85 kg/s. Two inputs were changed to generate the “d\_5\_p4\_063\_mod2” design: The pressure ratio was changed from 4.15 to 4 and the mass flow rate to 0.63 kg/s.

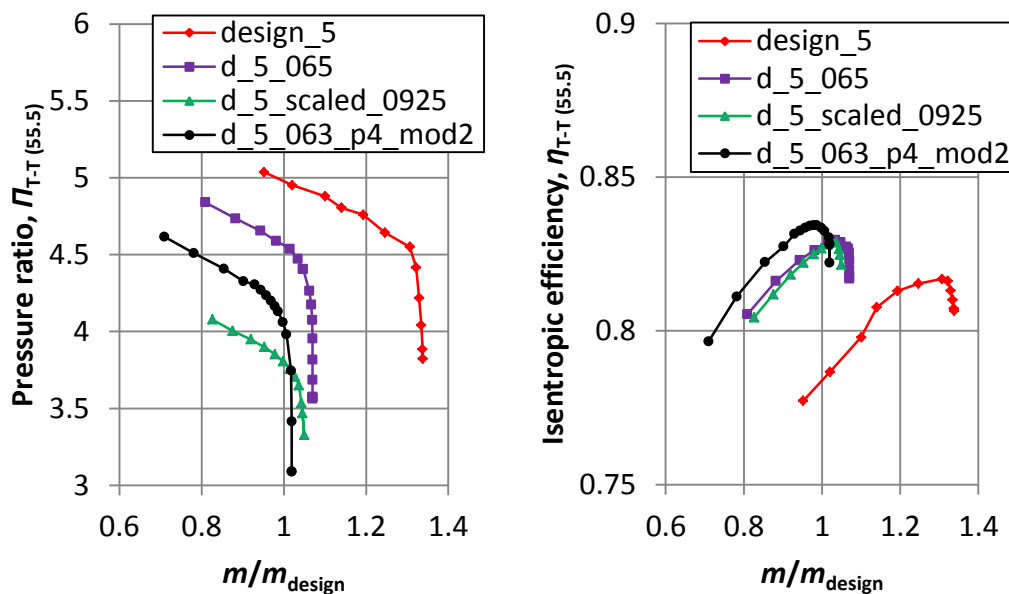


Figure 16: Results of designs generated using CFturbo

The design “d\_5\_p4\_063\_mod2” was chosen over the design “d\_5\_056” because of its higher efficiency. Efficiency was weighted higher than better pressure ratio, since the pressure ratio was close to the specified minimum value of 4.15. In hindsight it can be said that the “d\_5\_065” design was, in fact, the stronger favourite, given that the efficiency of “d\_5\_065” was only 1% higher than that of “d\_5\_p4\_063\_mod2”, but the pressure ratio was 6% lower. The scale on the efficiency axis was misleading. The choke margin was, unfortunately, not a factor considered in this decision.

The chosen design features a pressure ratio of 4.13 and an efficiency of 83.3% at a mass flow rate of 0.83 kg/s and a constant-radius trailing edge of  $r_2 = 55.5$  mm, which reflects a 30% larger radius than estimated in Section 6.1 for a similar pressure ratio and efficiency. The resulting specific speed (EU) was  $n_q = 52$  and the meridional exit angle was  $\alpha_{c2} = 74.5^\circ$ . Table 9 compares mixed-flow compressor designs from literature for perspective.

It can be seen that, given the tip speed  $U_2$  of the CFturbo design, potential exists for an increase in pressure ratio. Also,  $\alpha_{c2}$  15° larger than a typical angle for mixed-flow compressor designs mentioned in recent literature (Ramesh Rajakumar *et al.* (2013a)). The designation of “mixed-flow” may thus be debatable, but  $\alpha_{c2}$  is still 17% smaller than for a radial machine, adding a significant axial component to the velocity.

The FEA of this design was side-lined at the time due to time constraints. Wall- $y^+$  values of the chosen CFturbo design HEP computation can be found in Appendix D.

Table 9: Comparison of various mixed-flow compressor impellers

	$\alpha_{C2}$	$U_2$ (m/s)	$\Pi_{imp(T-T)}$	$\eta_{imp(T-T)}$
Harris <i>et al.</i> (2004)	45	-	-	-
Cevic and Uzol (2011)	50	540	4.34	72%
Ramesh Rajakumar <i>et al.</i> (2013a)	60	528	4.5	90%
Chosen CFturbo	74.5	552	4.13	83%

### 6.3. Conclusion

A mixed-flow impeller design with performance values close to the design specifications was obtained using the commercial 1-dimensional turbomachinery layout tool CFturbo. CFturbo was chosen as the designated layout tool, because designs generated by the in-house mean-line code did not produce designs that performed well enough to be considered for optimization.

CFD analyses showed that the  $m_{HEP}$  of the original CFturbo design exceeded the specified value by 30%. Different approaches were implemented in order to reduce the HEP mass flow rate of the design. A change in CFturbo input parameter values resulted in a design with its  $m_{HEP}$  within 3% of the specified mass flow rate and with an acceptable performance. The meridional exit angle  $\alpha_{C2} = 74.5^\circ$  was chosen by CFturbo according to the specific speed  $n_q$  of the machine, based on values from the Pocketbook for Mechanical Engineering by Dubbel (1997). With the pressure ratio close to the specified value and an efficiency value above 80%, the design is suitable to be aerodynamically optimized.

## 7. AERODYNAMIC OPTIMIZATION

After an acceptable impeller design was obtained from CFturbo, the design's performance was optimized using FINE<sup>TM</sup>/Design3D v 10.05a. This chapter describes how the impeller geometry was defined using lines and Bézier curves linked by control points and their parameters. The fitting of the parametric geometry to the original geometry is outlined. The procedure for determining reasonable parameter bounds is explained before reporting on the database generation, which was based on the design of experiments (DoE) approach. Finally the optimization procedure, which involves teaching of an artificial neural network (ANN) and the implementation of a genetic algorithm (GA), is outlined and results are shown.

### 7.1. The Optimization Process

Optimization is the process of minimizing or maximizing a given function. In the field of turbomachinery the design space is very large and any small change in geometry can have a big impact. In order to search the design space for the best design that adheres to the given requirements, a design may be optimized in three dimensions using CFD. Optimizing in three dimensions ensures an accurate representation of the actual flow conditions if done correctly.

It would be very time-consuming to evaluate the design space using only CFD computations, because thousands of computations would be necessary to define the design space accurately enough to be optimized. FINE<sup>TM</sup>/Design3D thus makes use of an ANN to generate a “response surface”, which is used to predict the performance of different designs and approximate a design space represented by CFD simulations. A database of performance values corresponding to different geometries is used as an input to the ANN. According to Hildebrandt *et al.* (2009), the minimum number of database samples needed for an ANN to be effective is three times the amount of free parameters.

The database is generated following the DoE approach. This approach expands the extent of information included in the database, for a restricted amount of geometries (Montgomery, 2001). During the database generation a parameter value was allowed to take any value in the given continuous range. Each step in the database generation as well as the optimization comprises of smaller steps associated with the CFD-chain as follows:

- Automatic grid generation using a grid-template file (\*.trb)
- Adaptation of BCs and flow solver settings via an *associated computation* which was defined in FINE<sup>TM</sup>/Turbo
- Solving
- Automatic post-processing using a user-defined CFView<sup>TM</sup> macro linked to FINE<sup>TM</sup>/Design3D

The resulting database contains the performance values as well as geometric parameter data of different designs. Once the database has been generated, an optimization routine may be started. Multiple databases may be merged to form a single database. Designs contained in the database obtain a global performance value by using penalty functions. Constraints are specified by the user. The higher a performance value of a design deviates from the requirements the higher the penalty it receives. The penalties for different requirements are weighted and summed to give a single objective function:

$$F = \sum w * \left( \frac{q_{imp} - q}{q_{ref}} \right)^k \quad (7.1)$$

In Equation 7.1  $w$  is a weighting factor,  $q_{imp}$  is the imposed value of the quantity,  $q_{ref}$  is a reference value and  $q$  is the actual quantity value.  $k$  is an exponent determining the behaviour of the penalty function.

The ANN generates the response surface using the objective function values obtained for each design in the database. An optimization routine can now be applied to the response surface. Several optimization algorithms can be chosen in FINE™/Design3D. Given a complex objective function with many varying parameters, the GA is adept in finding the global minimum amongst the local minima (Goldberg, 1989). A GA finds the optimal solution by considering the population of candidate solutions and evolving them to better solutions which form the next generation.

Once the objective function and optimization algorithm have been defined, the optimization process may be started. The performance of the optimized design is then confirmed with a CFD computation. ANN and CFD results are compared and an error for the ANN prediction is calculated. The initial accuracy of the ANN depends on the size of the optimization problem.

The process outlined above is repeated and learning continues for the ANN throughout the optimization process, since the performance of each new design is added to the database used by the ANN. After some cycles the prediction of the optimal design based on the ANN should converge to the CFD-predicted values, which indicates that no better design can be found. Figure 17 illustrates the process discussed. The CFD-chain may be replaced by the FEA-chain or both chains may be implemented simultaneously. The white arrowheads represent a step which is part of the optimization process. Shaded boxes denote the different software packages indicated in italics. Solid lines represent the design steps preceding the optimization.

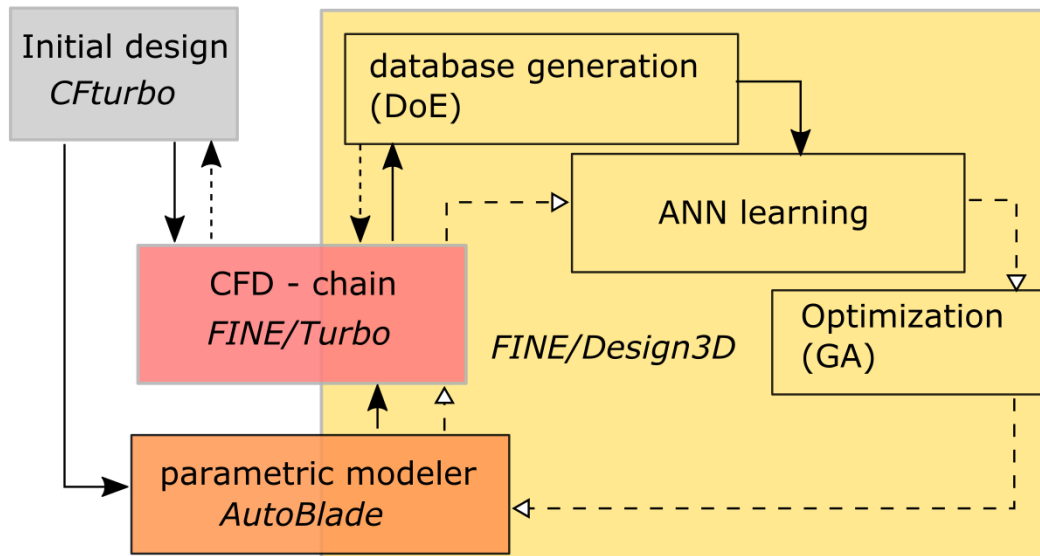


Figure 17: The optimization process in FINE™/Design3D

## 7.2. Parameterization

Parameterization is an important step preceding optimization, since it determines the way the model may be varied (topology), the degree of freedom in the model and the possible design variables. The geometry should be parameterized such that it reflects the target design geometry and accommodates the envisaged freedom. Ideally the parametric model should have as few free parameters (design variables) as possible in order to simplify the optimization problem and reduce optimization time and cost.

For parameterization of the geometry AutoBlade™ was used. The CFturbo design was parameterized by importing the \*.geomTurbo file of the geometry as the *target geometry* into the AutoBlade™ design space (Appendix G) and generating an initial parametric model via a turbomachine-type specific template and an *initialization*. An *initialization* via the *Adapt model* tab estimates parameter values and bounds of the model. Subsequently, necessary changes were made to the parametric model topology. For example, C-splines were changed to Bézier curves to define the camber. The model was adapted after the changes were made using the *Improve* option. The following four definition sets construct the major part of the parametric model of the impeller:

- Endwalls
- Stream surfaces
- Stacking laws
- Main blade camber curves and side curves

These definition sets are discussed in the following subsections.

### 7.2.1. Endwalls

The endwalls define the impeller meridional contours in the  $z$ - $r$ -plane. In this project the endwalls are symmetric about the axis of rotation. The hub nose contour was defined by a C-spline. A Bézier curve with five control points was utilized to define the impeller hub contour. Bézier curves exhibit more gradual changes in gradients compared to C-splines. This makes them ideal for parametric contour and camber definitions.

At the shroud the endwall definition begins with a line. The impeller contour was again defined using a five-point Bézier curve. The diffusing part downstream of the TE and the constriction was defined using straight lines. The endwall control points are shown in Figure 18. Red dots connected by red, dashed lines represent the Bézier control points. The control points were free to move in the directions indicated by the arrows. The endwall control points totalled 18, which adds up to 36 endwall parameters.

No change in discharge angle  $\alpha_{C2}$  was allowed in the optimization due to the resulting increase in free parameters and potential negative effects this change would have on the grid quality. Relaxing  $\alpha_{C2}$  would, however, be a potential factor for future investigation.  $\alpha_{C2}$  was held constant at the impeller tip at hub and shroud by enabling *slope continuity* at the end of the Bézier curve.

### 7.2.2. Stream Surfaces

Figure 18 shows black, dashed curves below the hub curve and above the shroud curve. These curves represent the stream surfaces. The stream surfaces are the segments at which the blade sections are defined. *Linear interpolation surfaces* are typically used for radial turbomachinery and allow blade definition in the  $dm/r$ - $\theta$  plane. To parameterize the geometry, two primary sections were made: one at the hub at -2% span-wise location and one at the shroud at +102%. The *Rulings* were activated. Ruled surfaces allow flank milling of the impeller. A ruled surface is a surface which can be generated entirely by straight lines.

### 7.2.3. Stacking Laws

The stacking point defines the reference point to which the hub and shroud are positioned. It was chosen to be the blade LE. The LE position in the  $dm/r$ - $\theta$  plane can only be changed using the LE meridional position and tangential lean parameters if the endwalls stay constant.

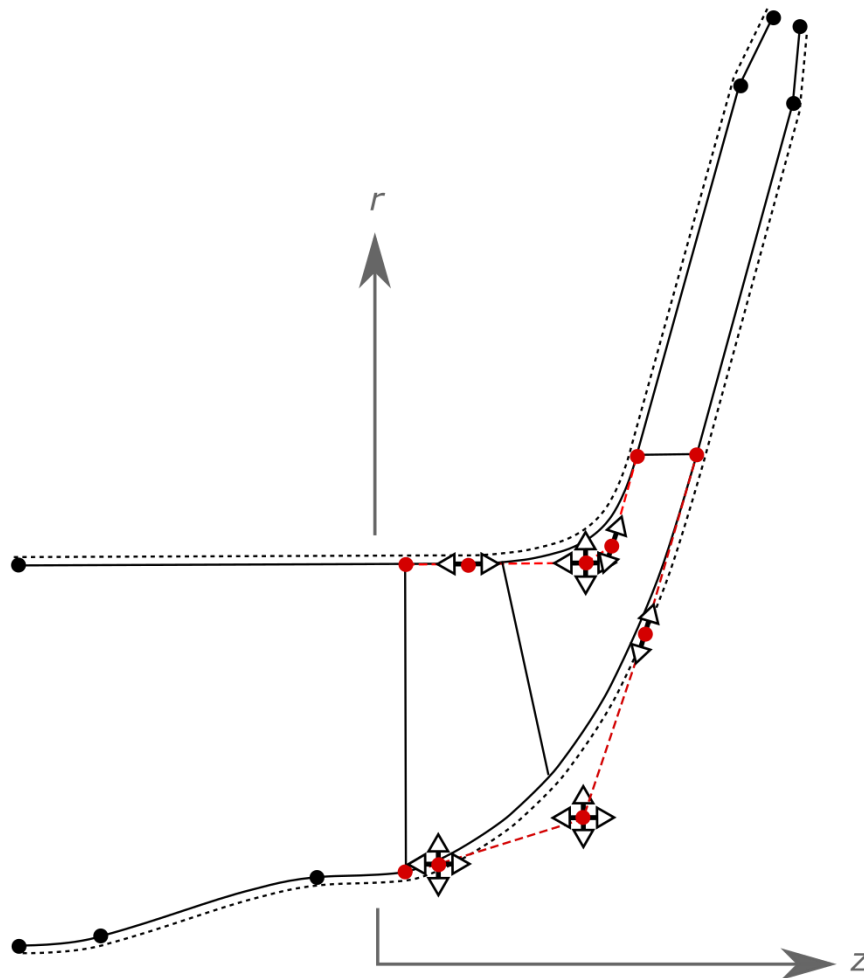


Figure 18: Parameterization of the hub and shroud contours (endwalls)

The main blade LE meridional location was relaxed (free to vary). Additionally, the tangential location parameter LEAN\_BETA was free, which controls the overall blade lean.

#### 7.2.4. Main Blade Camber Curve and Side Curves

The construction plane for the camber curves was the  $dm/r-\theta$  plane. To define the main blade camber curve on the hub and shroud section, a Bézier -curve with six control points was used. The inner points were moved away from the centre and thus toward the edges to improve fitting using the *twice-geometric* distribution with the first and second common ratio equalling 1.5. Blade camber curvature and blade lean are influenced by changes in these parameters. The splitter was set to be a truncated section of the main blade.

No dependencies were established between the hub and shroud Bézier points. This implies that the blade angles were free to differ from LE to TE throughout the blade span. The CFturbo design features the same sweep angle  $\beta_2$  at the TE throughout the blade span. Neighbouring Bézier-points could have been constrained in order to acquire the same blade angle at hub and shroud, but the blade angles were not constrained since that would restrict the design space. Ten camber parameters were relaxed as displayed in Figure 19, with the LE control point being the reference point.

Blade thickness was defined in AutoBlade™ by parameterizing the blade side curves. Symmetric thickness addition was chosen with the camber as reference. A Bézier spline with three uniformly distributed parameters for main and splitter blade thickness was selected. A rounded LE and a blunt TE were enforced, where the TE radius in the meridional plane was set to be constant. No thickness parameters were relaxed, as the aerodynamic optimization is usually commenced with the blade thickness frozen (Hildebrandt *et al.*, 2009) (Demeulenaere *et al.*, 2015).

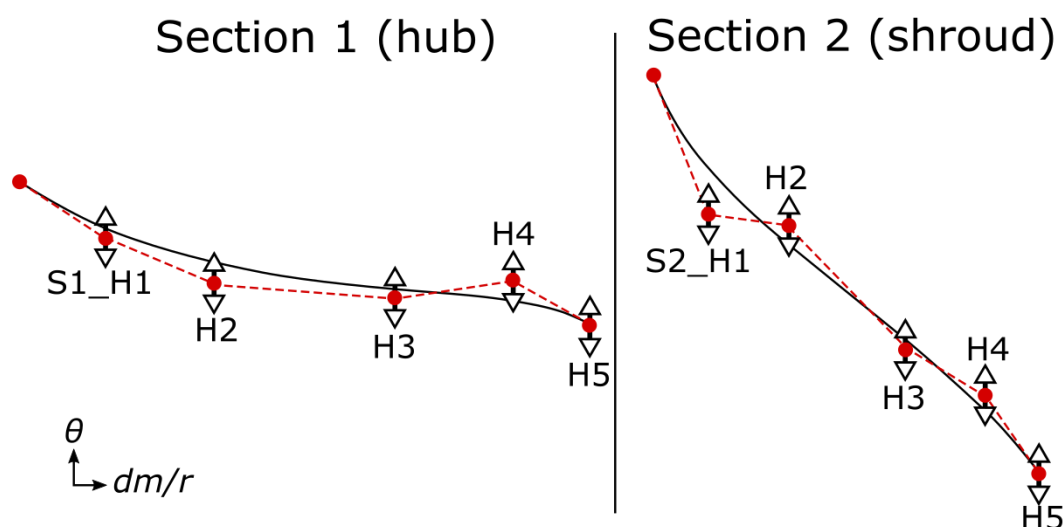


Figure 19: Section 1 and 2 camber Bézier points and associated freedom

The parameters of the final parametric model used in the optimization may be split into seven major groups as listed in Appendix H. A detailed list of the free and frozen parameters is shown in Appendix H.

### 7.3. Fitting

Obtaining a parametric geometry that is closer to the target geometry than it was after *initialization* is achieved through the *fitting* process. Topology and parameter bounds were checked to see if they didn't inhibit the fitting process from

achieving a better fit. A GA was used for the *fitting*. The model was fitted using the *medium* option, as any more optimization steps did not improve the fitting significantly. For the *fitting* the ruled surfaces had to be de-activated.

The blade camber angle  $\beta_2$  at the TE at the hub was not attempted to match perfectly with the target geometry. A better fit could have been achieved using very high values for the geometric common ratios, but the camber curve was rather set to experience gradual changes in gradient to improve flow conditions. When comparing the fitted design with the original design it was observed that the pressure ratio increased by 1.5%, the efficiency decreased by 0.2% and the choke limit was reduced by 2.4%.

#### 7.4. Parameter Value Bounds

The parameter value limits were defined according to visual impression. Parameter values were varied in AutoBlade™ to observe the effect on the geometry. Not all possible geometric variations could be identified, but the procedure gave a good first impression of the possible geometries.

To have a closer look at the geometric possibilities with the specified bounds the parametric modeller was run to randomly generate geometries, as would be done in the database generation process. These geometries could then be analysed and compared by loading the \*.par files into the *Compare Geometries* window in FINE™/Design3D, which makes 2-dimensional comparisons possible. Geometries were also compared in three dimensional space by importing the \*.par files into the AutoBlade™ design environment (Appendix G) and adding overlays. This conveyed a better impression of the blade geometry.

Based on the meridional contours and traces no unrealistic geometries were produced. This is confirmed by looking at some geometries shown in Figure 20, which were generated with the parametric modeller.

An inspection of the B2B sections showed that many different camber shapes could be produced, but once again no unrealistic shapes were generated. The shift in the horizontal axis shown in Figure 21 is due to the change in radius of the hub contour and/or the change in LE meridional position.

A 3-dimensional investigation showed that the blade lean was allowed to be very aggressive at the TE – both towards and against the direction of rotation – as a result of the different possible  $\theta$  positions of the camber Bézier points at hub and shroud. This was left unchanged to enlarge the design space.

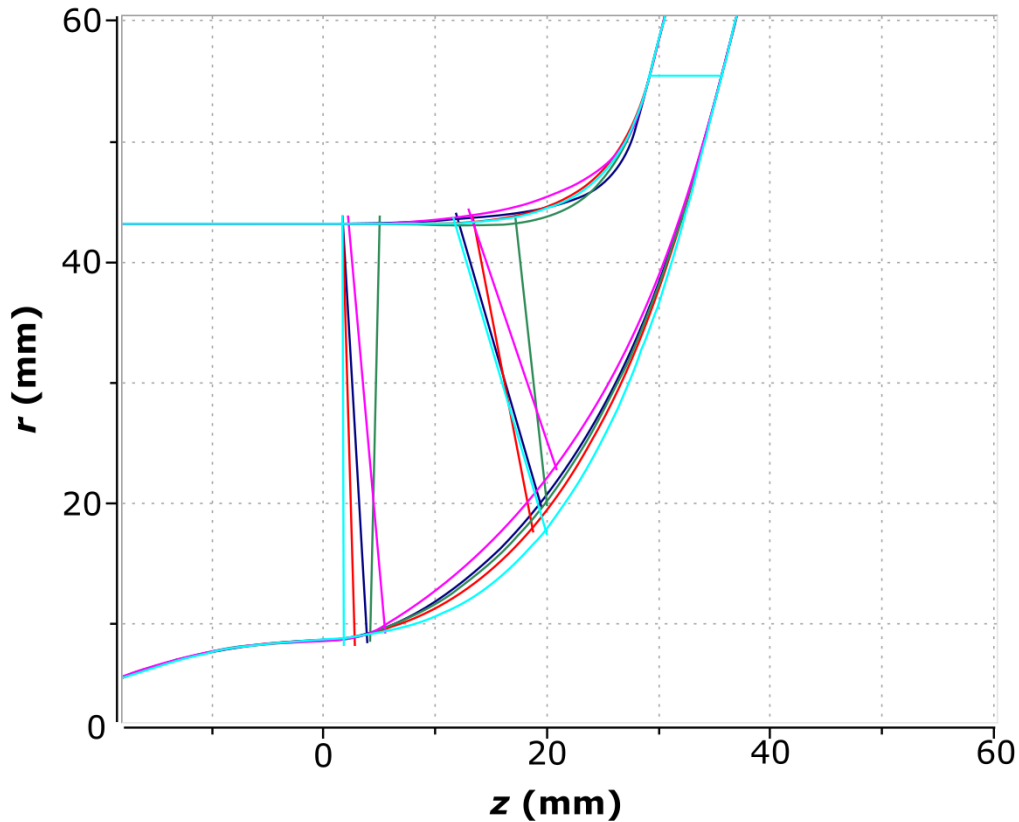


Figure 20: Meridional contours and traces of randomly generated geometries

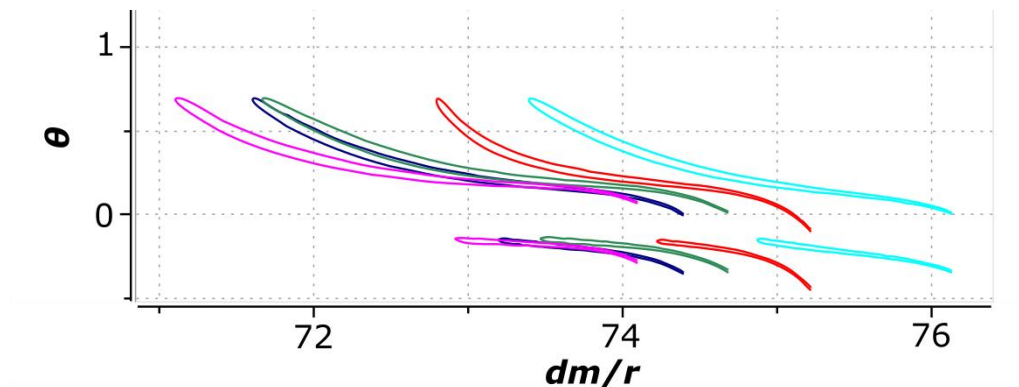


Figure 21: B2B views of possible blade shapes at section 1 (hub)

### 7.5. Operating Points

The operating points to be investigated during the optimization had to be chosen before creation of the database. Only investigating the design point is not a guarantee for a working design, the behaviour at off-design conditions is also critical. Three operating points were chosen to be included (multi-point optimization):

- one point at design conditions (DP)
- one point towards surge at a lower mass flow rate (SP)
- one point at choking conditions at a low backpressure (CP)

By looking at these three operating points, an indication would be obtained of the design and off-design performance at the design rotational speed. A *3D Associated Computation* was selected, which makes it possible to link the CFD model inputs defined in FINE™/Turbo projects to FINE™/Design3D. The SP was run at 95% of the DP mass flow rate which was imposed at the outlet. Placing the SP too close to actual surge might result in unstable computations. Locating the SP closer to the DP ensures stable simulations and allows for a better indication of the highest efficiency mass flow rate  $m_{HEP}$ . The DP was run with 0.83 kg/s mass flow imposed at the outlet as this is the highest efficiency mass flow of the CFturbo design ( $m_{HEP,CFturbo}$ ).

If a mass flow BC is selected, FINE™/Turbo reads the total mass flow input while imposing the mass flow divided by the periodicity. For both mass flow imposed operating points the *velocity scaling* technique for imposing mass flow was used as better convergence was observed compared to the *pressure adaptation* technique. The FINE™/Turbo Manual (NUMECA International, 2014b) notes that *velocity scaling* is not valid for significant backflows at the outlet. Any substantial backflow was prevented by adding a constriction at the outlet. The CP was run with a value of 200 kPa *averaged static pressure* imposed at the outlet. Backflow control was enabled for all operating points. Figure 22 shows the three operating points on the performance curve of the CFturbo design.

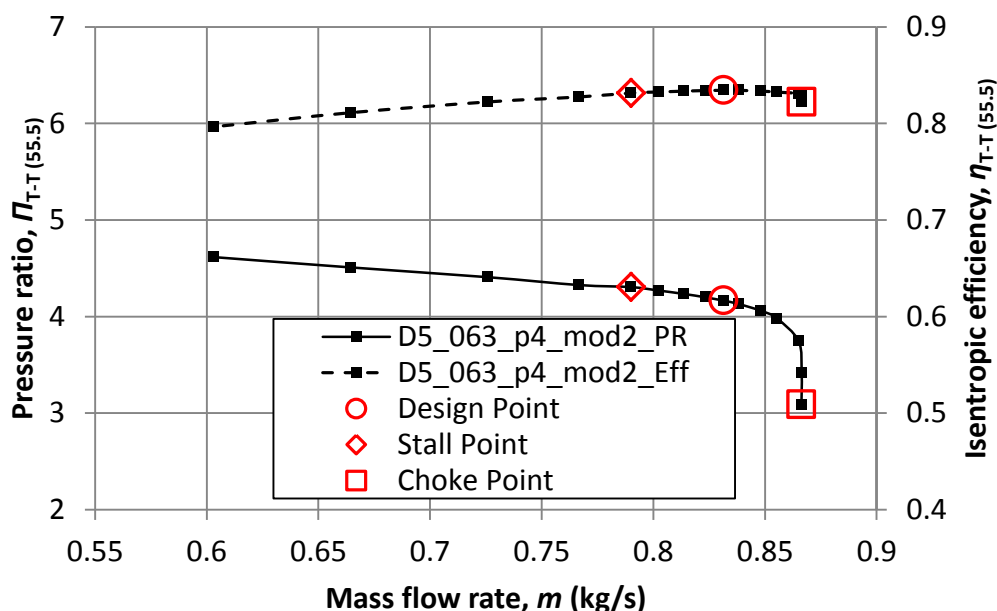


Figure 22: CFturbo compressor performance curves and chosen operating points for optimization (evaluation at  $r = 55.5$  mm)

Table 10 summarizes the three operating conditions.

Table 10: Operating points chosen for the CFD database and optimization

	SP	DP	CP
Outlet BC	0.79 kg/s	0.83 kg/s	200 kPa

## 7.6. Post-processing

In FINE<sup>TM</sup>Design/3D it is possible to implement a user-defined post-processing-macro which will automatically be executed in CFView<sup>TM</sup>. The required quantities are then added to the results file and can be accessed in the FINE<sup>TM</sup>/Design3D GUI.

A macro was written in Python which finds the necessary quantities at a specified location to calculate efficiency and pressure ratio. The efficiency and pressure ratio were calculated using mass-averaged total quantities at constant radius near the trailing edge of the impeller. The same macros were used for database generation and optimization.

## 7.7. Database Generation

After the visual investigation of the different possible designs, the database generation process was started. The database was generated according to the DoE approach. Parameters were chosen to vary randomly between the upper and lower bounds (*Continuous*).

### 7.7.1. Grid Toughness and Quality

The final optimization made use of the results from three database runs: DB01, DB02 and DB03. For DB01 and DB02 the mesh template utilized for the CFturbo design was used. After checking the mesh quality of the two databases, it was found that the grid quality was poor for many geometries. Hence DB03 was started with a new mesh template. The major difference to the grid used for DB01 and DB02 was in the main blade outlet topology type which was set from *low angle* to *normal*. The H-topology at the outlet was also enabled. These changes meant that acceptable grids were created with large and small backsweep angles.

The results of the first database run were compared to those of DB01 and major differences were observed. After an investigation it was found that with the new TE topology the results were not reasonable if the impeller performance was evaluated directly at the TE ( $r = 55.5$  mm). However, the results of three different meshes converged at around 57 mm radius. Thus the evaluation plane was shifted to  $r = 58$  mm. Figure 23 displays the mesh inconsistency at highest efficiency

point of the CFturbo design. It also shows results of the evaluation using the real velocity values used for the mass-weighted average as opposed to the absolute values. The mesh template that replaced the old template was designated “new\_TE\_topology\_1”.

In order to obtain an indication of the robustness of the new grid template, the grid quality of the designs in the three databases is tabulated in Table 11. The quality criteria were relaxed due to the original criteria being too conservative to be enforced in an optimization with geometric freedom of this scale. DB01 and DB02 used the old topology and DB03 the new topology.

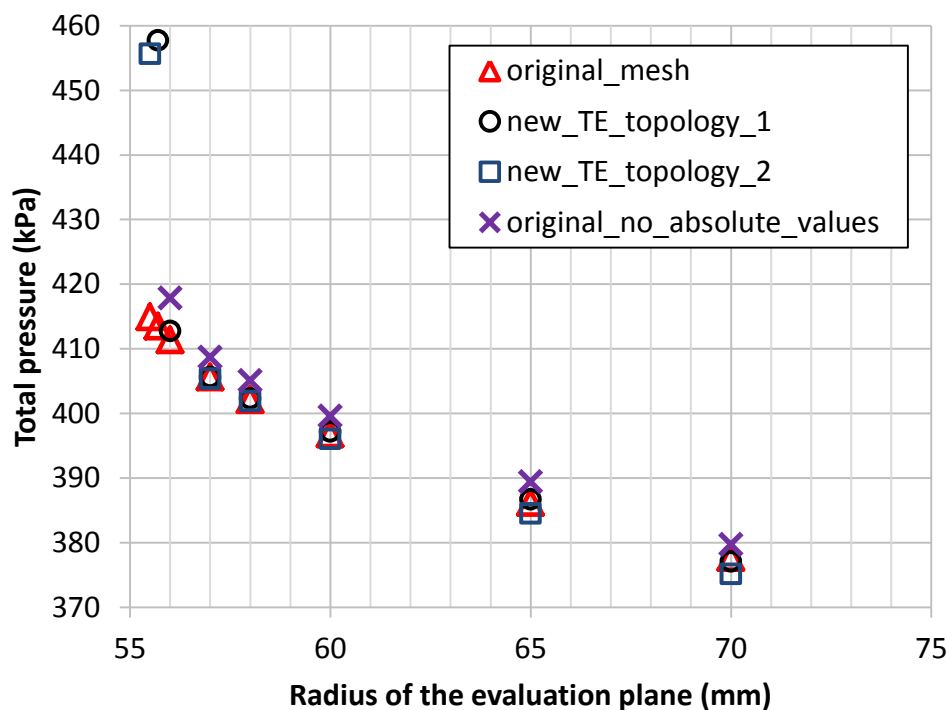


Figure 23: Comparison of mass-averaged total pressures at different radii with different TE topology

Table 11: Final CFD database grid quality

Number of designs	DB01, DB02 cleaned	DB03
in the database	67	77
with maximum aspect ratio >1,000	0%	0%
with maximum expansion ratio >4	5 (7%)	0%
with minimum angular skewness <18°	30 (45%)	4 (5%)
with maximum angular deviation >40°	10 (15%)	2 (3%)

The new mesh template produced only a small percentage of designs which do not meet grid quality criteria as opposed to the old mesh template. The computations of the designs in DB01 and DB02 have still converged, however. For the optimization the new mesh template was judged suitable, considering the results from DB03.

### 7.7.2. Numerical Model

Running the mass flow imposed computations with the CPU booster off added stability. This was not a problem for the CP calculation, which was run with the CPU booster enabled. Table 12 displays the numerical model details for the final database.

Table 12: Numerical model for databases DB01, DB02 and DB03

	CPU boost	CFL No.	Scheme definition	Max. cycles per grid level
DP	No	3	Linear progression	250
SP	No	3	Linear progression	250
CP	Yes	1000	Incr. on higher level	25

### 7.7.3. Results

The numerical convergence of many DP and SP calculations was unacceptable and a number of calculations crashed. This was also the case with the new mesh template. It was found that some designs had a small  $m_{choke}$  – lower than the enforced mass flow of CP and SP – leading to bad convergence. For several designs in the database oscillations in the mass flow had not completely settled within 2000 iterations, but they were consistently reducing in amplitude.

After completion of the first database, DB01 was ‘cleaned’ of invalid designs and designs with small  $m_{choke}$ . This was necessary, since DP results of designs with a smaller choke mass flow than specified by DP are misleading and incorrect. However, designs with a choking mass flow above 0.82 kg/s still produced acceptable convergence and the CP results are accurate. It was decided to include these designs in the final database such that they will be heavily penalised in the optimization and the ANN quickly learns to avoid these designs (Demeulenaere *et al.*, 2015). 34 samples were left in the cleaned database. DB02 was started with a different sample generator coefficient. Invalid designs and designs with  $m_{choke}$  smaller than 0.82 kg/s were also removed from DB02. 32 samples were left in DB02.

DB03 was started with the new mesh template. Some designs in the database were invalid, which meant that either one of the operating points had crashed or has not converged properly. It was found that some crashes of the CP run were caused by the CPU booster. Hence it was switched off in the optimization process. Designs with low choke mass flows were still included in the training database, but only down to 0.82 kg/s. 29 designs were left in DB03. Pressure ratio and efficiency values of all the converged solutions from the combined database are given in Figure 24.

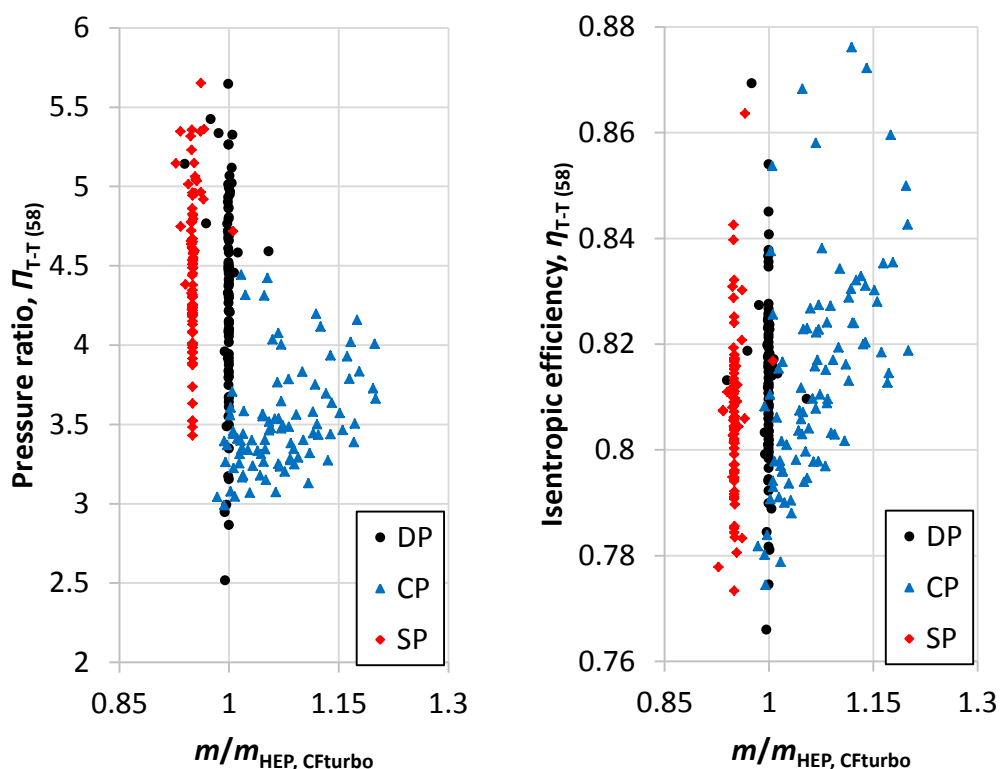


Figure 24: Results of the designs from the final CFD database

Figure 24 conveys the range of pressure ratios and efficiencies in the database of all three operating points. It can be seen that the pressure ratio range is significantly larger percentage-wise than that for efficiency. High pressure ratio and efficiency values do not directly imply that the design conforms to the design criteria. This is made clear by the high efficiency CP values which uncover designs that operate at mass flows far above the design mass flow rate. It can also be seen that at high pressure ratios there are designs where the mass flow did not converge to the imposed value, giving an indication of the stability of the computation and usefulness of the design.

## 7.8. Optimization

After the three databases were cleaned and combined, the *optimization* was prepared. Preparation included the definition of the objective function, setting the appropriate weightings for the penalty terms, configuring the ANN, and choosing the optimization algorithm and number of design iterations.

### 7.8.1. Optimization Settings and Objective Function Definition

A GA was implemented for the optimization step. Fifty optimizer steps were enabled. This ensured optimizer convergence without a significant sacrifice in time. In FINE<sup>TM</sup>/Design3D the objective function to be minimized is defined as in Equation 7.1. In the final aerodynamic optimization penalty terms were based on the following arguments:

- Design Point

At DP the efficiency needed to be as close to unity as possible. An equality constraint was used. The minimum pressure ratio at DP was determined to be 4.2 to allow a pressure ratio loss across the diffuser of 15% (as observed with the reference stage). A maximum deviation of the mass flow at the inlet  $m_{in}$  of 2% from the mean in the last 500 iterations was allowed at DP.

- Choke Point

Designs that choke below the design mass flow of the CFturbo design had to be penalised: A minimum mass flow rate of 0.84 kg/s at CP was enforced. Additionally, designs with a higher mass flow than 0.9 kg/s had to be penalised. This limited the highest efficiency point mass flow rate. The value is based on the database results.

- Stall Point

A maximum deviation of  $m_{in}$  of 5% from the mean in the last 500 iterations was allowed.

- DP-CP relative efficiency

After inspecting the database results, it was determined that many designs had a higher CP efficiency than DP efficiency. To ensure that the HEP exhibits a smaller mass flow than the CP, it was decided to not allow the CP efficiency to be higher than DP efficiency. The database results show a trend towards higher mass flows at highest efficiency point. The SP efficiency was always lower than the DP efficiency.

- SP-DP relative pressure ratio

A negative slope of the pressure ratio towards surge had to be guaranteed. A positive slope is generally associated with dynamic instability (Hill and Peterson, 1992). Therefore the SP pressure ratio had to be equal or larger than the DP pressure ratio.

Penalties were assigned if design performance did not adhere to the constraints shown in Table 13. Evaluation of performance was done at a constant radius of 58 mm.

Table 13: Imposed quantity values for the CFD optimization objective function

Quantity	Imposed Values				
	Stall Point (SP)	Design Point (DP)	Choke Point (CP)	DP - CP	SP - DP
$\eta_{T-T}$ (58)		1 EQUAL		0 MIN	
$\Pi_{T-T}$ (58)		4.2 MIN			0 MIN
$m$ (kg/s)			0.84 MIN 0.9 MAX		
$m_{in}$ deviation	0.05 MAX	0.02 MAX			

The final setting of the weightings and reference values evolved during the optimization by suspending, manual checking, adapting and re-starting. Several optimization runs were started in order to investigate where the optimizer is heading and the following questions were asked:

- Have the computations converged properly?
- Is the optimizer producing better designs according to the objective function? If yes, have the designs improved? If not, does the optimizer penalise improved designs?
- Do the improved designs adhere to all geometric and performance constraints?
- Do the improved designs produce reasonable performance curves, judging from the three calculated operating points?
- Are any parameter bounds reached? If yes, would it make sense to increase the given range of the respective parameter?
- Based on the above, does the objective function need to be adapted?

In the final optimization the aim was a penalty value of 0.2 for a highly undesirable quantity value, subject to designer estimate of importance. A table of the weightings is given in Appendix I.

The grid quality of the designs generated during the final optimization was within the margins given in Table 11 for more than 98% of the designs. This again proved the robustness of the grid which was changed during the database generation.

### 7.8.2. Numerical Model

The CPU booster was turned off for the CP calculation due to problems encountered while generating the database. For mass-flow imposed outlet boundaries (DP and SP) faster convergence was observed with the *Increase on higher level* sweep scheme definition. Hence the option was enforced for DP and SP during optimization. It was also enforced for the CP during optimization, with no noticeable negative effects.

### 7.8.3. Results

The ANN converged after ca. 75 iterations. ANN convergence is displayed in Figure 25. Due to the large amount of parameters, the parameter value ranges and the relatively complex objective function, the necessary optimization steps for convergence were more than the expected 40 (NUMECA International, 2014e).

Some critical parameter value bounds were reached during the optimization and the bounds of S1\_CAMBER\_H2, S2\_CAMBER\_H2 and Z\_LE\_SHROUD were adapted. Meridional lengths changed accordingly.

Figure 26 compares the B2B sections at the hub and shroud in the  $dm/r-\theta$  plane of the CFturbo and aero-optimized designs. Important to note is that the aero-optimized curves were shifted in the horizontal axis for better comparison. It can be seen that the LE blade angle  $\beta_1$  has increased relative to the horizontal at hub and shroud. The meridional length of the blade has also decreased.

Due to the parameter bounds set for the optimization, the shroud radius of the impeller was allowed to decrease somewhat with increasing  $z$ . This was observed while analysing the database geometries, but the implications were only realized after the optimized design was found: If the decrease in radius was more than the tip gap, the housing could not slide over the impeller. Therefore the shroud radius at the inlet was manually reduced from 43.2 mm to the lowest value on the shroud curve (42.934 mm (-0.6%)) while ensuring the rest of the contour remained unchanged. The effect of the change in radius on the performance was insignificant (<0.2%). Figure 27 contrasts the CFturbo design meridional contour and the final adjusted optimized meridional contour.

Evident in Figure 27 is the shift in meridional location of the main blade LE and splitter blade LE, both shifting towards the positive  $z$ -direction and thus reducing the meridional length of the blades. The hub curve radius also increased notably towards the location of the splitter.

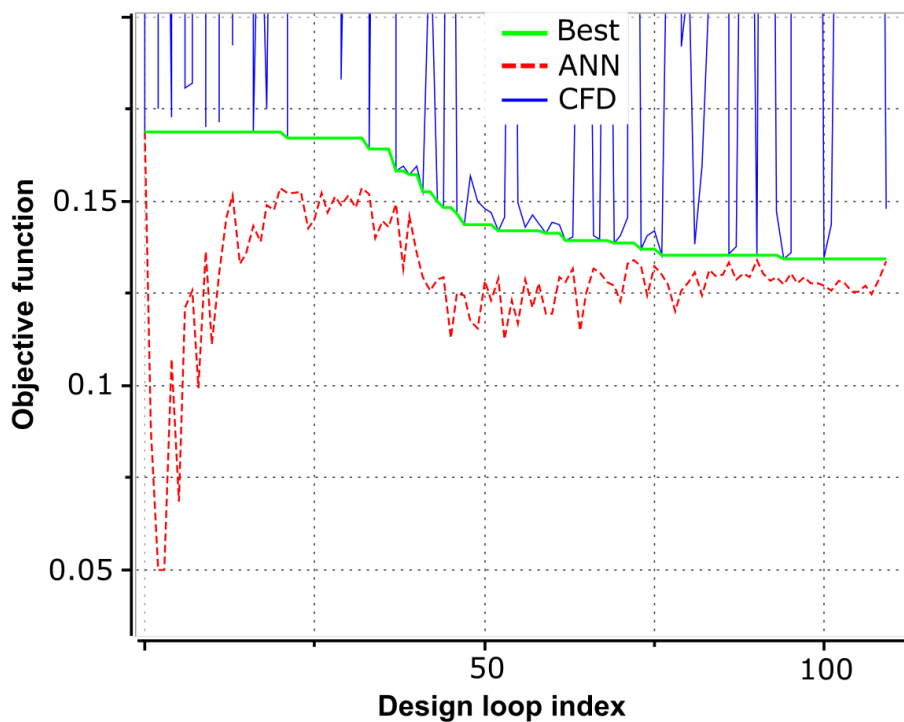


Figure 25: ANN convergence of the CFD optimization

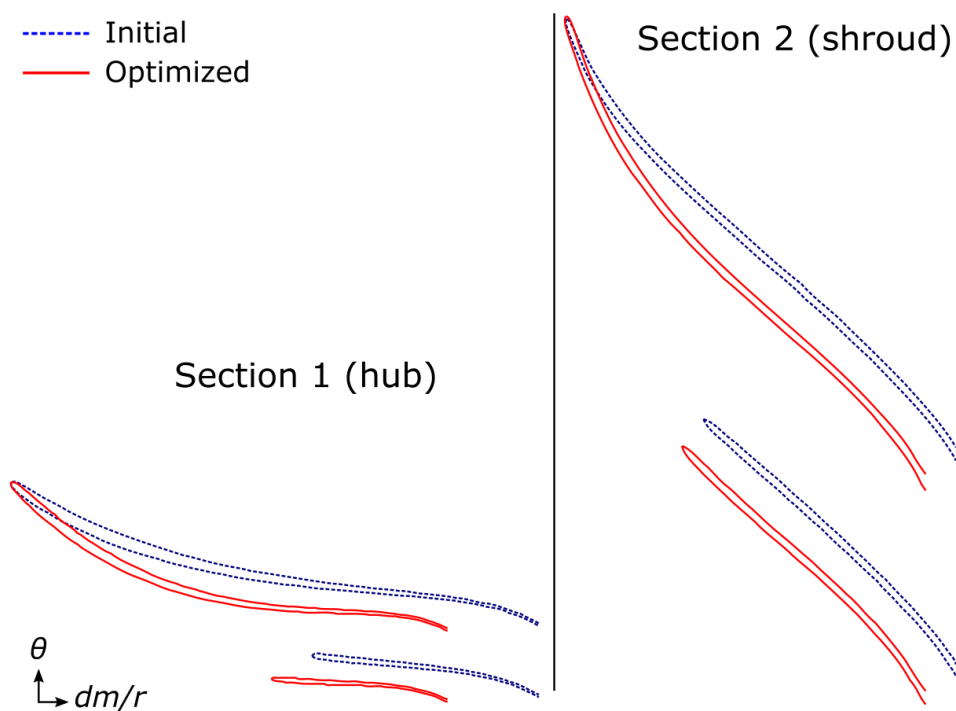


Figure 26: Initial fitted and optimized blade geometry at section 1 and 2

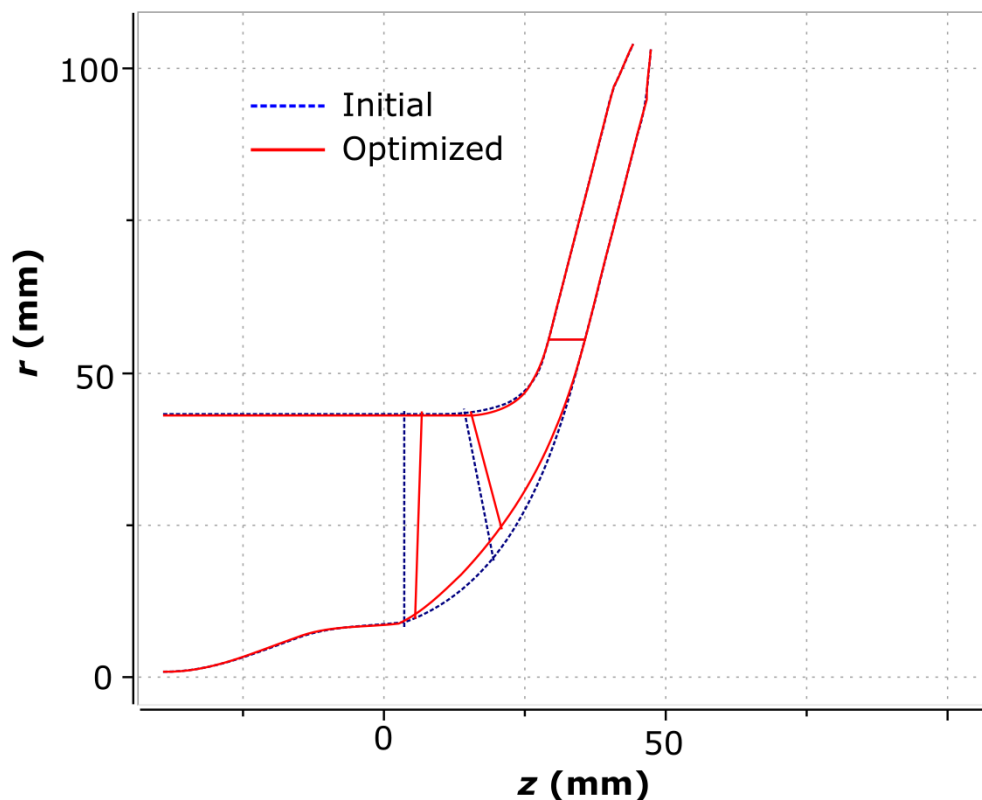


Figure 27: Comparison of initial and optimized meridional contours and locations

A comparison of the initial CFturbo and the final aero-optimized design is shown in Figure 28. The design point is achieved well in the optimized design. Additionally, an increase in pressure ratio of 15% compared to the initial design along with an increase in efficiency of 4.6% was achieved. The actual optimization process achieved an increase in pressure ratio from 4.21 to 4.62 (+9.7%) and an efficiency increase from the best value in the database of 82.8% to 85.6%. Table 14 compares the performance of the best database design and aero-optimized design with the CFturbo design. The percentage increase relative to the CFturbo design is given in brackets. The surge margin (Equation 2.16), which was not a constraint in the optimization, was reduced from 30% (CFturbo) to 16% (aero-optimized). This is still more than acceptable if compared to van der Merwe's (2012) value of 10.9%.

Table 14: CFturbo, best database design and optimized design performance comparison at HEP

	CFturbo	Database best	Aero-optimized
Pressure ratio, $\Pi_{T-T(58)}$	4.02	4.21 (+4.7%)	4.62 (+14.9%)
Efficiency, $\eta_{T-T(58)}$	81.0%	82.8%	85.6%

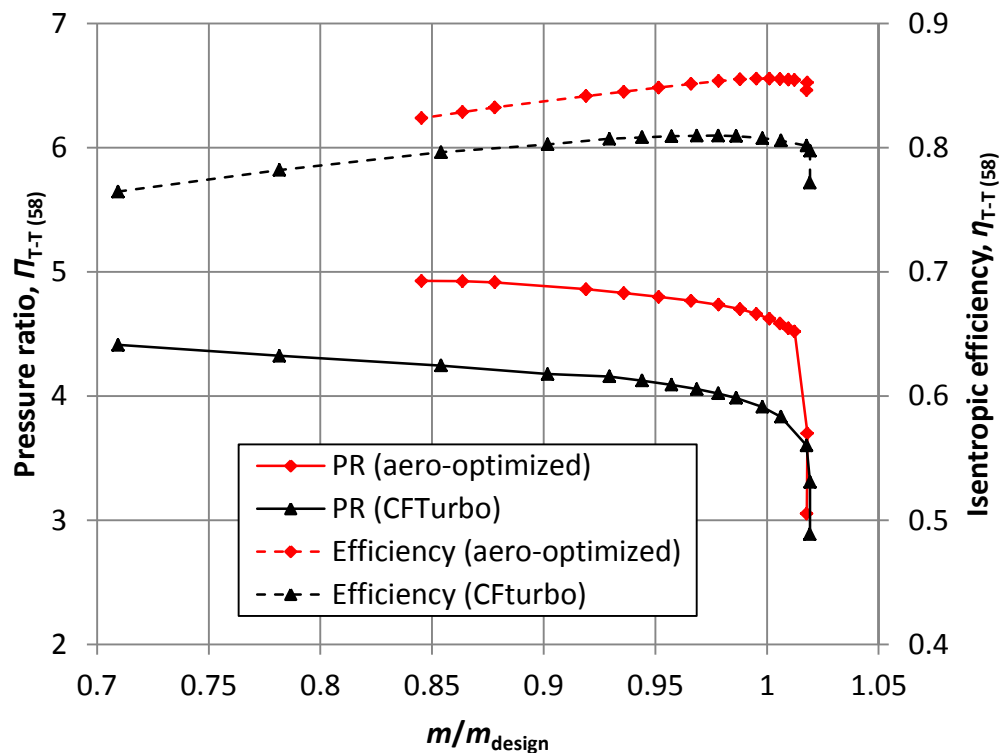


Figure 28: Initial and optimized design performance curves at design speed

## 7.9. Conclusion

A multi-point aerodynamic optimization of the CFturbo design was completed using FINE<sup>TM</sup>/Design3D. The CFturbo design was successfully parameterized and fitted. Parameter value bounds were carefully selected. Database geometries were investigated visually before commencement of the CFD-chain. The initial mesh was found to be weak in terms of quality for different geometries. A new, robust mesh template was generated. The evaluation plane radius was changed due to inconsistencies experienced when evaluating directly at the TE radius. Convergence problems were encountered in the database even with the robust mesh. This was attributed to the fact that  $m_{choke}$  was smaller than the imposed  $m_{DP}$  for some database samples. Through the optimization process a gain of 15% in pressure ratio was acquired at HEP and the efficiency was increased by 4.6%. The next step in the development process was to confirm the structural integrity of the aero-optimized design and, if necessary, complete a mechanical optimization.

## 8. MECHANICAL OPTIMIZATION

In order to ensure the impeller's structural integrity, the finite element (FE) kernel integrated in FINE<sup>TM</sup>/Design3D v. 9-1.3, called OOFELIE, was applied for the structural simulation under radial acceleration loads. It was found that the von Mises (VM) stresses of the aerodynamically optimized design exceed the acceptable limit in the main blade as well as in the impeller disk. The aim of the structural optimization was to reduce the maximum VM stress to below 300 MPa while preserving aerodynamic performance.

The VM stress is an equivalent value for the complete overall state of stress. It can be compared to the material yield strength to indicate if yielding would occur for the given stress state. The VM stress is derived from the distortion-energy theory for ductile materials (Budynas and Nisbett, 2011).

The material stresses are influenced by the centrifugal load, the aerodynamic load and also thermal effects. However, in this analysis only the centrifugal load was considered. As mentioned by van der Merwe (2012), aerodynamic loads are typically used for fatigue analyses, which are beyond the scope of this project. Based on the work of Demeulenaere *et al.* (2015) a maximum VM stress target of  $\sigma_{VM,max} = 300$  MPa, which was also recommended by NIB, was set. This being a very conservative value, the peak VM stress was allowed to reach 380 MPa if 300 MPa could not be achieved. This value was based on the successful testing of van der Merwe's (2012) aluminium impeller with a predicted  $\sigma_{VM,max}$  of 380 MPa.

An approach was devised to obtain a well-performing, structurally sound design. This approach is based on current literature by Demeulenaere *et al.* (2015). The following steps were envisaged:

- Disable the ruled-surfaces enforcement (software limitations).
- Reduce disk stresses using only a database of different impeller backface designs.
- Optimize the blade stresses to ideally reduce to disk stress levels.
- Confirm the aerodynamic performance of the optimized design.
- If necessary, commence a coupled CFD-FEA optimization.

The constraint in the optimization was the global maximum VM stress. It was not possible to define a stress location which could be included in the objective function. Hence the optimization was split into two steps, which form task 2 and 3 in the list above: The disk stresses were to be reduced using a database, such that the blade stresses may be reduced as far as possible in the optimization process, before the maximum stress relocates to the disk.

### 8.1. Parameterization

The impeller disk contour was defined using eight control points and thus a total of 16 parameters, shown in Figure 29 in the meridional view. The disk was defined by four lines and one Bézier curve with four control points in red. Dependent parameters are linked via a dashed line. The  $z$  next to the dashed line indicates that the  $z$ -direction-parameter of the control point was the dependent parameter.

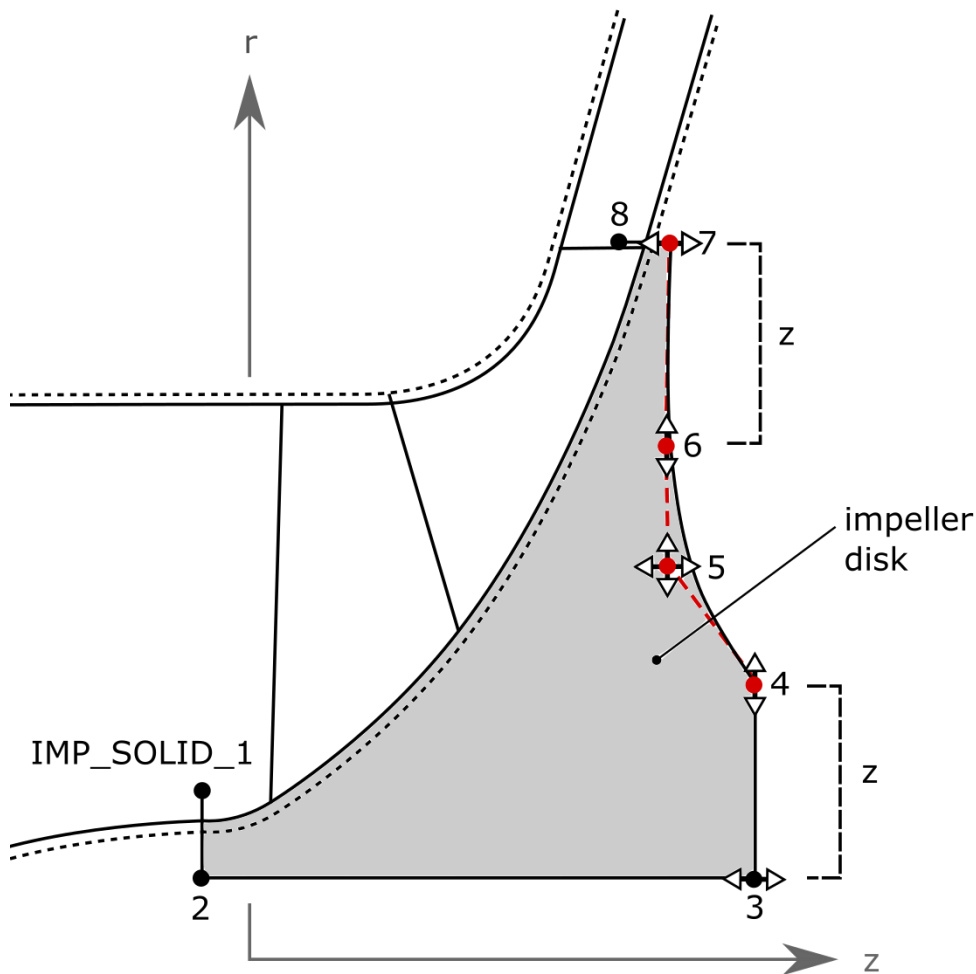


Figure 29: Parameterization of the impeller solid sector in the meridional plane

A fillet was added to the blade roots by activating the *blend parameters* and enabling the *constant radius* setting. An initial fillet radius,  $r_{fil}$ , of 0.5 mm lead to a large number of cells required to mesh the fillet. The fillet radius was therefore provisionally increased to 1 mm.

In Appendix J a shaft-stress calculation is given which was completed to determine a provisional value for the bore diameter. The torque obtained from the

aero-optimized design's CFD results was utilized. With the material selected as mild steel, a shaft diameter of 10 mm was calculated with a safety factor of two.

The blade thickness parameters were uniformly distributed along the camber. Bézier splines formed the blade side curves (pressure and suction side), which consisted of the following three parameters:

- radius at the leading edge
- half-thickness in the middle of the blade and
- half-thickness at the trailing edge

Thickness addition was selected as *symmetric*. The splitter blade thickness values were aligned with the main blade thickness in order to keep the number of free parameters to a minimum. All other parameters were frozen at the aero-optimized designs' values.

## 8.2. Discretization

HEXPRESS<sup>TM</sup>/Hybrid automatically generates 3-dimensional elements of mixed nature: tetrahedrals, hexahedrals, prisms and pyramids. According to the file containing the mesh and element details (\*.fea.mesh.e) all elements are linear: The tets have four nodes, the pyramids have five nodes and so on. This was deduced from the *Propoelem* definition, which declares the elements in the mesh file.

When running an FEA in FINE<sup>TM</sup>/Design3D, the solid model is exported as ParaSolid (\*.xmt\_txt) and then automatically meshed using HEXPRESS<sup>TM</sup>/Hybrid. Only a periodic section of the impeller is modelled, which provides good correlation with the full model results (linear static analysis) but decreases the computational prowess necessary and time expended significantly (Valakos *et al.*, 2007).

A cell count of around 380,000 to 400,000 was obtained in the database. Refinements at the fillets, blade pressure and suction side as well as the blade tip were enabled. No negative jacobians, concave, twisted or negative cells were obtained. The maximum equiangular skewness was around 0.9 and the maximum expansion ratio 12.

The *automatic projection check* had to be switched off. *General face accuracy* as well as *periodic face accuracy* were set to 2. These values are in the same unit as the AutoBlade<sup>TM</sup> geometry, which is in millimeters. *Maximum equiangular skewness* was set to unity in order for the software to accept the grid quality. Geometry units had to be set to millimetres. The mesh is however scaled to meters before it is transferred to OOFELIE (NUMECA International, 2014e).

### 8.3. FE Model

To create the solid model, the rulings, which enable flank milling of the impeller, were initially switched off.

A number of materials eligible for the impeller are compared in Table 15. Inconel was suggested by the CSIR. Al 7075 (in bold, also called *Ergal*) is the material used by van der Merwe (2012). *Ergal* is readily available and relatively cheap, and was also the material of choice in this thesis. A particularly strong aluminium alloy and a common titanium alloy are included for comparison. Some fatigue strengths are also shown, but depend on the number of cycles and therefore values have many different ranges.

Table 15: Various potential impeller materials and their properties

Material	Density (kg/m <sup>3</sup> )	Modulus of Elasticity (GPa)	Poisson's ratio	0.2 % yield strength (MPa)	Fatigue Stength (MPa)
Inconel 718SPF	8200	205	0.284	829-1293	-
<b>Al 7075-T6</b>	<b>2810</b>	<b>71.7</b>	<b>0.33</b>	<b>500</b>	<b>159</b>
RSA-7034 T6	2890	71	-	730	425
Ti-6Al-4V (G5)	4430	113.8	0.342	880	240-600

Material Property Data. [Online]. Available: [www.matweb.com](http://www.matweb.com). [2015, July 5]

The material was modelled as isotropic and homogeneous. A rotational speed of 95,000 rpm was defined, resulting in a tip speed of 552 m/s. Boundary conditions for symmetry and rotational load were applied automatically by FINE<sup>TM</sup>/Design3D. Thereafter OOFELIE solved the matrices for the unknowns. Cyclic symmetry implies the displacements and stresses on one periodic surface are the same as on the other periodic surface, which was implemented by OOFELIE. For OOFELIE to support non-matching grids on the periodic faces, an integration scheme is used (NUMECA International, 2014e).

### 8.4. Impeller Backface and Bore

Disregarding the impeller blades, the highest stresses in the solid sector occurred at the bore. A curved backface has shown to significantly reduce bore stresses compared to a straight radial backface (Valakos *et al.*, 2007). An improvised curve was thus initially defined to describe the backface. To further reduce the bore stresses, a database was created with only the backface parameters relaxed (impeller disk control points 3 to 7).

Zheng *et al.* (2012) make it clear that the parameters relaxed in the database generation play an important role in relation to the bore stress. The bore diameter

had to be kept fixed, however, which according to Zheng *et al.* (2012) has a significant influence on the bore stress.

#### 8.4.1. Database Generation

The final backface design was a result of the investigation of several databases, each database having undergone some changes in parameter value ranges based on the results from the previous database. In Figure 30 some of the resulting database geometries are shown.

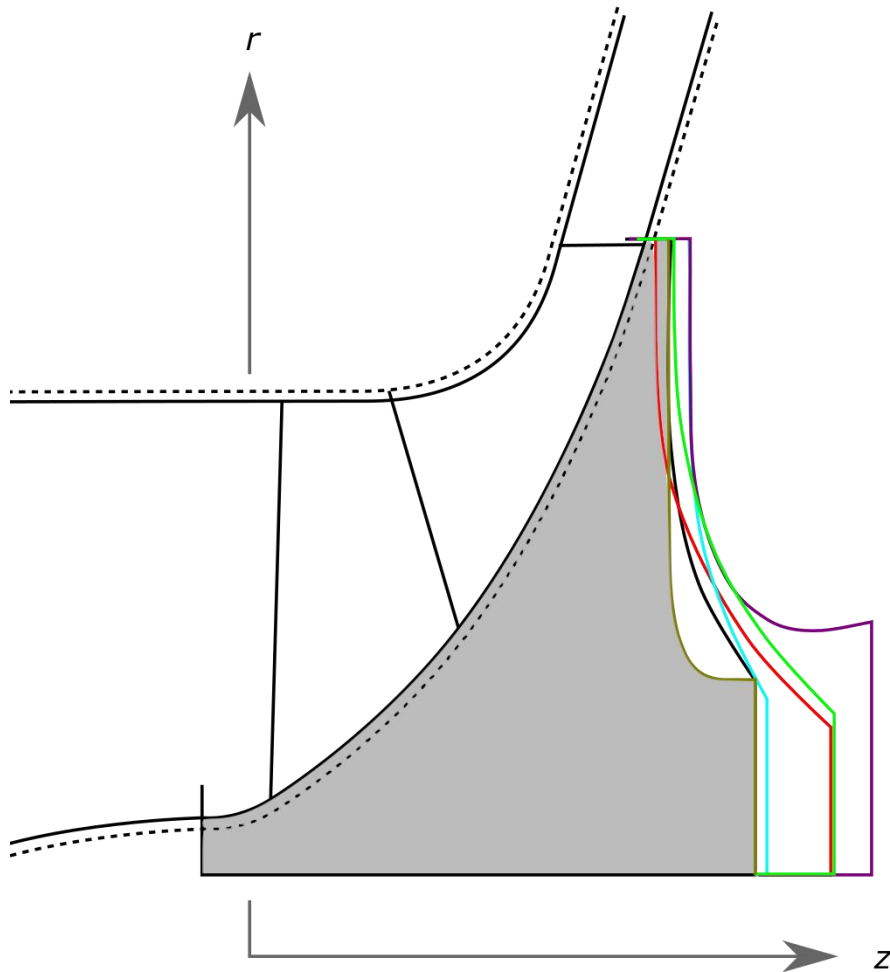


Figure 30: Various geometries obtained in the impeller backface database

#### 8.4.2. Results

Bore stresses were not reduced to 300 MPa in the database and thus an undercut was considered. Investigating the results made it clear, however, that an undercut increases blade stresses towards the TE as well as stresses on the impeller

backface. Additionally, van der Merwe (2012) reported on unacceptable impeller tip deformations as a result of an undercut. With this in mind it was decided to continue without an undercut.

The best database design without undercut had a peak bore stress of 362 MPa (Figure 31, right) compared to the initial 425 MPa (left). This represents a 15% decrease in bore stress. The backface stresses were below 300 MPa.

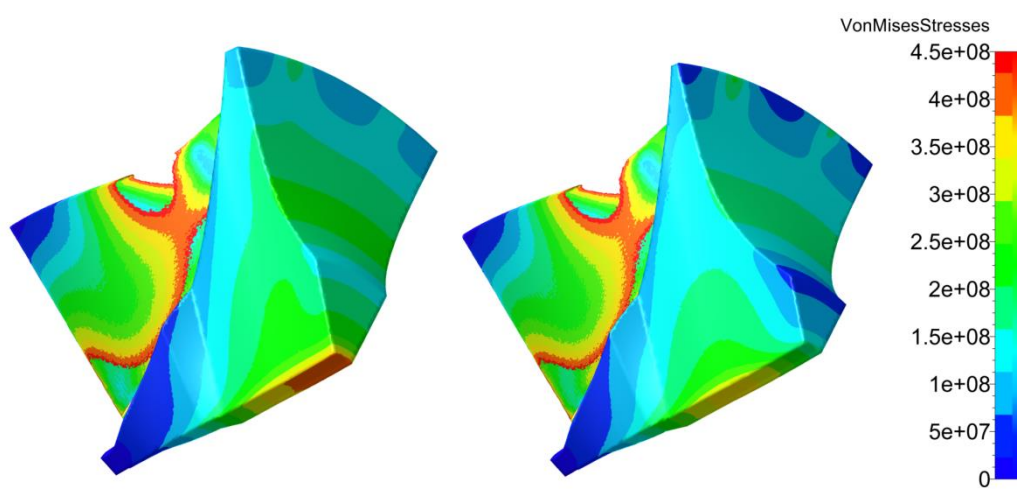


Figure 31: Initial backface design (left) and best database result

## 8.5. Impeller Blade

The main blade stresses exceeded the acceptable limit by a large margin. Consequently the blade stresses were to be optimized while preserving aerodynamic performance.

### 8.5.1. Database Generation

A database was generated with fixed backface parameters. All six main blade thickness parameters as well as the shroud camber parameters H2 and H3 (as shown in Figure 19) were relaxed. The other three shroud camber parameters were left frozen, since they were further away from the high stress location. The influence of blade inlet and outlet angle on aerodynamic performance was expected to be large, which did not encourage the relaxation of these parameters. The inducer shroud radius,  $r_{1s}$ , was also relaxed.

### 8.5.2. Optimization Settings and Objective Function Definition

A GA was implemented for optimization. The only penalty term was that of the maximum VM stress, which was given an equality constraint of 300 MPa with a weight of 2 for a quadratic penalty function and a reference value set equal to the

constraining value. The small number of free parameters and the simple objective function meant the number of optimizer steps for each iteration could be set to *coarse* (25 steps), since optimizer convergence was fast.

### 8.5.3. Optimization and Results

Two optimization runs were completed. In the first optimization the blade thickness was reduced to below 0.5 mm at the LE. This was unacceptable from a manufacturing point of view, and therefore the second optimization was started with a 0.5 mm thickness lower bound. In the first optimization the optimizer also decreased  $r_{1s}$  due to its influence on  $\sigma_{VM,max}$ . As a result  $m_{choke}$  and  $m_{HEP}$  were reduced, as confirmed by a CFD computation, which is why  $r_{1s}$  was changed back to its original value and was frozen in the second optimization.

In order to force the optimizer to produce better results, the stress objective was set to 250 MPa. The optimized design showed peak VM stress of 430 MPa at the tip and root of the main blade. ANN convergence was almost instant due to the small number of design variables and constraints. The blade thickness distribution is compared in Figure 32. Due to the side curves consisting only of three parameters, the optimizer reduced the stresses at the peak stress location by raising the TE thickness, resulting in a continuous increase in blade tip thickness from leading to trailing edge.

Investigating the FEA results showed that the peak stress was situated at the tip as well as the root of the main blade. The optimizer was not able to reduce these stresses any more by only varying the shroud thickness parameters. Therefore other parameters needed to be considered.

The hub blade thickness was previously limited to 2 mm, because it was known to reduce the mass flow capabilities (due to a reduced throat area). Hence the hub blade thickness limit of 2 mm was not increased.

Another option to reduce the stresses was to increase the fillet radius  $r_{fil}$ . The effect of the fillet with a radius  $r_{fil} = 1.85$  mm on the pressure ratio is documented by van der Merwe (2012): a maximum deviation of only 2.5% was obtained between numerical and experimental results. No efficiency data was available. Hence  $r_{fil}$  was changed to 1.85 mm.

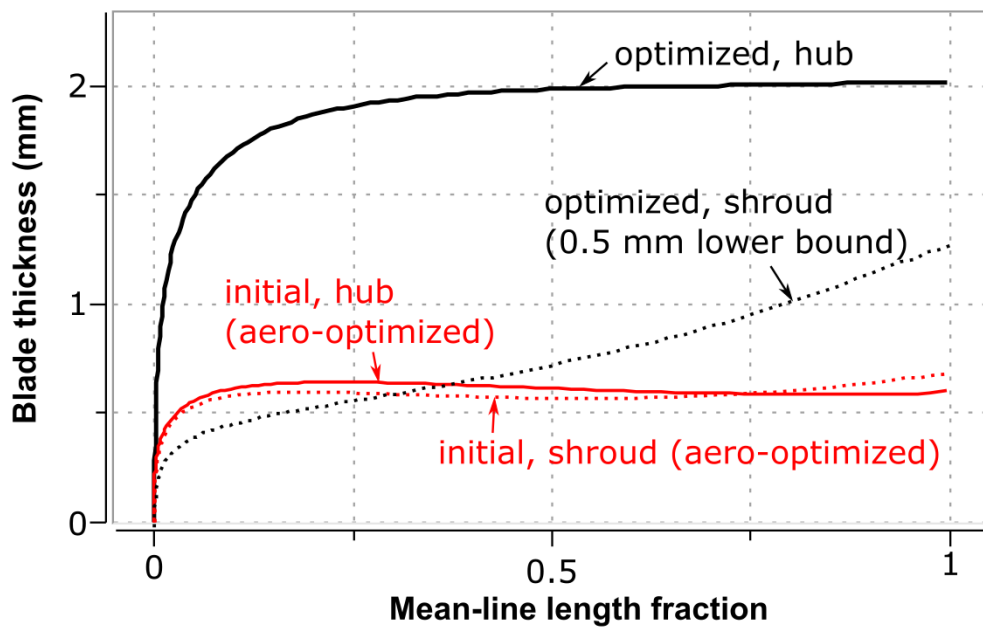


Figure 32: Hub and shroud blade thickness of the aero-optimized and mechanically optimized designs

Using a fillet radius of  $r_{fil} = 1.85$  mm reduced the stresses significantly. The blade root stress and also the blade tip stress values dropped. As a result, the bore stress peaked at 377 MPa and the blade tip and root stresses were somewhat lower (370 MPa). The results of the blade thickness optimization are shown in Figure 33, where the aero-optimized design and the structurally optimized design are compared.

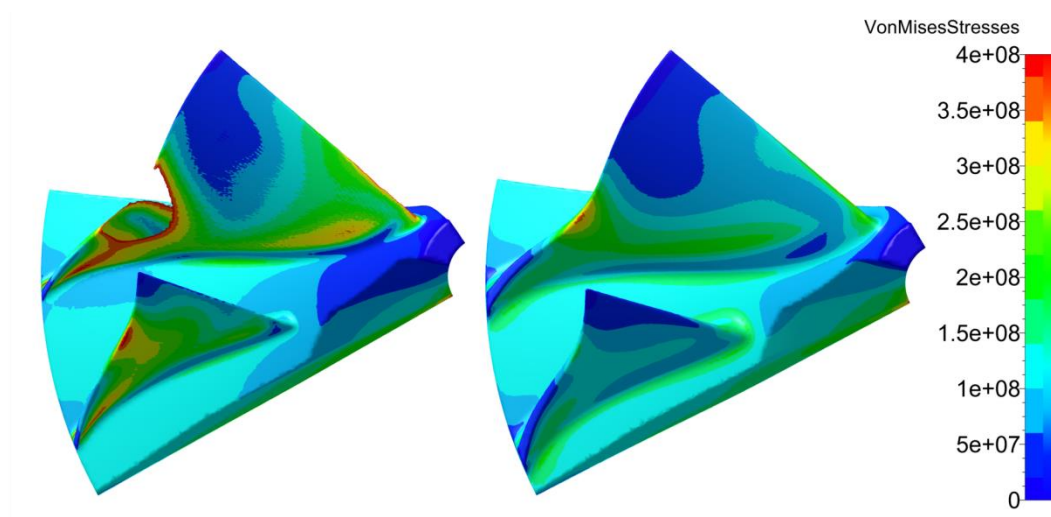


Figure 33: VM stresses of the aero-optimized design (left) and the mechanically optimized design with  $r_{fil} = 1.85$  mm

The effect of the shroud camber was investigated next, since its influence on the stresses could not yet be separated from the effects of the change in thickness distribution. Original values from the aero-optimized design were used first, with the results showing a lower mass flow rate as well as worse performance (aerodynamically and structurally) compared to the mechanically optimized design. Since this change resulted in lower mass flow, the camber values were subsequently decreased, resulting in higher mass flow and better performance. As a result of the manual shroud camber changes, the blade tip and root stresses were reduced from 370 MPa to 300 MPa and 340 MPa respectively. Efficiency and pressure ratio were higher than for the aero-optimized design. The aerodynamic optimization did not achieve this performance since any changes in camber would have had a negative effect on  $m_{HEP}$ .

Table 16 summarizes the important design criteria values for the different designs obtained. No significant differences in efficiency were observed among these designs. Maximum VM stresses are given in MPa.

Table 16: Summary of design steps and effects on performance

	$\sigma_{VM,max}$ [bore]	$\sigma_{VM,max}$ [root]	$\sigma_{VM,max}$ [tip]	$\Pi_{T-T}$ (58)	$m_{HEP}$ (kg/s)
Aero-optimized	362	>500	>500	4.62	0.851
Mech.-optimized	377	420	431	4.7	0.823
$r_{fil} = 1.85$ mm	377	370	370	4.7	0.823
Decreased 2 shroud camber values	377	340	300	4.88	0.835

## 8.6. Conclusion

A solid model of the aero-optimized design was successfully generated in FINE<sup>TM</sup>Design3D. Only centrifugal loads were considered while commencing the linear static FEAs. A hand calculation based on the torque obtained from the CFD results indicated a bore diameter of 10 mm when using a safety factor of 2. The initial database of varying backface parameters was able to reduce the impeller disk stresses by 15%. The blade stress optimization using only FEA lead to new blade thickness distributions at hub and shroud as well as a different fillet radius and shroud camber curve. Blade tip maximum stresses were reduced from above 500 MPa to 300 MPa, while the blade root stresses were reduced to a maximum of 340 MPa. As a result,  $\sigma_{VM,max}$  was located at the bore with a value of 377 MPa. These values were obtained without a decrease in aerodynamic performance but with a small sacrifice in highest efficiency mass flow  $m_{HEP}$  and choking mass flow  $m_{choke}$ . Attention could now be turned to improving the HEP and choking mass flow rates and reducing  $\sigma_{VM,max}$  through an aero-mechanical optimization.

## 9. COUPLED AERO-MECHANICAL OPTIMIZATION

The resources were available to complete a coupled optimization in FINE<sup>TM</sup>/Design3D v. 9-1.3, where each optimization step comprises a CFD simulation and FEA of a different rotor geometry. Performance results of both simulations were included in the objective function as constraints.

The primary objective of this optimization was to recover the CP mass flow rate  $m_{choke}$ . Judging from previous calculations, there was a chance that the highest efficiency point would also gain in mass flow if  $m_{choke}$  increases. Obtaining a larger  $m_{HEP}$  was found to have a bigger effect on thrust compared to an increase in pressure ratio of the same percentage of the respective design value. This was concluded by analysing different operating points using the ECA code GasTurb12.

As a secondary objective, the maximum VM stress,  $\sigma_{VM,max}$ , was to be reduced. The objectives were to be reached while conserving aerodynamic performance. It was established in the previous chapter that changes in blade camber of the aero-optimized design affect the blade root stresses, amongst others. Thus another objective was to ensure that any changes in camber did not lead to high VM stresses at the blade root.

The free parameters were:

- Section 2 (shroud) camber parameters H2 and H3
- Impeller backface control points 3, 4, 5 and 6

S2\_CAMBER\_H2 and S2\_CAMBER\_H3 were relaxed due to the previously observed influence on blade tip and root stresses, aerodynamic performance and the choke limit.

### 9.1. Database Generation

The following steps were followed during the database generation:

- Generate the geometries
- Generate the CFD meshes and confirm mesh quality
- Run the CFD simulation on the CP
- Run the FEA

To be consistent and to prevent previously experienced problems, the same numerical model settings were used as in the aerodynamic optimization. The mechanical optimization showed that relaxing the inducer radius  $r_{1s}$  has a negative effect on mass flow and thus the parameter was not relaxed.

## 9.2. Optimization Settings and Objective Function Definition

The numerical modelling settings from the database generation were carried over to the coupled optimization. Given that the choke limit was of primary importance regarding the CFD in this optimization, only the CP was chosen as an operating point evaluated in the optimization. The performance of the CP and the HEP were found to be closely related; the pressure ratio and efficiency differing by a constant value. This was deduced from results of four different designs where only the two shroud camber values H2 and H3 were varied. A comparison between the difference in  $m_{choke}$  and  $m_{HEP}$  of the four different designs was also made. These values did not exhibit the same degree of similarity. The highest difference was 0.017 kg/s, which was rounded down to 0.015 for definition of the minimum choking mass flow constraint. For the objective function the following constraints were defined:

- Choke point

A choking mass flow of  $m_{choke} = 0.865$  kg/s was expected to be achievable by only varying the shroud camber values. This was based on previous computations with different shroud camber values. CP pressure ratio and efficiency incurred penalties if their values were below four and one respectively. Based on previous calculations the CP performance directly relates to the highest efficiency point performance.

- Maximum VM Stress

The maximum VM stress constraint was set to a very optimistic minimum of  $\sigma_{VM,max} = 250$  MPa in an attempt to stretch the optimizer.

In Table 17 the final objective function constraints are given.

Table 17: Imposed quantity values for the coupled optimization objective function

	$\eta_{T-T}$ (58)	$\Pi_{T-T}$ (58)	$m_{choke}$ (kg/s)	$\sigma_{VM,max}$ (MPa)
Imposed values	1 EQUAL	4 MIN	0.865 MIN	250 MIN

In the coupled optimization the mass flow rate criterion was of primary importance, because it related to the aim of the optimization. Maximum VM stresses and pressure ratio were of higher importance than efficiency, because the database results showed that much more potential existed for an increase in pressure ratio and decrease in  $\sigma_{VM,max}$  than for an increase in efficiency.

The reference penalty value was taken to be the largest penalty for  $\sigma_{VM,max}$  that was assigned to the database designs according to the objective function while the default weight factor and exponent were used. The highest penalty for  $m_{choke}$  was set to be double that. The other maximum penalties were set to be half the

reference penalty value. This led to the best sample in the database being the one which had the following characteristics: largest  $m_{choke}$  with low  $\sigma_{VM,max}$ , high pressure ratio and high efficiency.

Of the 20 database designs and 50 designs in the optimization only 4 grids (6%) had a minimum skewness below  $18^\circ$  and 5 grids (7%) had a maximum angular skewness above  $40^\circ$ .

### 9.3. Results

After some optimization attempts, the parameter ranges were adapted to provide the optimizer with enough freedom in the direction of optimization. It was important to limit the impeller disk tip thickness to a minimum of 0.5 mm as suggested by Mr David Krige of Cape Aerospace Technologies.

The optimization was not able to increase  $m_{choke}$  of the best database design. However, the optimizer was able to increase the pressure ratio meaningfully from 3.79 to 3.97 (at CP) until the changes started affecting  $m_{choke}$  negatively. No substantial increase in efficiency was obtained. These results meant  $m_{choke}$  had to be increased using parameters other than H2 and H3 at the shroud. Looking at the circumferentially averaged relative Mach number plot of the aero-mechanically optimized design, the choke location can be seen as marked in Figure 34.

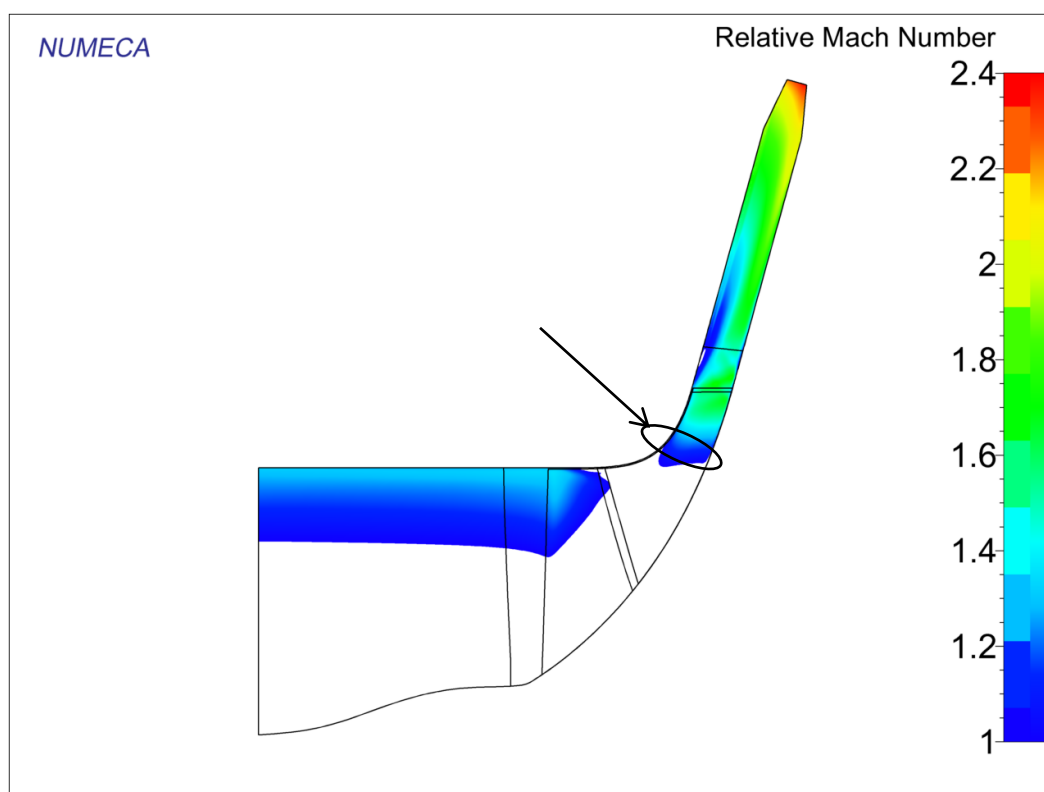


Figure 34: Relative Mach number distribution in the meridional plane at choke

To enable a larger mass flow passing through the marked location, the flow area had to be increased. Knowing that some room existed for the main blade root stress to be increased to the level of the bore stress, the following options were considered:

- Increase the inducer radius,  $r_{1s}$  (shift shroud up)
- Increase the impeller tip hub-to-shroud height,  $b_2$  (shift shroud left)

As a result of a 0.5 mm increase in  $r_{1s}$  (1.16%),  $m_{HEP}$  was shifted to  $m_{design}$ . This was achieved with the disadvantage of having a smaller pressure gradient of the impeller performance curve towards surge.  $\sigma_{VM,max}$  experienced no change. Through an increase in  $b_2$  by 0.5 mm (7.7%),  $m_{HEP}$  stayed equal to  $m_{design}$  but the choke margin improved from 2.3% to 5%. This was achieved with a small penalty in efficiency.

To evaluate the influence of the 1.85 mm fillet radius on the choke limit, a CFD analysis was completed with the fillets included. The results showed a 1.2% decrease in  $m_{choke}$ . This meant the aero-mechanically optimized design with increased  $r_{1s}$  and  $b_2$  features a choke margin of 3.8% if the fillets are considered. As for the influence of the fillets on the remainder of the performance curve, van der Merwe (2012) noted a maximum difference in CFD and experimental results in pressure ratio and in the unchoked region of 2.5%. He attributed this to omitting the fillet in the CFD.

In Figure 35 the aerodynamic performance of the CFturbo and aero-optimized designs are compared with the aero-mechanically optimized design with manual changes to  $r_{1s}$  and  $b_2$ . This design is the final design. No further changes have been made to this design in this study. A compressor map of the final design can be found in Appendix N.

Due to  $\sigma_{VM,max}$  being located at the bore with blade root stresses lying well below the bore stress before the optimization was started, and  $\sigma_{VM,max}$  not shifting to the blades during the optimization process, the backface could be optimized. The resulting backface contour together with the VM stress plot is shown in Figure 36.  $\sigma_{VM,max}$  has been reduced from 377 MPa to 342 MPa as a result of the optimized backface contour and the lower blade root stress is due to the optimized camber. This reflects a safety factor of 1.5 based on the material's yield strength. The best database value of  $\sigma_{VM,max}$  was 346.7 MPa.

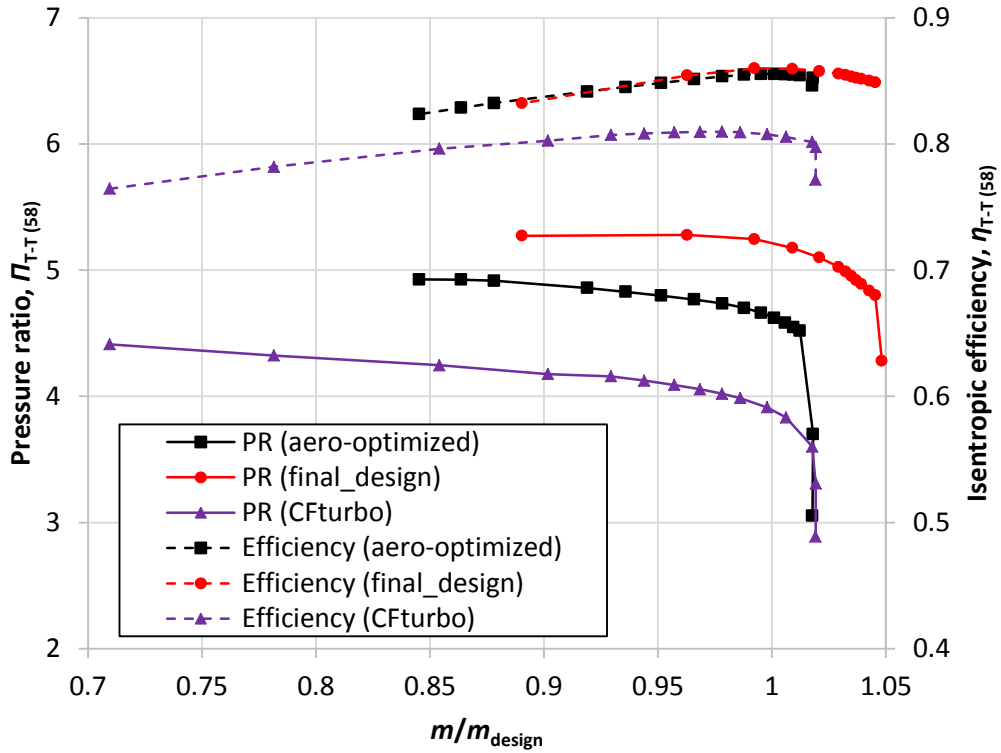


Figure 35: Final design vs. CFturbo and aero-optimized designs at 95 krpm

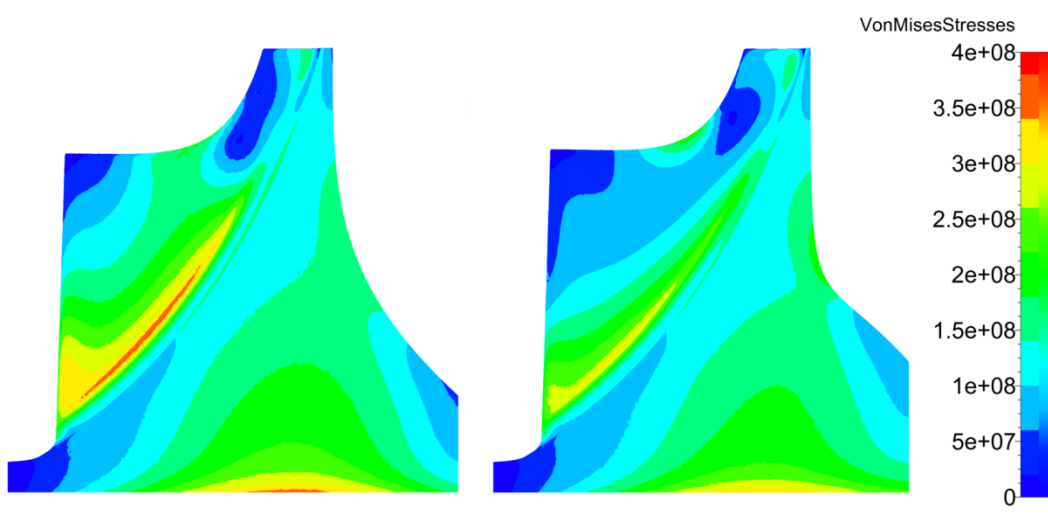


Figure 36: The mechanically optimized design with  $r_{fil} = 1.85$  mm (left) compared to the design resulting from the shroud camber and backface optimization

Table 18 summarizes the important design parameter values of the different optimized designs and the results of the manual changes on the aero-mechanically optimized design. The increase in  $b_2$  reflects the final step and the performance of the final design. The pressure ratio increased steadily, while no efficiency penalty

was incurred. Stresses can be seen to have improved meaningfully and have not been affected by the manual changes in the aero-mechanically optimized design, which are responsible for the improvement in mass flows.

Table 18: Summary of important design parameters

	$\sigma_{VM,max}$ (MPa)	$\Pi_{T-T}$ (58)	$\eta_{T-T}$ (58)	$m_{HEP}$ (kg/s)	$m_{choke}$ (kg/s)
Aero-optimized	>500	4.622	85.5%	0.851	0.865
Mech.-optimized (manually changed)	377	4.88	86.2%	0.835	0.852
Aero-mech. opt.	342	5.20	86.6%	0.830	0.856
$r_{1s}$ increase	342	5.165	86.8%	0.85	0.869
$b_2$ increase (final design)	342	5.25	86.0%	0.844	0.891

In order to obtain an impression of the changes in camber and thickness from the aero-optimized design to the resultant design of the coupled optimization, the blade profiles in the B2B-view ( $dm/r-\theta$  plane) are shown in Figure 37. The change in shroud camber angle as well as blade thickness is evident. The camber metallic angle distributions of the initial, aero-optimized and final design are compared in Appendix M.

To understand how the geometric changes improved the aerodynamic performance of the CFturbo design, the relative Mach number distributions in the B2B plane were analysed and compared. If the flow in a compressor is transonic, meaning Mach numbers exceed unity, shock structures may form. Shocks typically occur in compressors with pressure ratios larger than 3.5 (Tamaki, 2012). Shocks have a negative effect on performance due to the irreversibilities associated with shocks and the potential boundary layer separation induced by shocks. Relative Mach number distributions were thus analysed at design conditions at the HEP of the CFturbo and final designs at 10, 50 and 90% of the blade span.

At 10% span the results showed no shocks, but a very low Mach number region at the pressure side of the main blade of both designs. This region is somewhat smaller in the optimized design (Appendix K). At 50% span the CFturbo design experiences a shock at the suction side of the main blade close to the LE. This shock structure is not present in the optimized design as can be seen in Appendix K.

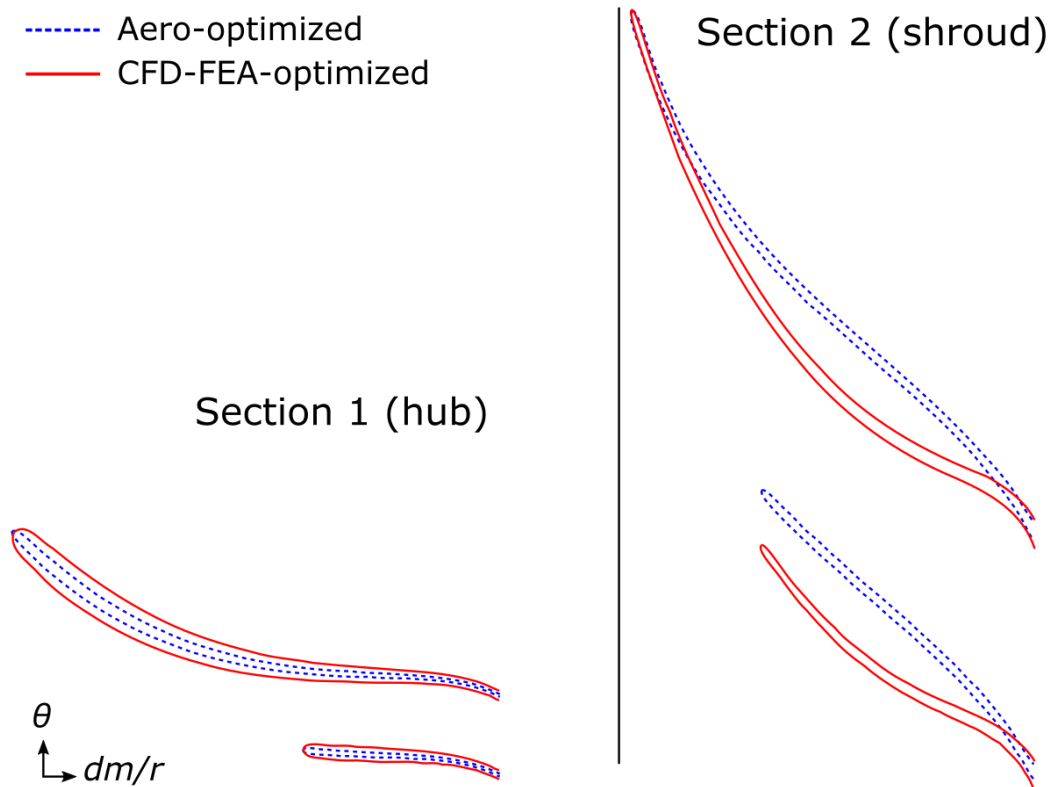


Figure 37: Blade profiles of the aero-optimized design and the aero-mechanically optimized design

Shocks are prone to appear near the shroud as shown by van der Merwe (2012). That is also the case with the CFturbo and optimised designs when analysing the B2B views at 90% span, as seen in Figure 38.

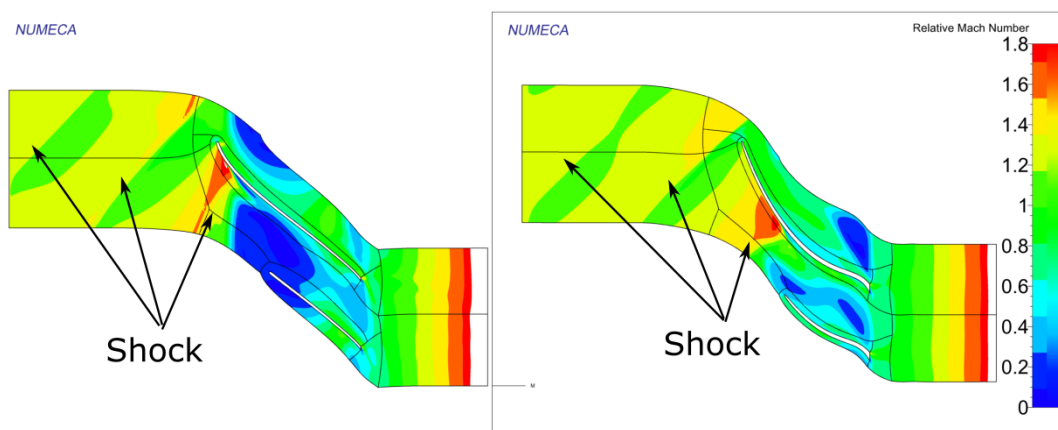


Figure 38: Relative Mach number contours of the CFturbo design (left) and the final optimized design at 90% span and design conditions

Both designs show normal shocks occurring upstream of the main blade LE. Once the air reaches the main blade LE, it accelerates to a relative Mach number of 1.8

at the suction surface before another shock occurs. In the CFturbo design, this shock causes the boundary layer to separate from the main blade suction surface, which might be the reason for the large region of very low relative Mach number downstream of the shock. In this region the flow is reversed and does not stream towards the splitter. The final design also experiences a shock at the main blade suction surface, although this shock occurs further downstream of the main blade LE and the low relative Mach number region downstream of the shock is significantly smaller, contributing to the better performance. The flow separation on the main blade suction surface is not present anymore.

The meridional view was inspected for the presence of any significant recirculation which contributes to a decrease in performance. Comparing the meridional velocity of the CFturbo and the final optimized design (Appendix K), a small recirculation zone near the LE at the shroud is evident in the CFturbo design, but completely diminished in the final design. Meridional velocities close to the TE of the CFturbo design have been reduced and show a smoother transition to higher velocities. A large recirculation zone is present in both designs downstream of the impeller due to flow separation at the shroud. This has a negative effect on stage performance and must be addressed in the future.

#### **9.4. Errors and Uncertainty**

When numerically modelling fluid flow, many possible reasons for discrepancies between the predicted results and the actual flow behaviour exist. These reasons are split into two categories: error and uncertainty. Errors in a CFD model are defined by “any deficiency that is not caused by lack of knowledge” (Versteeg and Malalasekera, 2007). Major errors are:

- numerical errors due to rounding, iterative methods and discretization
- coding errors that occurred during development of the software
- user error due to incorrect use of the software

Significant numerical errors were prevented by ensuring a reduction in the global residual by at least three orders of magnitude and by proving grid independence. Coding errors are unlikely, since the commercial software implemented has been used and validated before many times. User error was prevented by proving the author’s proficiency in the use of the software via simulation of a reference compressor stage (Chapter 4).

Uncertainty is associated with the deficiencies in a CFD model due to lack of knowledge. These include:

- input uncertainty: domain geometry, BCs and fluid properties
- physical model uncertainty: semi-empirical sub-models and simplifying assumptions

The domain geometry could be optimized for CFD modelling by placing the inlet and outlet boundaries relatively far away from the areas of interest. Pressure and temperature at the inlet were specified and an axial velocity direction could be assumed as the compressor impeller is the first component of the MGT. Using the perfect gas air model to define fluid properties reduces computational time and was deemed appropriate for compressors by MacIsaac and Langton (2011:288). Its validity for the pressure and temperature ratios achieved in this thesis was proven by computing the performance curve of the final design using the real gas model and observing a difference in performance values of less than 1%.

Turbulence models are a main contributor to physical model uncertainty. Choosing an appropriate turbulence model is essential to reducing physical model uncertainty. The Spalart-Allmaras (SA) one-equation model is often used in turbomachinery applications (van der Merwe, 2012) (Xuanyu *et al.*, 2015) (Tamaki, 2012). More information on turbulence modelling and the SA model is given in Appendix A. The validity of the SA model was confirmed by computing the performance curve of the final design using the commonly implemented  $k-\omega$  SST (shear stress transport) two-equation turbulence model. The SST-model results reveal efficiency values almost 3% higher than predicted by the SA model and a significantly larger surge margin of 40%. This leads to the conclusion that the SA model results are conservative. This will be confirmed by experimental results in the future.

## 9.5. Conclusion

A coupled aero-mechanical optimization was successfully completed using FINE<sup>TM</sup>/Design3D. The starting design was taken as the best design from the mechanical optimization. A choke mass flow rate of  $m_{choke} = 0.891$  kg/s was achieved while  $\sigma_{VM,max}$  was reduced from 377 MPa in the mechanical optimization to 343 MPa (-9%). The highest efficiency mass flow rate was shifted from  $m_{HEP} = 0.83$  kg/s to  $m_{HEP} = 0.844$  kg/s with a choke margin of 5% disregarding the effects of the fillet. The final choke margin was increased to 3.8% based on a CFD calculation including fillets. Compared to the aero-optimized design, the pressure ratio was increased by 11% and highest efficiency by 1.3%. These values were achieved through changes in camber, shroud radius  $r_{1s}$  and hub-to-shroud height at the impeller tip  $b_2$ . A surge margin of 12% was calculated for the final design. Relative Mach number distributions in the B2B plane showed diminished areas of low relative Mach number and less flow separation in the final design compared to the CFturbo design. Now that the aerodynamic and mechanical performances of the impeller have been optimised, a study on the vibrational characteristics of the design could be completed.

## 10. ROTOR DYNAMIC ANALYSIS

In this chapter the dynamics of the compressor rotor are analysed, which entails the determination of its natural frequencies and their potential excitations associated with the shaft rotational speed. FE-methods were employed to compute the natural frequencies and mode shapes of the rotor. The procedure and results of the rotor dynamic analysis are presented in this chapter.

### 10.1. Linear Static FEA Validation

A linear static FEA was conducted in MSC's SimXpert in preparation for the subsequent modal analysis. Given that a model for a linear static analysis had to be created for the modal analysis discussed in the next chapter, it was convenient to contrast and confirm the OOFELIE results.

#### 10.1.1. SimXpert FE Model and Simulation Procedure

The following procedure was undergone to complete one linear static analysis of the compressor rotor.

- CAD export and import: The scaled solid sector geometry was exported from AutoBlade<sup>TM</sup> as a Parasolid \*.xmt\_txt file and imported in MSC SimXpert. Care had to be taken that the correct units were selected. The periodic section as well as the full impeller model was exported.
- Mesh: Quadratic tetrahedral elements were generated by SimXpert's automatic solid mesher. Quadratic behaviour of displacements and stresses in between nodes was assumed such as implemented by van der Merwe (2012) and Verstraete *et al.* (2010).
- Material and co-ordinate system: Ergal was assigned to the solid property NASTRAN card as an isotropic, homogeneous material. A cylindrical co-ordinate system was created with its origin at (0, 0, 0) to which the nodal displacements were assigned.
- Cyclic symmetry: Multi-point constraints would accurately model the cyclic symmetry condition by equalling the stress states on the periodic surfaces, but for simplicity an investigation was done using only zero-displacement constraints in the tangential ( $\theta$ ) direction on the periodic surfaces as also done by van der Merwe (2012). Some problems with this modelling technique were identified to be the fact that the blades are curved and some of the periodic surfaces were not exactly orthogonal to the  $\theta$ -direction. Validity of the BC could be proven by modelling the full impeller. With the tangential constraint implemented no radial constraint was necessary.

- Axial constraint: The OOFELIE results suggest a large part of the flat impeller backface surface was axially constrained. Thus the whole flat surface was axially constrained in SimXpert. Zheng *et al.* (2012) use the same axial constraint for the linear static analysis.
- Loading: A centrifugal force was assigned to all nodes with the center of rotation at the origin and the  $z$ -axis being the axis of rotation.
- Solving: The model is written to a Nastran analysis file, which is sent to the solver.
- Post-processing: Result averaging across surfaces was switched off. This meant the values at the integration points were shown for the specified integration area, and not averaged for a smoother visual.

### 10.1.2. Results

A mesh independence study was conducted. The results of the study are shown in Table 19. It can be seen that from Mesh 2 to Mesh 3, a cell number increase of 63% resulted in a change in  $\sigma_{VM,max}$  of only 0.3% and no noticeable change in displacement.

Table 19: SimXpert linear static FEA mesh independence study results

Mesh	# of elements	# of nodes	$\sigma_{VM,max}$ (MPa) [location]	Max. displ. mag. (mm) [location]
1	58k	93k	361.5 [blade root]	0.367 [LE tip]
2	110k	174k	345.5 [bore]	0.365 [LE tip]
3	180k	281k	344.4 [bore]	0.366 [LE tip]

Table 20 lists the locations and values of the maximum VM stresses as well as the largest displacement magnitudes predicted by the different FEA packages.

Table 20: Linear static simulation result comparison

	# of elements	# of nodes	$\sigma_{VM,max}$ (MPa) [location]	Max. displ. mag. (mm) [location]
OOFELIE	400k	284k	344.2 [bore]	0.277 [TE tip]
SimXpert	110k	174k	345.5 [bore]	0.365 [LE tip]
ANSYS	92k	254k	340.1 [bore]	0.366 [LE tip]
ANSYS (full)	320k	527k	340.4 [bore]	0.365 [LE tip]

The stresses of the SimXpert and OOFELIE models do not only compare very well in values, but also in the distribution as can be seen in Figure 39. However, the displacement magnitude predicted by the SimXpert model is 30% higher than predicted by OOFELIE. Another inconsistency in terms of displacements in the OOFELIE model is that the displacement magnitude decreases with increasing mesh density as opposed to what is observed with the SimXpert model. Additionally, the location of maximum displacement is predicted to be at the trailing edge. Due to the better solidity at the trailing edge, this result does not seem realistic.

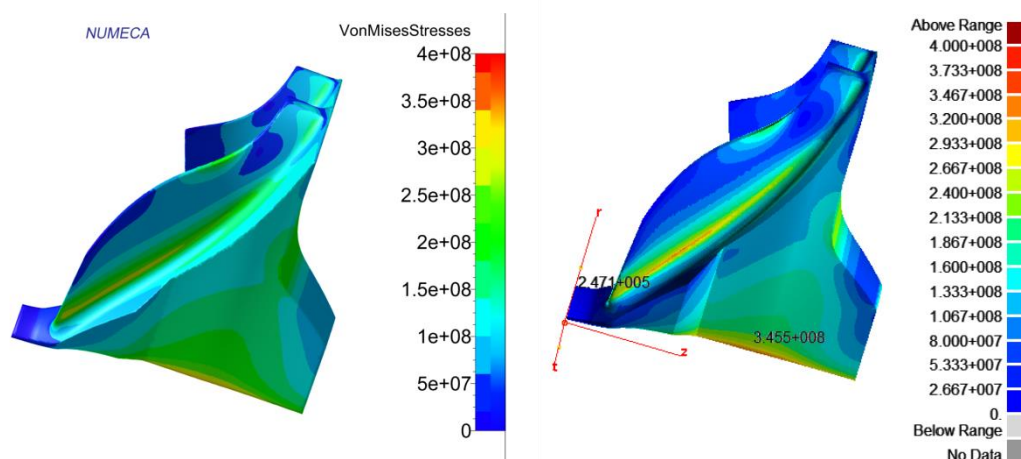


Figure 39: Comparison of OOFELIE (left) and SimXpert equivalent stress results

The periodic CAD model as well as the full impeller model were imported into ANSYS Mechanical. This served the following two purposes:

- Validate the cyclic symmetry BC implemented in SimXpert
- Confirm the displacement magnitude as obtained from the SimXpert model

The bore surface nodes were constrained in the  $\theta$ -direction and the full back plate planar surface in the  $z$ -direction. The SimXpert displacement values and distribution were confirmed by both ANSYS models, as shown in Table 20 which increases the reliability of the SimXpert results. These were thus used in determining whether the displacements are acceptable.

The tip gap is 0.2 mm wide and therefore the displacement normal to the blade tips must be below 0.2 mm to avoid the blades making contact with the casing. A safe 0.12 mm peak radial displacement located at the TE was calculated. The maximum displacement in the negative axial direction is 0.24 mm, but is located at the tip of the LE and is therefore acceptable.

Possible reasons for the discrepancy in displacement magnitude from OOFELIE could include the use of linear elements (especially tets) instead of quadratic

elements (over which the user has no control) or a discrepancy in the way the displacement magnitude is derived. Although time constraints prevented the investigation, a possible approach to finding the cause would be to analyse simpler shapes in OOFELIE in small steps, starting with a solid disk followed by a disk with straight vanes and so on.

## 10.2. Modal Analysis

Using the model described in Chapter 10 as a foundation, an undamped modal analysis was conducted. The objective was to obtain possible natural frequencies of the impeller and draw up a Campbell diagram (see Appendix A) to assess and, if necessary, change the vibration characteristics of the impeller. As discussed in Chapter 2, the stiffness of the impeller blades changes due to the centrifugal forces. This results in a shift in modal frequency at high rotational speeds.

### 10.2.1. FE Model

The important changes made to the linear static SimXpert model were:

- the change in analysis type from linear static to modal analysis with preload
- the axially constrained surface area

A rotational preload had to be added to the *load cases* due to centrifugal effects. The load case had to be selected as a preload in the *LoadCaseControl* under the *DefaultLoadCase* of the SOL103 (modal analysis). Important rotational speeds for the preload are the design speed, 10% overspeed to consider overshoot, 10% below design speed (potential testing speed), and idling speed at around 50 krpm.

The impeller back plate was assumed to be located at a shaft shoulder of 2 mm radius larger than the impeller bore. Axial displacements were therefore constrained for all nodes at a radius up to 7 mm.

### 10.2.2. Results

Different modal frequencies correspond to different mode shapes. In the case of the impeller, the shapes may be split into three groups:

- main blade flapping mode
- splitter blade flapping mode
- combined mode (main blade, splitter blade and disk)

Examples from each group are shown in Figure 40.

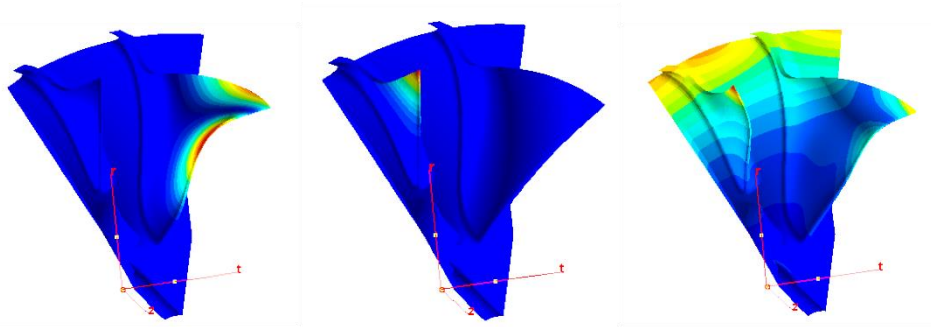


Figure 40: Different mode shape groups: main blade (left), splitter blade (middle) and combined

The resulting modal frequencies are shown in Table 21. Results from a periodic SimXpert and a periodic ANSYS model are given. In both models the whole flat backside surface of the impeller was axially constrained. This represents modelling condition 1. Condition 2 represents the smaller axially constrained surface with a radius of 7 mm. Each fill colour corresponds to a different mode shape. The natural frequencies are marginally higher than the measured values obtained by Kammerer (2009) of an aluminium radial compressor with  $r_{2s} = 200$  mm, whose first four modes are in the range of 1,400 to 5,000 Hz.

Table 21: Pre-stressed modal analysis results at 95 krpm

		Mode #					
Model		1	2	3	4	5	6
Frequency (Hz)	SimXpert 2	4,114	8,160	8,981	9,822	11,259	15,917
	SimXpert 1	4,117	8,977	9,820	11,258	14,277	15,917
	ANSYS 1	3,970	5,595	9,008	9,800	11,307	14,405

The effect of the change in axial constraint is the change in modal frequency of a combined mode from 14,277 Hz (condition 1) to 8,160 Hz (condition 2). Also, the effect of the cyclic symmetry BC is evident, as the ANSYS results show an additional combined mode at 5,600 Hz which the SimXpert model did not pick up due to its tangential constraint on the periodic surfaces.

Potential resonant conditions can be found by investigating the Campbell diagram in Figure 41. Modelling condition 2 was implemented to obtain the modal frequencies. Dashed lines represent engine order (EO) lines and the vertical line shows the design rotational speed. Triangles represent main blade flapping mode frequencies, squares represent splitter flapping modes and circles a combined blade-disk mode. The diamond signifies the ANSYS combined mode not obtained in SimXpert.

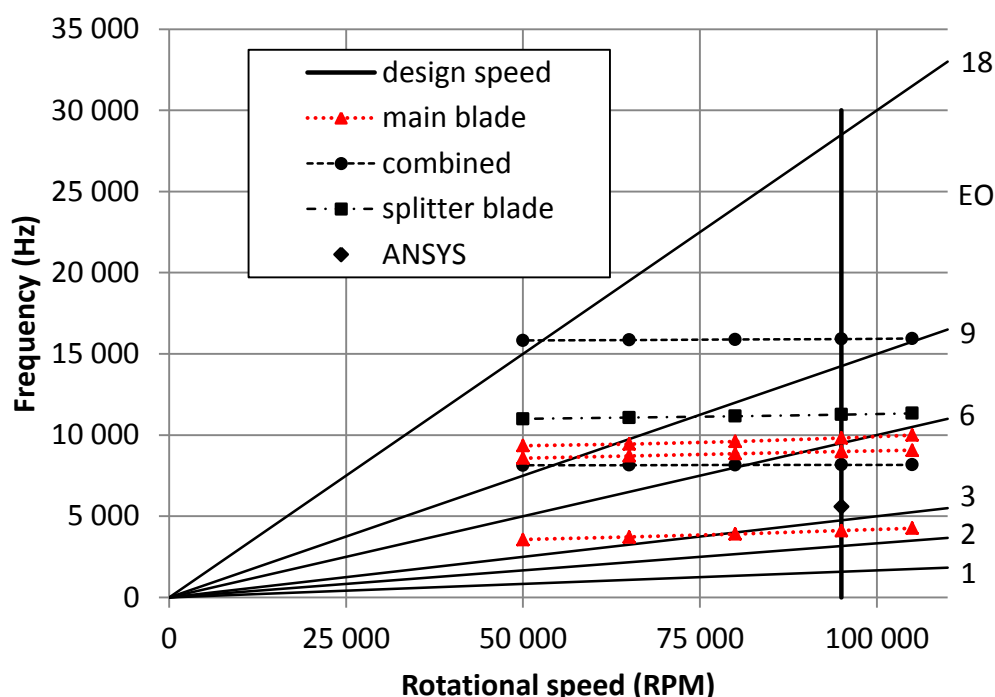


Figure 41: Compressor rotor Campbell diagram (SimXpert 2)

When analysing the Campbell diagram, it was decided to ignore self-excited stimuli as they do not need any perturbation of fixed amplitude to evoke them (Cumpsty, 1989). Only flow-field related forced vibration stimuli were considered. Unbalance and other mechanical forced vibration stimuli are more likely to be occurring at EO 1 and 2, which don't coincide with the natural frequencies. Other stimuli must, however, not be dismissed altogether. The identified potential regions of resonance are summarized in Table 22, not all listed critical speeds have the same weight, though.

The incidence of the low natural frequencies with the very low EOs are considered serious, as explained by Cumpsty (1989). Regarding the higher EOs, any critical number of struts or stator vanes near the inducer or impeller outlet as indicated in Table 22 should not be present once the MGT has been constructed. Considering the above, it can be said that the MGT should not have any 3, 6 or 9 struts or stator vanes located near the inducer. Additionally, there should be no 6, 9 or 18 stator vanes in close proximity to the impeller tip.

Speeds of 75 to 90 krpm should not be used for prolonged testing or idling speeds due to the possible excitation of the 1<sup>st</sup> main blade flapping mode at EO 3. The other main blade flapping mode critical speeds should not be serious if no 6 or 9 struts or stator vanes are located close to the inducer. The same can be said about the combined modes.

Table 22: Possible resonant conditions obtained from the Campbell diagram

Mode	Excited by	Critical speed (krpm) [EO]
1 <sup>st</sup> MB flap	3 struts/stator vanes near inducer, inlet distortion	~75-90 [3]
1 <sup>st</sup> combined	6 stator vanes near impeller outlet	~75-90 [6]
2 <sup>nd</sup> MB flap	9 & 6 struts/stator vanes near inducer	~55-65 [9], ~85-95 [6]
3 <sup>rd</sup> MB flap	9 & 6 struts/stator vanes near inducer	~60-70 [9], ~95-105 [6]
1 <sup>st</sup> SB flap	9 struts/stator vanes near inducer or impeller outlet	~70-80 [9]
2 <sup>nd</sup> combined	18 & 9 stator vanes near impeller outlet	~50[18], 105 [9]

Changes in blade design would not be helpful, in the sense that even though higher frequency modes would be shifted, the first main blade flapping mode would be moved to coincide with low EOs at design speed.

In summary, the compressor impeller features many potential resonant conditions, of which most could be prevented by considering the structural surroundings of the compressor in the MGT layout. Speeds between 70 and 90 krpm should be avoided given that a low EO coincides with the 1<sup>st</sup> main blade flapping mode. No problems are expected when running at the design speed of 95 krpm.

## 11. CONCLUSION AND RECOMMENDATIONS

Due to the increased interest in the application of MGTs for the propulsion of UAVs, a design of a mixed-flow compressor for an MGT was proposed. The design procedure and modelling results were presented in this report. Relevant theory and the function of a mixed-flow impeller was explained. An overview of the design process which was followed in this thesis was given. Literature concerning the history of mixed-flow compressors as well as the 1-dimensional and 3-dimensional analysis and development of mixed-flow compressors was detailed.

A reference compressor stage was analysed using CFD, proving the author's proficiency in the use of the software. An initial compressor impeller design was obtained using CFturbo. The initial design was optimized aerodynamically using CFD. Through the aerodynamic optimization process a gain in pressure ratio of 15% at design conditions was acquired and the efficiency was increased by 4.6% compared to the initial CFturbo design. Following the aero-optimization, a mechanical optimization was completed using FEA. The mechanical optimization process achieved a reduction in the peak VM stress from far above 500 MPa (material yield strength) in the aero-optimized design to below 400 MPa. A subsequent aero-mechanical optimization helped increase the pressure ratio of the aero-optimized design by 11% without sacrificing efficiency. The global peak VM stress was furthermore reduced to below 350 MPa (safety factor of 1.5) while the choke margin was increased by 3% as a result of manual changes to the shroud contour. The surge margin suffered a decrease from 30% in the initial design to 12% in the final design, which, according to literature, is still an acceptable surge margin. Errors and uncertainties in the CFD model were discussed. Possible resonant conditions were identified on the Campbell diagram of the rotor and relevant recommendations regarding the surrounding structure of the compressor were made.

The final mixed-flow compressor impeller design achieves a total-to-total pressure ratio of 5.2 at design conditions. This leaves a large margin for the diffuser to reach the specified stage pressure ratio of 3.83. An isentropic total-to-total efficiency of 86% was obtained for the impeller. These quantities were evaluated at a constant radius 2.5 mm downstream of the impeller tip. The maximum VM stress equals 344 MPa, which is 30% below the yield limit of the chosen material. The impeller features a surge margin of 12% as well as a choke margin of 3%, which includes the effects of the fillets. Thus the performance specifications have been met without neglecting the off-design characteristics. A summary of the impeller specifications and achieved values is given in Table 23.

Potential resonant conditions close to design speed have been identified, which should not be neglected. Critical resonant conditions exist between 75 and 90 krpm. No problems are expected when running at the design speed of 95 krpm.

Any structural members causing 3, 6 or 9 excitations per revolution should not exist near the inducer. Stator vanes near the impeller tip should be prevented to cause 6, 9 or 18 excitations per revolution. This is the result of the modal analysis that was conducted.

Table 23: Specified and obtained impeller performance quantities

Quantity	Specified	Final design
$m_{HEP}$ (kg/s)	0.85	0.844
$\Pi_{imp(T-T)}$	>4.15	5.25
$\eta_{imp(T-T)}$	>85%	86%
$\sigma_{VM,max}$ (MPa)	<300 (or <380)	344

The numerical analyses and optimization processes presented in this thesis required considerable computational time. The CPU time was, however, significantly reduced by making use of computer clusters and parallel processing. A summary of the processor management and CPU time of the major computations is given in Appendix L. A 3-dimensional render of the initial and final designs are shown in Appendix O for comparison.

### 11.1. Recommendations

Regarding the aerodynamic optimization, it was learnt that it is advisable to complete an optimization initially with small parameter bounds. This leads to a greater chance of obtaining good quality meshes as well as a smaller chance of  $m_{choke}$  being lower than  $m_{DP}$ . It is much more efficient to reduce the chance of crashed or badly converged designs before optimization, because the database requires significant computational time. If the optimizer reaches any bounds, these may be increased (but should not be reduced). Should it then be necessary to create a better mesh template, it can be done.

It might also be advisable to run only the CP calculations first to check whether designs are generated where  $m_{choke}$  is smaller than  $m_{DP}$ . The CP computations have a greater chance of being stable and have a higher guarantee of convergence if the parameter value ranges are high.

Consistency in the aero-optimization should have been guaranteed by an earlier prognosis of the robustness of the CFD grid and running all database and optimization samples using the same grid template. This did not, however, prevent the optimizer from improving the initial design.

Looking back critically, the number of free parameters on the hub and shroud in the parametric model could have been reduced by assigning four instead of five Bézier points to the impeller endwalls. Also, one parameter on the impeller shroud

curve was “free” in the parametric model, but was in fact fixed by the *slope continuity* constraint.

## 11.2. Future Work

The following areas have potential for future investigation:

- It would be interesting to observe the effect of a change in meridional exit angle  $\alpha_{C2}$  on the performance of the impeller. An optimization with  $\alpha_{C2}$  relaxed could be achieved by firstly enforcing a trailing edge trace orthogonal to the flow direction in the meridional plane. This could be done by relating the hub control point co-ordinates to the shroud contour co-ordinates using  $\alpha_{C2}$ . The vaneless diffuser passage parameters would have to be related to the trailing edge parameters. The Bezier control point adjacent to the trailing edge control point should have *slope continuity* enforced, such that it will automatically adjust to conserve the outlet angle.

This change will have an effect on the grid using the current grid template. The template should, however, be able to accommodate small changes in  $\alpha_{C2}$  without a major sacrifice in grid quality.

- The manufacturing and experimental testing of the impeller is an important step necessary to validate the numerical results presented in this thesis and should be completed in the future. Testing of the impeller could be completed in a blow-down facility as done by van der Merwe (2012) or on an MGT test rig along with all other engine components assembled.
- The diffuser is a critical component still to be designed. A single-row vaned cross-over diffuser is currently under consideration to be matched to the impeller at SU. This kind of diffuser would be ideal in terms of geometric constraints, as it would complete the tasks of directing the flow in the axial direction and recovering of the pressure in a single row. A big task for the diffuser would be to eliminate, if possible, the separation occurring at the shroud near the impeller outlet. Curving the shroud contour towards the axial direction as soon as possible is thought help reduce the separation by pushing the fluid back against the wall. The fact that the air is decelerated in that region does not assist in keeping the boundary layer attached. Therefore it might be beneficial to accelerate the fluid to prevent separation before diffusing. If this is not possible, minor changes to the impeller design could be made in order to shift the separation point or reduce the recirculation region.

## REFERENCES

- Aungier, R.H. 2000. *Centrifugal Compressors: A Strategy for Aerodynamic Design and Analysis*. ASME press, New York.
- Basson, J.G.T. 2014. Design Methodology of an Axial-flow Turbine for a Micro Jet Engine. Master Thesis. Stellenbosch University. Stellenbosch.
- Benini, E. and Giacometti, S. 2007. Design, Manufacturing and Operation of a Small Turbojet-engine for Research Purposes. *Applied Energy* 84: 1102–1116.
- Budynas, R.G. and Nisbett, J.K. 2011. *Shigley's Mechanical Engineering Design*. 9<sup>th</sup> ed. McGraw-Hill, New York.
- Boyce, M.P. 2002. *Gas Turbine Engineering Handbook*. Gulf Professional Publishing. Houston, Texas.
- Cevic, M. and Uzol, O. 2011. Design Optimization of a Mixed-flow Compressor Impeller for a Small Turbojet Engine. *Aircraft Engineering and Aerospace Technology: An International Journal*. 83(3): 127–137
- Cloud, C.H. 2009. Design Audits of Turbomachinery: Rotor Dynamics. *Proceedings of the 21<sup>st</sup> Ethylene Producers' conference*. Tampa, Florida, USA.
- CFturbo. 2014. CFturbo 9.2. User's Manual.
- Cumpsty, N.A. 1989. *Compressor Aerodynamics*. Longman Group UK Limited. Singapore.
- Chen, J., Huang, G., Xia, C., Zhu, J. 2011. Flow Analysis and Improvement of a micro Transonic Compressor Impeller. *47th AIAA/ASME/SAE/ASEE Joint Propulsion Conference & Exhibit*. AIAA 2011-5750.
- Demeulenaere, A. and Hirsch, C. 2004. Application of Multipoint Optimisation to the Design of Turbomachinery Blades. ASME Paper GT-2004-53110.
- Demeulenaere, A., Jonnacorsi, J.C., Gutzwiller, D., Hu, L., and Sun, H. 2015. Multi-disciplinary multi-point optimization of a turbocharger compressor wheel. *Proceedings of ASME Turbo Expo 2015*. Montreal, Canada.
- De Wet, A.L. 2011. Performance Investigation of a Turbocharger Compressor. Master Thesis. Stellenbosch University. Stellenbosch.
- De Villiers, L.C.B. 2014. Design of a Centrifugal Compressor for Application in Micro Gas Turbines. Master Thesis. Stellenbosch University. Stellenbosch.

- Dixon, S.L. 1998. *Fluid Mechanics and Thermodynamics of Turbomachinery*. 5<sup>th</sup> ed. Elsevier Butterworth-Heinemann. Oxford.
- Dubbel, H. 1997. *DUBBEL: Taschenbuch für den Maschinenbau*. 19th ed. W. Beitz, & K. H. Küttner (Editors). Springer.
- Eisenlohr, G. and Benfer, F.W. 1994. Aerodynamic Design and Investigation of a Mixed-Flow Compressor Stage. AGARD Conference Proceedings 537: Technology Requirements for Small Gas Turbines.
- Fischer, A., Korfanty, M., Müller, R., Strobel, J. 2014. Auslegung, Entwurf, Nachrechnung und Optimierung einer Hochdruck-Turboverdichterstufe. *ANSYS Conference and 32<sup>nd</sup> CADFEM User's Meeting*. Nuremberg, Germany. [Online]. Available: [http://en.cfturbo.com/fileadmin/content/down/papers/ACUM\\_2014\\_CFturbo.pdf](http://en.cfturbo.com/fileadmin/content/down/papers/ACUM_2014_CFturbo.pdf) [2015, November 2]
- Goldberg, D.E. 1989. *Genetic Algorithm*. Addison Wesley Publishing.
- Harris, M., Jones, A. and Alexander, E. 2003. Miniature Turbojet Development at Hamilton Sundstrand: The TJ-50, TJ-120 and TJ-30 Turbojets. Paper presented at the *2nd AIAA Unmanned Unlimited Systems, Technologies and Operations–Aerospace Conference*, Sand Diego, CA, USA.
- Hildebrandt, T., Thiel, P. and Lehmann, I. 2009. Entwicklung eines leistungsgesteigerten Radialverdichters für Ab-gasturbolader: Von der CFD basierten Optimierung mit FINE™/Turbo bis zum serienreifen Prototyp im Hause KBB. *Proceedings of the 14<sup>th</sup> Aufladetechnische Konferenz*, Dresden.
- Hildebrandt, T., Gressera, L. and Sievert, M. 2011. Kennfeldverbreiterung eines Radialverdichters für Ab-gasturbolader durch multi-disziplinäre CFD-FEM-Optimierung mit FINE™/Turbo. *Aufladetechnische Konferenz Dresden*.
- Hill, G.H. and Peterson, C.R. 1992. *Mechanics and Thermodynamics of Propulsion*. Addison-Wesley. USA.
- Japikse, D. 1996. *Centrifugal Compressor Design and Performance*. Concepts ETI. USA.
- Japikse, D., and Baines, N.C. 1997. *Introduction to Turbomachinery*. Oxford University Press.
- Kammerer, A. 2009. Experimental Research into Resonant Vibration of Centrifugal Compressor Blades. PhD dissertation. Zürich: Swiss Federal Institute of Technology (ETH Zürich). Diss. ETH No. 18587.

- Kano, F., Fukao, Y. and Shirakami, T. 1984. Development of High Specific Speed Mixed Flow Compressors. *Proceedings of the 13<sup>th</sup> Turbomachinery Symposium*. Texas A&M University. Texas, USA. pp. 139-147.
- Krige, D.S. 2013. Performance Evaluation of a Micro Gas Turbine Centrifugal Compressor Diffuser. Master Thesis. Stellenbosch University. Stellenbosch.
- King, J.A. and Glodeck, E. 1942. Performance Characteristics of Mixed-Flow Impeller and Vaned Diffuser with several Modifications. NACA Wartime Report E-197.
- LEDGER University Research Program. [Online]. Available: <http://ledger.wikispaces.com/> [2014, July 18]
- MacIsaac, B. and Langton, R. 2011. *Gas Turbine Propulsion Systems*. 1st ed. Wiley-Blackwell.
- Mönig, R., Broichhausen, K. and Gallus, H. 1987. Application of Highly Loaded Single-Stage Mixed-Flow Compressors in Small Jet-Engines. *AGARD Conference Proceedings No. 42*.
- Mönig, R., Elmendorf, W. and Gallus, H. 1993. Design and Rotor Performance of a 5:1 Mixed-Flow Supersonic Compressor. *Journal of Turbomachinery*, 115(3): 565-72.
- Montgomery, D. 2001. *Design and Analysis of Experiments*. 5<sup>th</sup> ed. John Wiley & Sons Inc. New York, USA.
- MSC Software. 2015. [Online]. Available: <http://www.mssoftware.com/product/simxpert> [2015, October 31]
- Müller, R.P. and Kreuzfeld, G. 2011. CFturbo – Modern turbomachinery design software. *Compressor Tech Magazine*.
- Musgrave, D. and Plehn, N. 1987. Mixed-Flow Compressor Stage Design and Test Results with a Pressure Ratio of 3: 1. *Journal of Turbomachinery*, 109(4): 513-9.
- National Research Council. 2000. Uninhabited Air Vehicles: Enabling Science for Military Systems. National Academy Press, Washington, D.C. pp. 59–61.
- Niculescu, M.L., Silivestru, V., Vizitiu, G., Danaila, S. and Berbente, C. 2007. Theoretical and Numerical Investigation of Centrifugal and Mixed Compressor Impellers. Paper presented at the *8th International Symposium on Experimental and Computational Aerothermodynamics of Internal Flows*.
- NUMECA International. 2014a. AutoGrid5<sup>TM</sup> User Manual.

- NUMECA International. 2014b. FINE™/Turbo 9.1 User Manual.
- NUMECA International. 2014c. CFView 9.1 User Manual.
- NUMECA International. 2014d. AutoBlade™ User Manual.
- NUMECA International. 2014e. FINE™/Design3D 9.1 User Manual.
- Patankar, S.V. 1980. *Numerical Heat Transfer and Fluid Flow*. USA: McGraw-Hill.
- Pichlmeier, D. 2010. [Online]. Available: [http://www.dapitech.de/EN/turbine\\_cad\\_en.html](http://www.dapitech.de/EN/turbine_cad_en.html) [2015, November 1]
- Pierret, S., Demeulenaere, A., Gouverneur, B. and Hirsch, C. 2000. Designing Turbomachinery Blades with the Function Approximation Concept and the Navier-Stokes Equations. *8th AIAA/NASA/USAF/ISSMO Symposium on MDO*, Long Beach, CA.
- Ramamurthy, S. and Srharsha, A.M. 2009. Theoretical Evaluation of Flow through a Mixed Flow Compressor Stage. *19<sup>th</sup> International Symposium on Air Breathing Engines*.
- Ramesh Rajakumar, D., Ramamurthy, S. and Govardhan, M. 2013a. CFD Analysis of Flow through Mixed Flow Compressor Under various Operating Conditions. *International Journal of Scientific & Engineering Research*, 4(2).
- Ramesh Rajakumar, D., Ramamurthy, S. and Govardhan, M. 2013b. Study on the Performance Deterioration of Mixed Flow Impeller due to Change in Tip Clearance. *Journal of Thermal Sciences*, 22(6): 532-538.
- Schenk, O. and Gärtner, K. 2004. Solving unsymmetric sparse systems of linear equations with PARDISO. *Journal of Future Generation Computer Systems*. 20(3): 475-487.
- Tamaki, H. 2012. Effect of Recirculation Device with Counter Swirl Vane on Performance of High Pressure Ratio Centrifugal Compressor. *ASME Journal of Turbomachinery*. 134(5). 051036.
- Tamaki, H., Unno, M., Kawakubo, T. and Hirata, Y., 2009. Aerodynamic Design to Increase Pressure Ratio of Centrifugal Compressors for Turbochargers. *Proceedings of the ASME Turbo Expo 2009: Power for Land, Sea and Air*. ASME, Orlando, Florida, pp. 1171–1184.
- Valakos, I.M., Ntipteni, I.S. and Nikolos, I.K. 2007. Structural Optimization of a Centrifugal Impeller using Differential Evolution Algorithm in CATIA Environment. *Operational Research*. 7(2): 185 – 212.

- Van der Merwe, B.B. 2012. Design of a Centrifugal Compressor Impeller for Micro Gas Turbine Application. Master Thesis. Stellenbosch University.
- Velde, O., Kreuzfeld, G., Lehmann, I., and Buchmann, K. 2012. Schneller Designprozess für Radialverdichterlaufräder durch Beurteilung der Meridianströmung und der Schaufeldruckverteilung während des Entwurfs. *Aufladetechnische Konferenz Dresden*.
- Versteeg, H.K. and Malalasekera, W. 2007. *An Introduction to Computational Fluid Dynamics: The Finite Volume Method*, 2<sup>nd</sup> ed. Harlow: Pearson Education Limited.
- Verstraete, T, Alsaahli, Z and Van den Braembussche, R.A. 2010. Multidisciplinary optimization of a radial compressor for micro gas turbine application. *ASME Journal of Turbomachinery*. 132(3) 0.31004.
- Vick, M.J., Heyes, A. and Pullen, K. 2010. Design Overview of a 3 Kilowatt Recuperated Cermaic Turboshaft Engine. *ASME Journal of Engineering for Gas Turbines and Power*. 132(9) 092301.
- Visser, G. 2014. Modal Analysis: What it is and is not. [Online] Available: <https://esteq.co.za/2014/11/25/modal/> [2015, November 7]
- White, F.M. 1998. *Fluid Mechanics*. 4<sup>th</sup> ed. McGraw-Hill.
- Whitfield, A. and Baines, N.C. 1990. *Design of Radial Turbomachinery*. Longman Scientific & Technical, Essex, England
- Whitfield, A. and Roberts, D. 1981. The Effect of Impeller Tip Design on the Performance of a Mixed Flow Turbocharger Compressor. Paper presented at the *ASME Gas Turbine Conference and Products Show*, Houston, Texas.
- Youssef, N. and Weir, G. 2002. Mixed Flow and Centrifugal Compressor for Gas Turbine Engine. US Patent Number 6488469 B1
- Xuanyu, C., Xiangwei, M., Xingmin, G., and Donghai, J. 2015. The Aerodynamic Design and Investigation of Loading Distribution of a Mixed Flow Compressor. *Procedia Engineering* 99 484 – 490
- Zheng, X., Jin, L., Zhang, Y., Qian, H. and Liu, F. 2012. Effects of Disk Geometry on Strength of a Centrifugal Compressor Impeller for a High Pressure Ratio Turbo Charger. *Proceedings of ASME 2012 Gas Turbine India Conference*, Mumbai, India.

## APPENDIX A: THEORY AND SOFTWARE

### A.1 Computational Fluid Dynamics (CFD)

Computational fluid dynamics is the numerical analysis of fluid behaviour under given boundary conditions. Partial differential equations (PDEs) defining the flow field are converted to algebraic relations (White, 1998). The algebraic equations are applied on a discretized space. This means there are a discrete number of “cells” inside the space of interest, which is termed the flow domain.

In CFD-terminology the word cell is used, since in CFD the finite volume (FV) discretization approach is predominantly implemented. The FV-method splits the flow field into control volumes with cell-centred nodes, over which the PDEs are integrated by assuming appropriate interpolation schemes for the behaviour of the property in-between nodes (Patankar, 1980).

#### A.1.1 Reynolds-Averaged Navier-Stokes (RANS) Equations

One of the governing physical laws of fluid flow is the conservation of momentum. For a Newtonian fluid the Navier-Stokes (NS) equations embody this law. The nature of flows encountered in practice is predominantly turbulent, which means highly three-dimensional and time-dependent. However, in steady flow, the fluctuations of a flow variable revolve around a steady average value. To simplify flow modelling, the Reynolds-averaged NS (RANS) equations were thus developed, defining a flow variable by its time average plus an average deviation. This leads to additional terms in the underlying equations called Reynolds stresses. The basic NS equations do not provide enough information to solve these additional terms; a so-called closure problem arises, leading to turbulence modelling.

#### A.1.2 Turbulence Modelling

In order to close the system of equations generated by the additional Reynolds stresses, turbulence models were developed. Commonly used turbulence models are based on the Boussinesque approximation, which relates Reynolds stresses to mean rates of deformation using the so-called eddy viscosity  $\mu_t$ . A very successful model for aerofoil applications is the Spalart-Allmaras (SA) turbulence model, with only one additional transport equation to close the system of equations: the transport equation for the “eddy viscosity parameter”, which is a parameter used to define  $\mu_t$  (Versteeg and Malalasekera, 2007). A transport equation relates the rate of change of a quantity to the convection, diffusion, production and dissipation of the quantity. It is a low- $Re$  model and is suitable for aerofoil applications due to its stall-predicting ability (Versteeg and Malalasekera, 2007).

The SA model has proven its capabilities in aerofoil applications and has been implemented in this project.

## **A.2 Finite Element Analysis (FEA)**

Much like the dynamic behaviour of fluids is simulated in CFD, the stresses and deformations of a solid body can be simulated as well. In this field, called CSM (Computational Structural Mechanics), finite element methods (FEM) are usually applied. A computational structural (mechanical) analysis using FEM is called a finite element analysis (FEA). A solid is divided into small elements of finite size which share nodes at the element boundaries. The nodal displacements (and rotations) are linked through the force-displacement relations and material behaviour. Given the boundary conditions, the unknown displacements may be obtained through iterative or direct (matrix inversion) approaches. From the displacements the stresses in the material may be derived and failure predicted using appropriate failure theories.

### **A.2.1 Linear Static Analysis**

A linear static analysis assumes deformation in the linear-elastic region of the material. The analysis looks at the deformation of a fully constrained static body resulting from a specified load.

### **A.2.2 Rotor Dynamics and Modal Analysis**

Any structure experiences an unusual degree of displacement if excited at its natural frequency. This is due to the structure absorbing all of the energy supplied by the excitation (Visser, 2014). Each natural frequency has an associated mode shape, which are properties of the structure. The natural frequencies and mode shapes of a structure are dependent on the stiffness, mass and damping of the structure. However, the un-damped modes may be used to describe the motion, because the mechanical and aerodynamic damping is typically adequately small (Cumpsty, 1989). The purpose of a modal analysis is to determine these natural frequencies and associated mode shapes.

In the case of a rotating structure (rotor) many different kinds of vibration stimuli may occur during operation and lead to resonance. If, for example, the rotational speed of the rotor aligns with a natural frequency, any rotor imbalance will cause resonance due to the resulting excitation frequency. This will result in excessive vibratory motion (Cloud, 2009). The speed coinciding with the natural frequency speed is called the critical speed. According to Boyce (2002) an excitation may be a

- forced instability dependent on outside stimuli or a
- self-excited instability independent of outside stimuli such as flutter.

Typical forced vibration stimuli are:

- Mechanical stimuli such as:
  - Unbalance
  - Asymmetric flexibility (sag in the rotor shaft)
  - Shaft misalignment
  - Bearings
- Flow field stimuli including:
  - wake or potential field of an upstream stator or strut
  - inlet distortion (Cumpsty, 1989)

Japikse and Baines (1997) cite struts in the inlet, diffuser vanes and harmonics of the rotational speed as excitation sources. Judging from a Campbell diagram, the authors show possible excitations in a radial impeller due to subsynchronous whirl of the bearings (2 per rev). Excitation was avoided by making blade thickness modifications.

The Campbell diagram gives an indication of operational areas that could encounter resonance (Boyce, 2002). Engine order (EO) lines (Equation A.1), which represent harmonics of the rotational speed, are shown as well as the natural frequencies measured or simulated. If an important EO line coincides with a natural frequency, resonance can be expected at that excitation frequency and corresponding rotational speed.

$$f = n * \frac{N}{60} \quad (\text{A.1})$$

The critical EO lines depend on the excitations that may be caused per revolution of the rotor. If the rotor has 18 blades, any integer divider of 18 may excite a natural frequency linked to the main and splitter blade, or the whole impeller disk. Hence the EO lines to be considered would be 1, 2, 3, 6, 9 and 18 excitations per revolution. These EO lines are likely to coincide with multiple natural frequencies and it would be an impossible task to prevent all intersections. Cumpsty (1989) explains that the intersection of the low order natural frequencies with the very low order EOs are more serious than the others, and thus the focus should be to preventing these occurrences. High EO excitations of rotor blades are dangerous if stator rows or struts are located near the rotor blades. Increased axial spacing between adjacent blade rows leads to faster dissipation of the excitation strength.

A dominant excitation frequency is the design rotational speed. Other important speeds are the idling speed and potential testing speeds. Once a vaned diffuser is added to the design the stator blade passing frequency would also play a critical role. Figure 42 depicts a typical Campbell diagram showing three EO lines and one natural frequency. Hatched regions are drawn close to the intersections,

emphasizing the risk of resonance being within a frequency/speed region which is to be avoided while operating the machine.

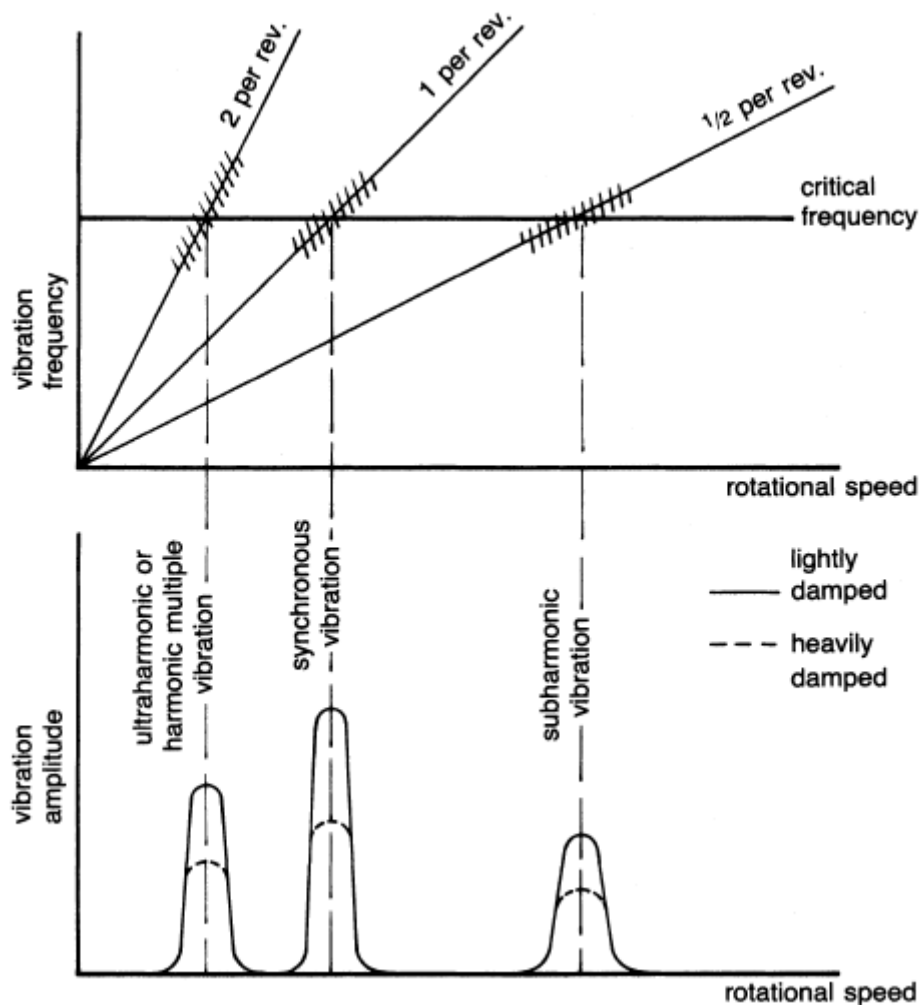


Figure 42: Campbell diagram and associated damped vibration amplitude (Boyce, 2002)

The flexural natural frequencies (flapping modes) of the rotor tend to increase with rotational speed due to the stiffening of the blade at high rotational speeds Cumpsty (1989). Thus not only do the natural frequencies and modes of the impeller have to be found, they have to be found as a function of rotational speed as shown by Basson (2014).

Another factor affecting the natural frequencies is the change in temperature. An increase in temperature causes the modulus of elasticity to decrease, which leads to a reduction in natural frequency. Thermal effects do, however, not form a part of this study. FEA or experimental methods may be used to find the natural frequencies and associated mode shapes of a structure.

### A.3 Software

This thesis has a strong focus on numerical modelling. Numerical modelling allows the designer to obtain relatively accurate performance predictions and insight into the behaviour of materials such that modifications can be made to improve the design before it is manufactured. This section refers to the major software packages that were used - for numerical modelling purposes and others - and explains their role in the design of compressors.

#### A.3.1 CFturbo

CFturbo is a commercial turbomachinery layout tool designed for radial and mixed-flow turbomachinery (CFturbo, 2014). The first design step requires the definition of the design point and the fluid properties. Thereafter the machine type and general meridional shape is defined based on the specific speed. Next the main dimensions (suction diameter, impeller diameter and outlet width) are generated based on conservation of mass, energy and momentum.

Efficiencies and empirical parameters (such as work coefficient, total flow coefficient, outlet width ratio, etc...) are predicted using the software. The prediction is based on empirical approximation functions that are dependent on specific speed or flow rate. Velocity triangles are generated next and meridional contours (Hub, shroud, LE and TE of blades) are defined. The “leading edge blade angles are calculated for shock-less inflow considering blade blockade. Trailing edge blade angles are calculated using the Euler equation and a slip model” (Mueller and Kreuzfeld, 2011). Blade thickness is also used for blade angle calculations. Initial blade thickness is determined by empirical functions (dependent on impeller diameter).

Using the Euler equation and the determined velocity triangles, the blade angles are placed on several span-wise cuts (Velde *et al.*, 2012). The blade angle distribution between LE and TE forms the blade mean lines and together the mean lines form the blade surface. Blade mean lines are formed in conformal mapped space using Bézier splines. The 3-dimensional form of the blade is generated. Until now the user always has the option to confirm the aerodynamic quality via empirical methods such as the Cordier diagram and manual geometric analysis. The performance prediction is purely empirically based and to be used with extreme caution. “The Cordier diagram is based on intensive empirical analysis of proved turbomachinery using extensive experimental data” (CFturbo, 2014).

#### A.3.2 NUMECA

NUMECA develops commercial software for the 3-dimensional simulation of fluid flow and multi-physics scenarios. In this thesis six different NUMECA packages are used. AutoGrid5<sup>TM</sup> is used to generate structured CFD meshes, FINE<sup>TM</sup>/Turbo for definition of boundary conditions and solving, CFView<sup>TM</sup> for

post-processing and visualization, AutoBlade™ for parametric modelling, FINE™/Design3D for multi-disciplinary optimization and HEXPRESS/Hybrid™ for the generation of unstructured FEA grids. The FE-kernel that was utilized in the optimization is developed by Open Engineering S.A. ([www.open-engineering.com](http://www.open-engineering.com)) and is integrated in FINE™/Design3D. More detailed information on the six software packages from NUMECA is highlighted as follows:

### AutoGrid5™

AutoGrid5™ (**A**utomated **G**rid Generator for Turbomachinery) is a software package developed to automatically generate high-quality structured grids for complex turbomachinery geometries. Structured grids are favoured in turbomachinery applications due to the higher accuracy obtained.

In AutoGrid5™ cylindrical blade surfaces are mapped from 3-dimensional Cartesian ( $x$ - $y$ - $z$ ) space to 2-dimensional blade-to-blade (B2B) space ( $dm/r$ - $\theta$  plane) in a process called conformal mapping. Four main steps make up the grid generation process:

- Geometry definition (blades, hub and shroud curves, splitters, etc...).
- Creation of the meridional flow paths. The 3-dimensional grid is constructed on the surfaces of revolution defined by the meridional traces of the flow paths.
- Building and regulation of the 2-dimensional meshes on span-wise cuts. This process includes
  - Blade & layer intersection
  - Conformal mapping
  - B2B mesh initialization
  - B2B topology optimization
- Construction of the 3-dimensional mesh by joining the 2-dimensional meshes defined on the flow paths along the span.

The surfaces of revolution created via the flow path definition are called layers. They intersect the 3-dimensional blade geometry and the resulting surfaces of intersection are projected onto the  $dm/r$ - $\theta$  plane. Through conformal mapping angles are preserved during projection, which means the mesh quality is also conserved. Each B2B grid is linked to a flow path. The curvilinear co-ordinate of a flow path is equal to the meridional co-ordinate in the  $dm/r$ - $\theta$  plane (NUMECA International, 2014a) shown in Figure 43.

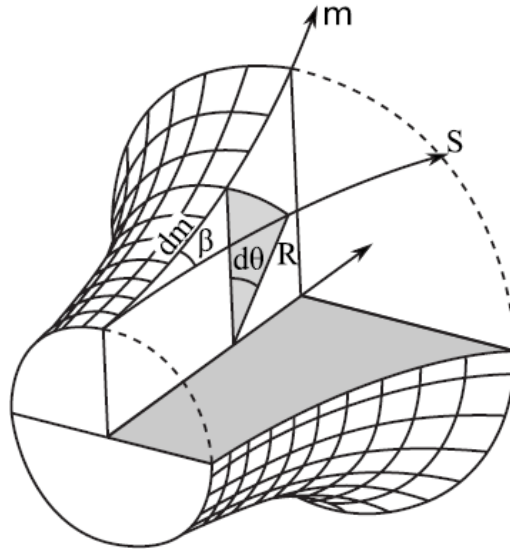


Figure 43: Construction of the  $dm/r-\theta$  plane (Verstraete *et al.*, 2010)

### FINE<sup>TM</sup>/Turbo

FINE<sup>TM</sup>(Flow **I**ntegrated **E**nvironment)/Turbo is the software package to which an AutoGrid<sup>TM</sup>5 mesh is imported. The boundary conditions are applied to the grid and the numerical method and flow solver settings are defined using FINE<sup>TM</sup>/Turbo. Subsequently the computation is run using the FINE<sup>TM</sup>/Turbo solver, EURANUS. EURANUS is a 3-dimensional multi-block solver capable of solving Euler or Navier-Stokes (laminar and turbulent) flows (NUMECA International, 2014b).

### CFView<sup>TM</sup>

CFView<sup>TM</sup> is a post-processing tool which can be used to represent relevant scalar or vector quantities obtained through a FINE<sup>TM</sup>/Turbo simulation in two and three dimensions. It is possible to display in cylindrical and Cartesian co-ordinates as well as B2B views. Circumferential averaging can be applied and surface integrals can be evaluated among others. New quantities can be defined and computed. The integrated macro capabilities are useful for automating the post-processing step. Macros can be recorded while working in CFView<sup>TM</sup> and are written in the Python programming language which makes writing, reading and handling of data simple (NUMECA International, 2014c).

### AutoBlade<sup>TM</sup>

AutoBlade<sup>TM</sup> is a parametric geometry modeller for 3-dimensional turbomachinery blades. In AutoBlade<sup>TM</sup> it is possible to model the blades and also

to fit a modelled geometry to a given target geometry by automatically varying the previously defined model parameters (NUMECA International, 2014d).

### FINE/Design3D

FINE™/Design3D integrates the AutoGrid5™, CFView™, FINE™/Turbo and AutoBlade™ package to form an environment for 3-dimensional optimization of turbomachinery. This is achieved by an optimization feature linked to the AutoBlade™ parametric model and creating a coupling between the optimization and the CFD-chain in FINE™/Turbo. FINE™/Design3D is also coupled to HEXPRESS™/Hybrid and OOFELIE, which represent the FEA-chain. It is therefore possible to run a multi-disciplinary optimization in FINE™/Design3D (NUMECA International, 2014e).

### HEXPRESS™/Hybrid and OOFELIE

HEXPRESS™/Hybrid generates unstructured hex-dominant meshes for all kinds of applications. It can mesh inner and outer geometries of any complexity in parallel.

OOFELIE (**O**bject **O**riented **F**inite **E**lements led by an **I**nteractive **E**xecutor) is a numerical modelling toolkit that includes a finite-element (FE) kernel. OOFELIE was designed for multi-disciplinary interactions as well as couplings between other professional numerical modelling tools (Open Engineering, 2015). The **parallel direct sparse linear solver** (PARDISO) (Schenk and Gärtner, 2004) for linear systems of equations is the default solver used by OOFELIE in FINE™/Design3D.

### A.3.3 MSC SimXpert and Nastran

MSC (**M**ac**N**eal-**S**chwendler Corporation) SimXpert is a commercial multi-disciplinary computer-aided engineering (CAE) tool. It supports simulation of structural (FEA), multi-body dynamic, crash and thermal problems, among others. The simulation chain from pre- to post-processing is completed in a unified environment. SimXpert prepares models to be solved by MSC Nastran. MSC Nastran (**N**ASA **s**tructural **a**nalysis) is a version of the Nastran FE solver developed by MSC (MSC Software, 2015).



## APPENDIX C: CFTURBO SETTINGS

### Global Setup

- Mass flow: 0.63 kg/s
- Total pressure ratio: 4
- Revolutions per minute: 95,000
- Gas: Air, perfect
- Casing efficiency (stator & volute): 85 %
- Inlet conditions:  $p_{01} = 0.987$  bar,  $T_{01} = 26$  degC
- Swirl number: Hub: 1, Shroud: 1

### Meridional Contour

- Changed shroud meridional exit angle to be the same as hub angle:  $74.5^\circ$

### Main Dimensions

- Setup
  - Splitter blades selected
  - Unshrouded selected
  - Tip clearance 0.2 mm
- Parameters
  - Diameter coefficient: 3.084
  - Outlet width ratio: 0.058
  - Meridional deceleration: 1
  - Total-to-total efficiency: 89.1
- Dimensions
  - Shaft allowable stress: 15 MPa, factor of safety: 1.15
  - Min shaft diameter: 16.9 mm
  - Hub diameter: 17.2 mm
  - Suction diameter: 86.4 mm
  - Impeller diameter: 111 mm
  - Outlet width: 6.44 mm
  - Cordier diagram

### Blade Properties

- Blade setup
  - Number of blades: 9/9
  - Blade shape: ruled surface 3D
  - Splitter blade linked to main blade selected
  - Blade average thickness: hub, shroud, main, splitter: 0.6 mm
  - Incidence: flow ratio shockless/design selected. hub 100%, shroud 100%

- Deviation flow Model: Wiesner slip coefficient selected
- Blade angles
  - Automatic selected
  - number of blade profiles: 5
  - Main blade incidence angle: Hub: 53.5, Shroud: 15.3
  - Main blade sweep: Hub: 38, Shroud: 38

Blade edges:

- Leading edge: design mode ellipse, axis ratio: 3
- Trailing edge: blunt

Blade Profiles:

- Main blade: design mode: linear. SS-PS coupling: symmetric. global point count: 4

## APPENDIX D: COMPRESSOR IMPELLER PERFORMANCE EVALUATION

In the mean-line approach the performance of the impeller is estimated by calculating the theoretical pressure ratio and temperature ratio between inlet of the impeller and the impeller tip (blade TE). Evaluation of the CFD results was therefore initially also at the impeller tip, in line with the meridional trailing edge position. This was the case for the MATLAB and CFturbo designs.

Studies were conducted on the influence of the position of the evaluation plane. They showed that, with the grid topology as set for the CSIR and CFturbo designs, there is a major drop in efficiency when evaluating a small distance downstream of the trailing edge, but no big variation in total pressure. This may, however, depend on the design.

To generate an evaluation plane in CFView<sup>TM</sup>, a new quantity may be defined, of which an *Isosurface* generates the evaluation plane at a specific quantity value. The radius  $r$  was defined by:

$$r = \sqrt{x^2 + y^2} \quad (\text{D.1})$$

This forms a cylindrical evaluation plane at any given radius  $r$ . A quantity evaluated on a plane of constant  $r$  is designated by a subscript which includes  $r$  in brackets, for example the total pressure ratio at  $r = 58$  mm would be  $\Pi_{T-T(58)}$ . For the designs with the TE orthogonal to the channel curves the following quantity was defined:

$$c = r + \tan(90 - \alpha_{c2}) * z \quad (\text{D.2})$$

which forms a conical evaluation plane at a given value for  $c$ . Equation D.2 was used to evaluate the design obtained from the in-house 1-dimensional code shown in Figure 12.

Cell-values of the quantity of interest were averaged on the cylindrical or conical evaluation plane by using a mass-weighted surface integral. The weighting factor was set to be the product of density and the absolute velocity vector (mass flux). As recommended by the CFView<sup>TM</sup> Manual (NUMECA International, 2014c), the absolute values of the absolute velocity components were taken to prevent the results not reflecting the max/min range of the quantity which might be caused by backflow. The weighted integral is defined by:

$$\text{weighted integral} = \frac{\int q * (\vec{w} \cdot \vec{dS})}{\int (\vec{w} \cdot \vec{dS})} \quad (\text{D.3})$$

where  $q$  is the quantity value,  $\vec{w}$  is the weight vector and  $\vec{dS}$  is the surface vector differential. The dot represents the dot-product. For a mass-averaged weighted integral  $\vec{w} = \rho \vec{V}$ . The mass-weighted integral is commonly used for total quantities in compressible flow due to influence of the mass flux on the quantity.

The mass flow rate was evaluated at the domain outlet. This value had to be treated with care, as backflow at the outlet would lead to different mass flow rates if the absolute value velocity was used to compute the mass flow as compared to the real velocity. Backflow was, however, minimized at the outlet through the use of a constriction.

## APPENDIX E: CFD AND FEA GRID DETAILS AND DEPENDENCY

### E.1 Reference Compressor Stage Grid

The impeller inlet bulb topology was selected to be a “butterfly” rounded topology with the grid points and smoothing steps as indicated in Figure 45.

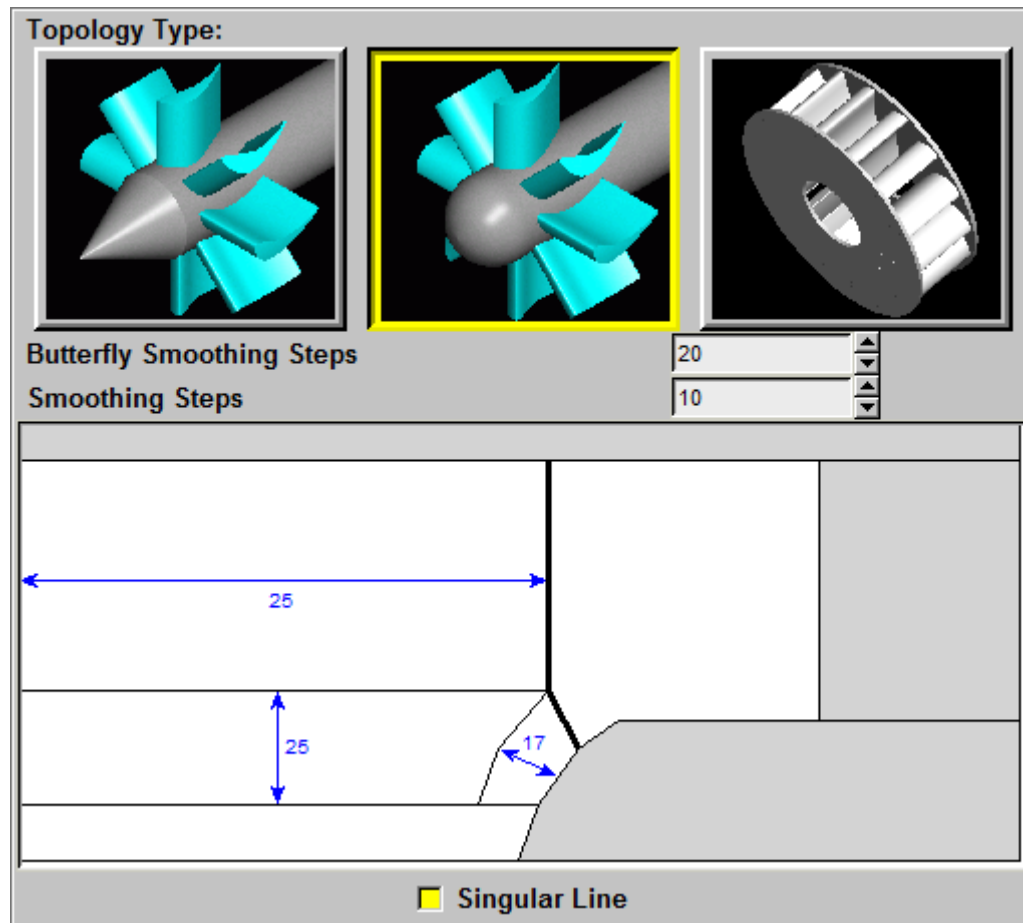


Figure 45: Inlet bulb mesh topology of the reference stage

Figure 46 shows the number of grid points of the impeller grid along the different block boundaries and also, in case of the splitter blade, the distribution between inlet and skin block. The skin block is the block closest to the blades and has been enabled for both blades. In Figure 47 the diffuser O4H topology and the grid point distribution is shown.

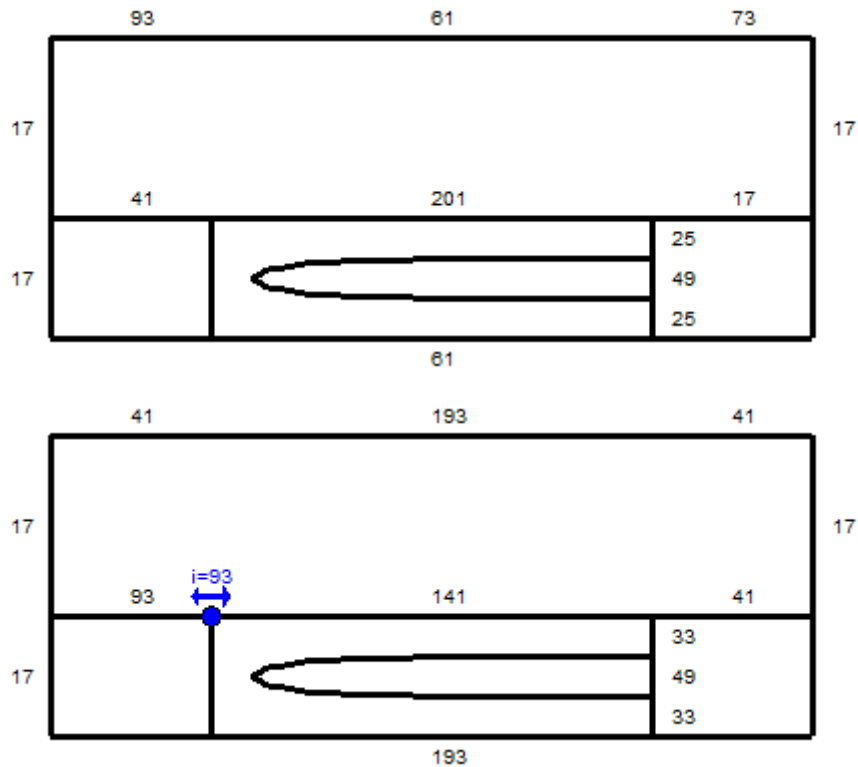


Figure 46: Main blade (top) and splitter blade grid points of reference impeller

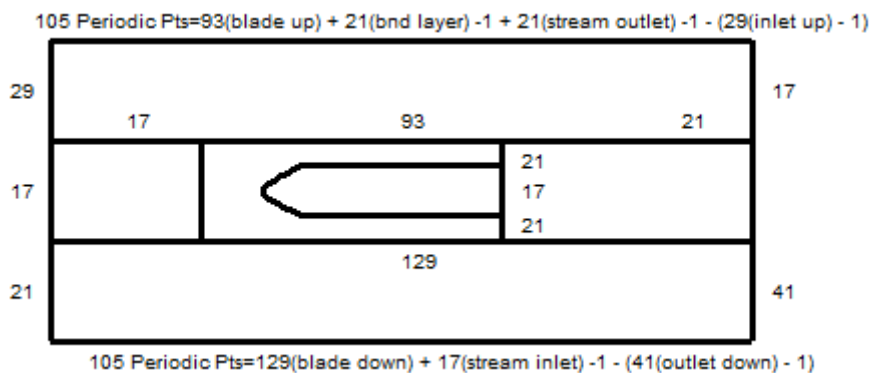


Figure 47: Grid point distribution of reference diffuser

## E.2 Grid used for the Initial CFturbo Design as well as DB01 and DB02

In Table 24 the important grid defining parameters for the grid generated for the initial CFturbo design are given. The \*.trb grid template file generated in the process was implemented for databases DB01 and DB02, which were part of the final database used for the aerodynamic optimization.

Table 24: Important grid defining dimensions of the initial design

Cell width at wall and TE ( $\mu\text{m}$ )	# of flow paths	Tip gap (mm)
5	73 (17 in tip gap)	0.2

600 B2B *optimization* steps along with 500 *gap optimization* steps produced the best grid quality while *skewness control in gaps* was set to *medium*. No fillets were implemented in the CFD. No optional H-topology for inlet and outlet was selected in the *topology* tab. *High staggered blade optimization* was enabled with both, the main and splitter blade being of *low angle* outlet type, where the main blade was of inlet type *high angle* and the splitter of inlet type *normal*.

The outlet was selected to be untwisted from a stream-wise starting point 13% downstream of the control line closest to the TE. This improved the span-wise grid quality. An improvement in span-wise grid quality was also obtained by placing a few z-constant lines uniformly spaced between inlet and LE. Prior to this change, the hub curvature created low angles in the span-wise direction. No *shroud gap interpolation* was enabled. *Span interpolation* was 7%.

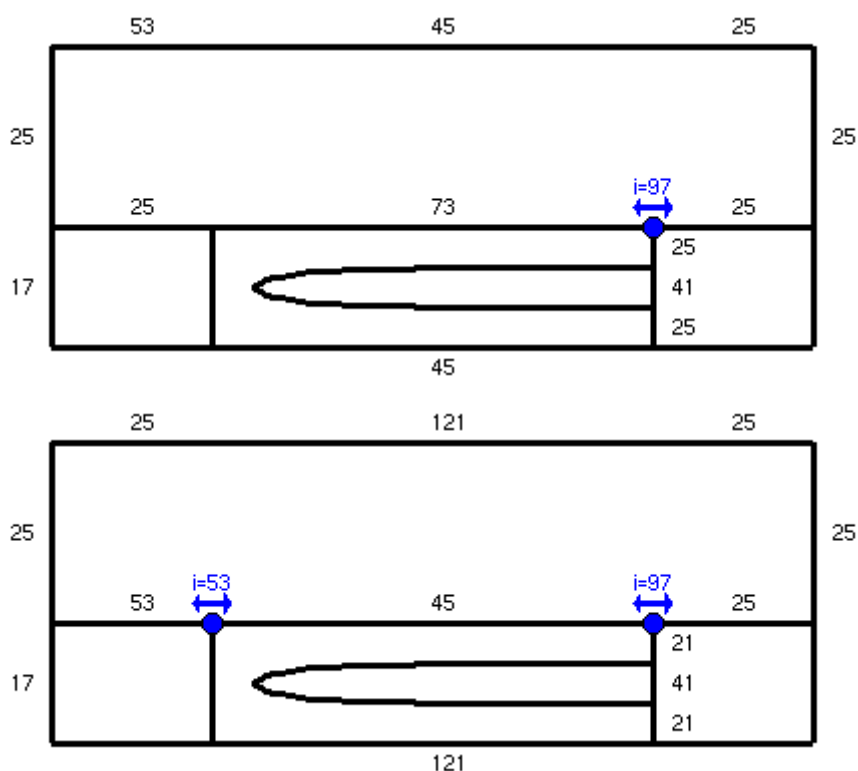


Figure 48: Main blade (top) and splitter blade grid points of initial design, database and optimization grid

A grid independence study was completed and results are shown in Figure 49. The quality of the grid on the CFturbo design is given in Table 25.

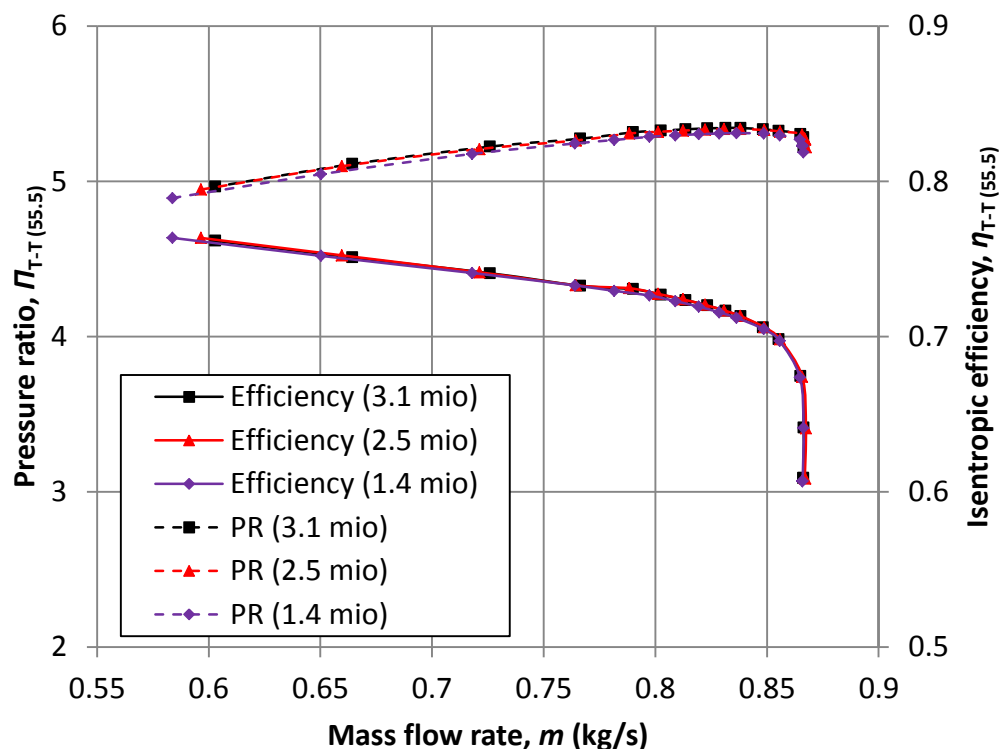


Figure 49: CFturbo (initial) impeller design grid independence study results

Table 25: Final CFturbo design mesh quality

Criterion	Critical value	Suggested range	% bad cells
Angular skewness (deg)	21.7	>20	0
Aspect ratio	410	<10 000	0
Expansion ratio	2.53	<2.5	0.002
Angular deviation (deg)	23.9	<45	0

### E.3 DB03, Aerodynamic Optimization and Coupled Optimization CFD Grid

As mentioned in the main body of the text, the major difference to the grid used for DB01 and DB02 was in the main blade outlet topology type which was set from *low angle* to *normal* and the fact that the H-topology at the outlet was enabled. A mesh independence study was also conducted for this grid, evaluating performance 2.5 mm downstream of the trailing edge. Results are shown in Figure 50.

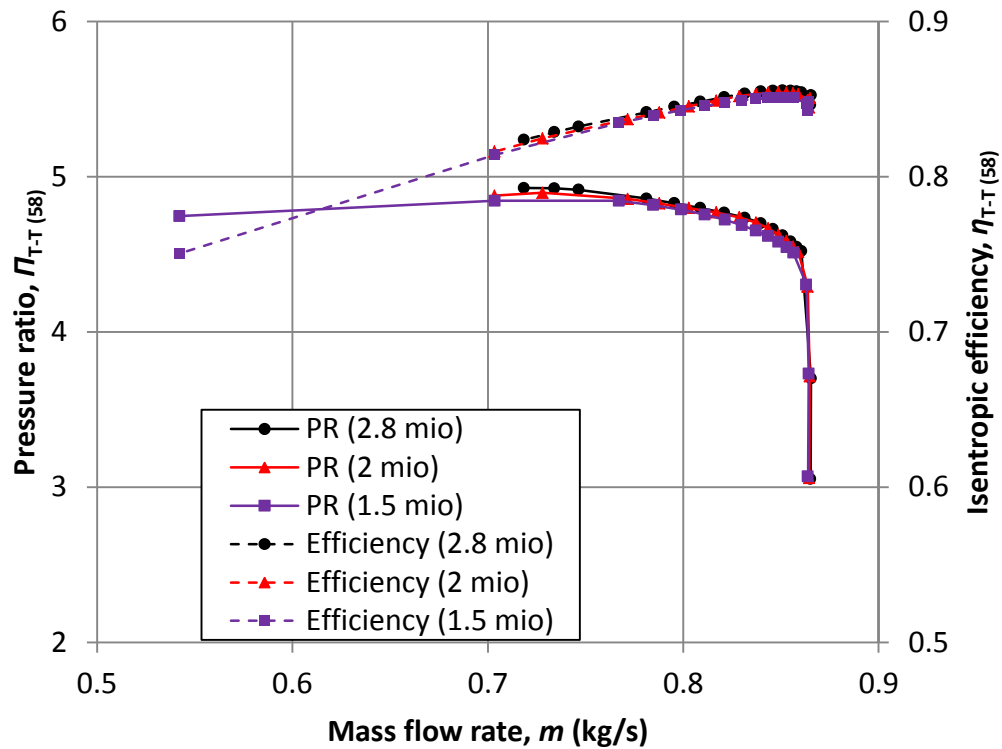


Figure 50: Grid independence study results of the grid used for DB03, OPT14 and all subsequent CFD simulations

#### E.4 HEXPRESS<sup>TM</sup>/Hybrid FEA Grid Settings

Grid generation settings that were applied in FINE<sup>TM</sup>/Design3D for the FEA are given in Table 26. A grid independence study of the HEXPRESS<sup>TM</sup>/Hybrid grid was not conducted due to computational limits. The linear static FEA stress results of the final impeller design were, however, confirmed by grid independent SimXpert results as well as ANSYS results using a periodic section and also a full impeller model.

Table 26: Automatic grid generation settings in FINE<sup>TM</sup>/Design3D

Parameter	Value
Global Element Size	2.4
Refinement Diffusion	0
Curved Face Max NB Divisions	4
Blend Refinements	3, 3
Blade PS/SS Refinements (min, max)	3, 3
Blade Blunt/Tip Refinements (min, max)	3, 3
General Refinements (min, max)	2, 2

## APPENDIX F: Y-PLUS VALUES

In Table 27 the maximum values of the  $y^+$ -values at the wall boundaries at HEP of grids for the following geometries are given:

- the reference compressor stage
- the CFturbo design chosen as base design for the optimization
- the final design, which was aero-mechanically optimized

The values correspond to the fine grids used to generate the results presented in this thesis (~3 million cells). They had to be kept below 10.

Table 27: Maximum wall- $y^+$  values for important impeller designs at HEP

Geometry of computational grid	Maximum wall- $y^+$ value
Reference compressor stage	6.3
CFturbo design	7.5
Final optimized impeller	8.4

## APPENDIX G: NUMECA AUTOBLADE DESIGN SPACE

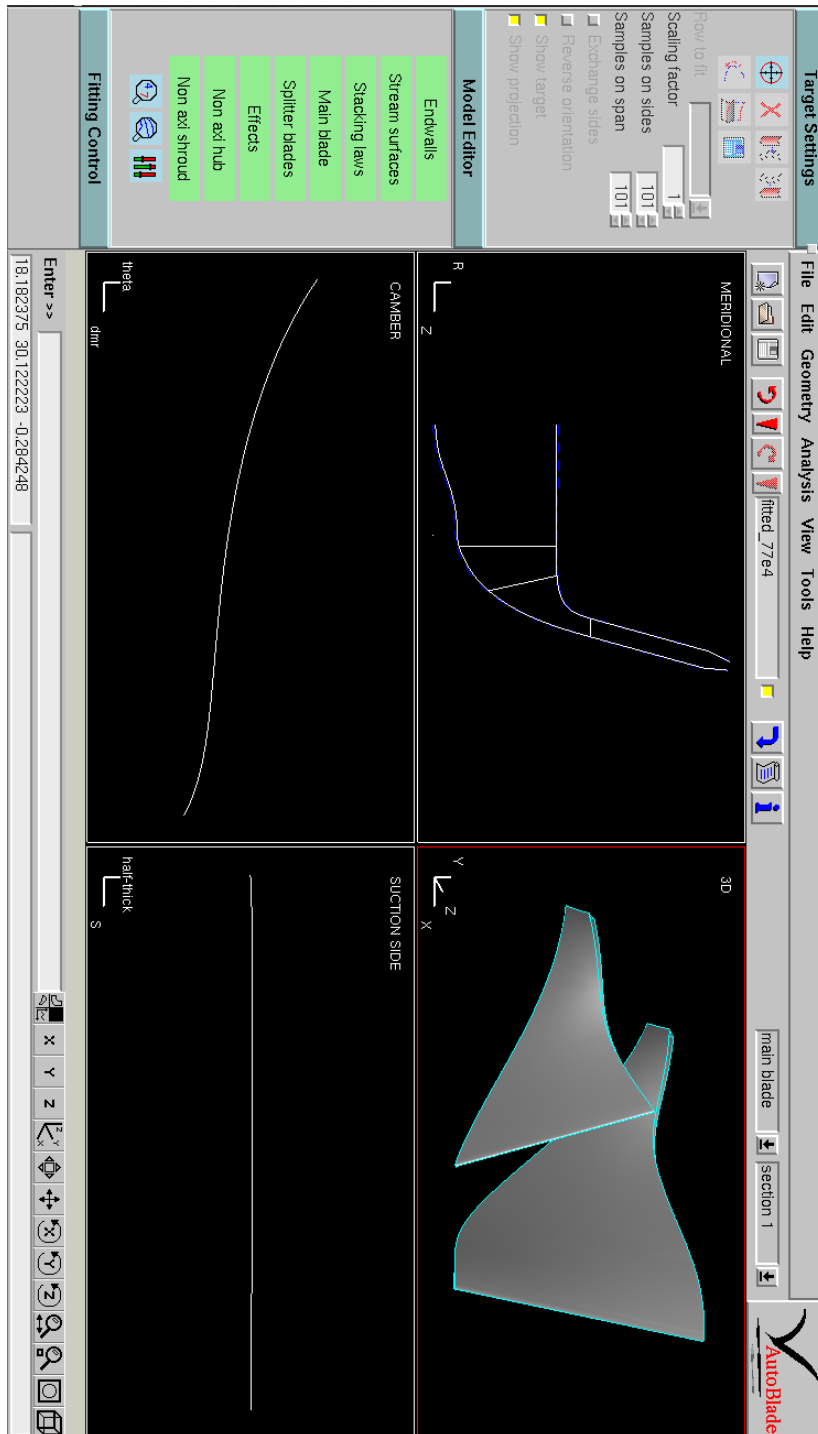


Figure 51: NUMECA AutoBlade™ design space

## APPENDIX H: DOE IMPELLER PARAMETERS

### H.1 Parametric Model Overview

Table 28 lists the different parametric groups and the associated parameters of the parametric model used in the aerodynamic optimization. Main blade and splitter blade are abbreviated MB and SB respectively.

Table 28: Parametric model overview

Parametric group	Amount of parameters	
	Sum	Free
1) Endwalls	$16 + 20 = 36$	12
2) Stream surfaces: sectional locations	2	0
3) Section 1 & 2: camber (MB)	$2 \times 5 = 10$	10
Section 1 & 2: thickness distributions (MB & SB)	$2 \times 6 = 12$	0
Section 1 & 2: SB meridional position	$2 \times 3 = 6$	2
4) Meridional location: MB LE & TE	$2 + 2 = 4$	2
Meridional length: section 1 & 2	2	0
5) Tangential location: lean	1	1
6) Number of blades	1	0
7) Rotational speed	1	0
<b>Total</b>	<b>75</b>	<b>27</b>

### H.2 Aerodynamic Optimization: Free Parameters

NAME	MINIMUM	VALUE	MAXIMUM	REFERENCE
----	-----	-----	-----	-----
HUB_Z5	4.9936	6.993583	8.9936	1
HUB_R5	10.1085	10.10853	11.1085	1
HUB_Z6	21.4255	23.4255	25.4255	1
HUB_R6	9.8652	14.8652	19.8652	1
HUB_Z7	28.0993	30.0993	32.0993	1
HUB_R7	33.4401	35.4401	37.4401	1
SHROUD_Z3	7.890094	10.89009	13.89009	1
SHROUD_R3	43.202	43.20203	46.202	1

SHROUD_Z4	20.7399	23.79349	26.7399	1
SHROUD_R4	41.2806	43.28161	46.2806	1
SHROUD_Z5	22.396	26.41798	30.396	1
SHROUD_R5	41.3544	45.43364	49.3544	1
S1_CAMBER_H1	-0.461	-0.261	-0.161	0.05
S1_CAMBER_H2	-0.653	-0.503	-0.403	0.05
S1_CAMBER_H3	-0.669	-0.569	-0.469	0.05
S1_CAMBER_H4	-0.58	-0.48	-0.38	0.05
S1_CAMBER_H5	-0.795	-0.695	-0.595	0.05
S1_SPLIT1_MLE	0.5325	0.57	0.6075	0.0375
S2_CAMBER_H1	-0.392	-0.242	-0.192	0.05
S2_CAMBER_H2	-0.361	-0.261	-0.211	0.05
S2_CAMBER_H3	-0.527	-0.477	-0.427	0.05
S2_CAMBER_H4	-0.612	-0.562	-0.512	0.05
S2_CAMBER_H5	-0.748	-0.698	-0.648	0.05
S2_SPLIT1_MLE	0.278	0.353	0.428	0.0375
Z_LE_HUB	1.551	3.551	5.551	2
Z_LE_SHROUD	1.538	3.538	5.538	2
LEAN_BETA	0	0.145455	3.145	3

### H.3 Aerodynamic Optimization: Frozen Parameters

NAME	MINIMUM	VALUE	MAXIMUM	REFERENCE
----	-----	-----	-----	-----
HUB_Z1	-39.2000	-39.2000	-39.2000	0
HUB_R1	0.8000	0.8000	0.8000	0
HUB_Z2	30.5308	30.5308	30.5308	0
HUB_R2	1.7846	1.7846	1.7846	0
HUB_Z3	6.4475	6.4475	6.4475	0
HUB_R3	8.2264	8.2264	8.2264	0
HUB_Z4	3.5752	3.5752	3.5752	0
HUB_R4	9.0499	9.0499	9.0499	0
HUB_Z8	35.6431	35.6431	35.6431	0
HUB_R8	55.4855	55.4855	55.4855	0
HUB_Z9	46.5273	46.5273	46.5273	0
HUB_R9	94.8409	94.8409	94.8409	0
HUB_Z10	47.3367	47.3367	47.3367	0
HUB_R10	103.2490	103.2490	103.2490	0
SHROUD_Z1	-39.2000	-39.2000	-39.2000	0
SHROUD_R1	43.2	43.2	43.2	0
SHROUD_Z2	3.5308	3.5308	3.5308	0

SHROUD_R2	43.2017	43.2017	43.2017	0
SHROUD_Z6	29.2084	29.2084	29.2084	0
SHROUD_R6	55.4993	55.4993	55.4993	0
SHROUD_Z7	40.5590	40.5590	40.5590	0
SHROUD_R7	96.4435	96.4435	96.4435	0
SHROUD_Z8	44.2338	44.2338	44.2338	0
SHROUD_R8	104.1095	104.1095	104.1095	0
S1_SPAN	-0.02	-0.02	-0.02	0
S2_SPAN	1.02	1.02	1.02	0
S1_LE_RADIUS	0.373007	0.373007	0.373007	0
S1_HALF_THICKNESS_P1	0.278889	0.278889	0.278889	0
S1_HALF_THICKNESS_P2	0.283236	0.283236	0.283236	0
S1_SPLIT1_MTE	0	0	0	0
S1_SPLIT1_DELTA_THETA	0.001062	0.001062	0.001062	0
S1_SPLIT1_LE_RADIUS	0.387632	0.387632	0.387632	0
S1_SPLIT1_HALF_THICKNESS_P1	0.225941	0.225941	0.225941	0
S1_SPLIT1_HALF_THICKNESS_P2	0.315471	0.315471	0.315471	0
S2_LE_RADIUS	0.366348	0.366348	0.366348	0
S2_HALF_THICKNESS_P1	0.186718	0.186718	0.186718	0
S2_HALF_THICKNESS_P2	0.343602	0.343602	0.343602	0
S2_SPLIT1_MTE	0	0	0	0
S2_SPLIT1_DELTA_THETA	0.007272	0.007272	0.007272	0
S2_SPLIT1_LE_RADIUS	0.319261	0.319261	0.319261	0
S2_SPLIT1_HALF_THICKNESS_P1	0.295906	0.295906	0.295906	0
S2_SPLIT1_HALF_THICKNESS_P2	0.302196	0.302196	0.302196	0
R_TE_HUB	55.5	55.5	55.5	0
R_TE_SHROUD	55.5	55.5	55.5	0
S1_MERID_LENGTH	2.791985	2.791985	2.791985	0.001
S2_MERID_LENGTH	0.676490	0.676490	0.676490	0.001
NB	9	9	9	0
BLADE_ROTATION	39.83848	39.83848	39.83848	0

## APPENDIX I: OBJECTIVE FUNCTIONS

The imposed value, constraint type, relevant actual value, weight factor, exponent, reference value and the resultant penalty value of the relevant quantities for the aero-optimization objective function is given in Table 29. Values for the aero-mechanical optimization objective function are given in Table 30.

Table 29: Objective function definition of the aerodynamic optimization with balanced penalty values according to the given quantity value

	Quantity	$q_{imp}$	Type	$q$	$w$	$k$	$q_{ref}$	Penalty
DP-CP	$\eta_{T-T}$ (58)	0	MIN	-0.003	200	2	0.1	0.18
SP-DP	$\Pi_{T-T}$ (58)	0	MIN	-0.01	20	2	0.1	0.2
CP	$m$	0.9	MAX	0.91	16	2	0.09	0.198
CP	$m$	0.84	MIN	0.835	55	2	0.084	0.195
SP	$m_{in}$ conv.	0.05	MAX	0.06	5	2	0.05	0.2
DP	$m_{in}$ conv.	0.02	MAX	0.03	80	2	0.2	0.2
DP	$\Pi_{T-T}$ (58)	4.2	MIN	4.1	350	2	4.2	0.198
DP	$\eta_{T-T}$ (58)	1	EQUAL	0.78	4	2	1	0.194

Coupled optimization:

Table 30: Objective function definition of the coupled optimization with penalty values according to the given quantity value

	Quantity	$q_{imp}$	Type	$q$	$w$	$k$	$q_{ref}$	Penalty
CP	$\eta_{T-T}$ (58)	1	EQUAL	0.855	12	2	1	0.252
CP	$\Pi_{T-T}$ (58)	4	MIN	3.35	20	2	4	0.528
CP	$m$	0.865	MIN	0.853	2	2	0.017	0.996
FEA	$\sigma_{VM,max}$	250e06	MAX	380e06	2	2	250e06	0.541

## APPENDIX J: SHAFT STRESS CALCULATIONS

The maximum von Mises stress of a shaft in terms of shaft stresses is given by Budynas and Nisbett (2011:370):

$$\sigma_{VM,max} = \sqrt{3 * \left( \frac{16K_{fs}(T_m)}{\pi d^3} \right)^2} \quad (J.1)$$

where  $K_{fs}$  is the fatigue stress-concentration factor for torsion and  $T_m$  is the midrange torque. Equation J.1 is a shortened version of the original equation, where the midrange and alternating bending moments have been ignored, since the available information was not sufficient to obtain these. The same applied to the alternating torque.

Rearranging Equation J.1 yields

$$d = \left( \frac{16K_{fs}(T_m)}{\pi \sqrt{\left( \frac{\sigma_{VM,max}^2}{3} \right)}} \right)^{\frac{1}{3}} \quad (J.2)$$

The midrange torque acting on the shaft was obtained from the CFD calculation of the aero-optimized design at design conditions and yielded  $T_m = 16.7$  N.m.  $K_{fs}$  was taken to be 1, assuming low notch-sensitivity. The material was selected to be mild steel as suggested by the CSIR. The cold-drawn low carbon steel designated AISI 1018 is a common mild steel with a yield strength of 370 MPa (Budynas and Nisbett, 2011). The safety factor  $n_y$  is defined as

$$n_y = \frac{\sigma_y}{\sigma_{VM,max}} \quad (J.3)$$

where  $\sigma_y$  is the yield strength. The CSIR suggested a safety factor of 2, which leads to a maximum VM stress of 185 MPa, which was rounded down to a conservative 150 MPa, given that bending stresses were ignored and low notch sensitivity was assumed. Substituting this value in Equation J.2 yields a minimum shaft diameter of 10 mm.

## APPENDIX K: MERIDIONAL VELOCITIES AND B2B RELATIVE MACH NUMBERS IN COMPARISON

In Figure 52 the circumferentially averaged meridional velocity distribution in the meridional plane of the CFturbo design and the final design are shown. A diminished high-velocity region can be seen in the final design. The recirculation zone at the shroud of the vaneless diffusing passage is evident.

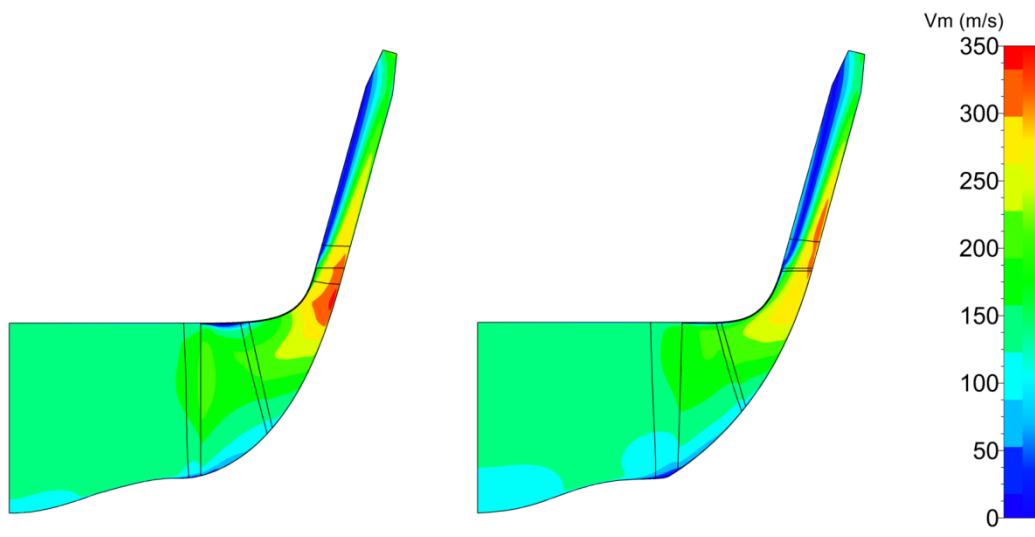


Figure 52: Meridional velocity contours of the CFturbo (left) and final design

Figure 53 compares the relative Mach number distribution of the CFturbo design and the final design in the B2B plane at 10% span. Similarly, the relative Mach number distribution is compared at 50% span in Figure 54.

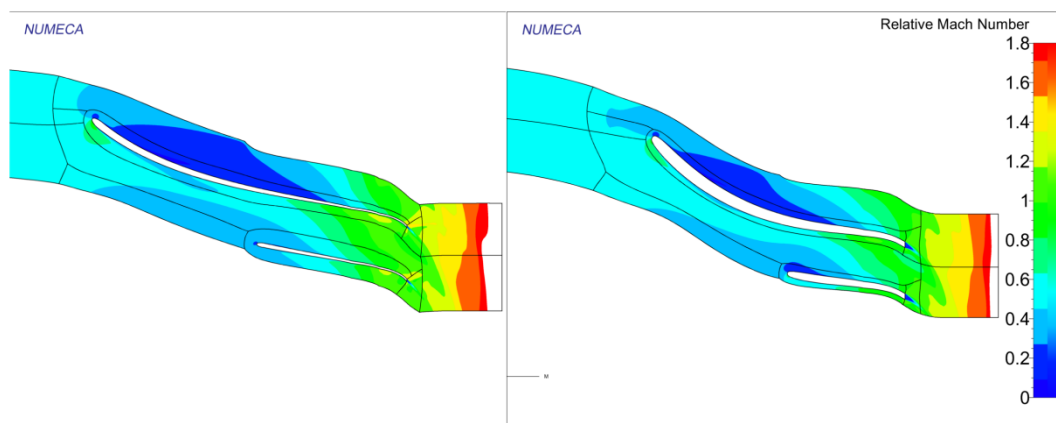


Figure 53: Relative Mach number contours at design conditions and 10% span of the CFturbo design (left) and the final design

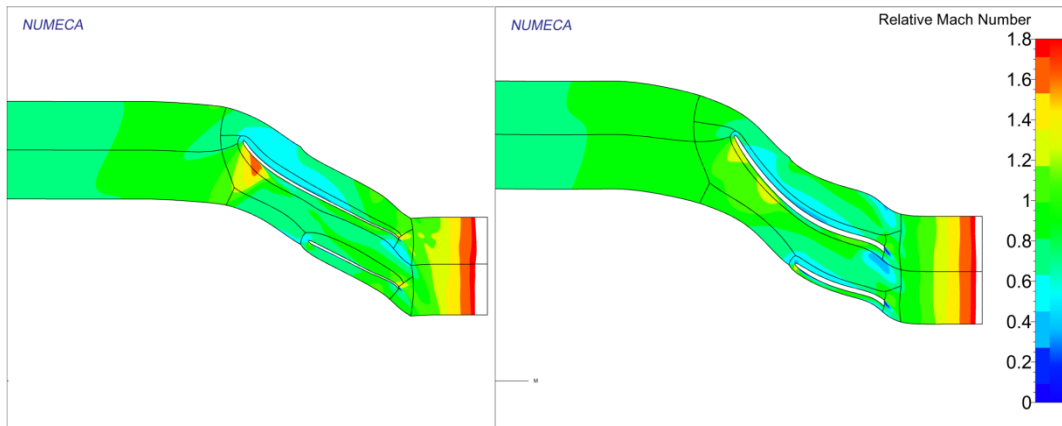


Figure 54: Relative Mach number contours at design conditions and 50% span of the CFturbo design (left) and the final optimized design

## **APPENDIX L: PROCESSOR MANAGEMENT AND CPU TIME**

### **L.1 CFD Database and Optimization**

#### **L.1.1 Database**

During the database generation one mesh took 25 minutes to generate. AutoGrid5<sup>TM</sup> can only be run sequentially, according to the AutoGrid5<sup>TM</sup> User's manual (NUMECA International, 2014d), hence assigning more cores did not help with the speed of meshing. The ruled surfaces were deemed responsible for the large amount of time taken for meshing. Completion of the three EURANUS jobs using parallel partitioning on each node (11 cores per node) on a LINUX cluster and the mesh consisting of 3-million cells took 94 minutes for the SP and DP (2400 iterations). The CP took 80 minutes (600 iterations, CPU boost). Parallel partitioning was necessary, since the number of cores exceeded the number of blocks in the mesh, making the parallel mode inefficient.

For DB03, with the new mesh template defining a 2.8 million cells mesh, the DP and SP took 71 minutes (2400 iterations). The CP took 35 minutes (300 iterations, CPU boost). The processors used were Intel XEON 5650 2.67 GHz with 6 physical cores (two processors on one mainboard makes 12 cores per node). Generating all three databases took 12.2 days.

#### **L.1.2 Optimization**

Completion of one optimization cycle using parallel partitioning on 3 nodes with 11 cores assigned to each job on a LINUX cluster took 3 hours. This includes mesh generation, ANN teaching and optimization with 50 GA optimizer steps. 2500 iterations plus the coarse grid initialization steps (total of 2800 iterations) of one DP and SP job on one node took 100 minutes. The CP took 80 minutes (2200 iterations). The new\_TE\_topology\_1 grid template was used, which consists of 2.8 million cells. The final optimization took 13.8 days.

Table 31: CFD database and optimization computational time

	CP	DP & SP	Database	Optimization
Old mesh	80 min	94 min	292 h (12.2 d)	-
New mesh	35 min	71 min		330 h (13.8 d)

## L.2 OOFELIE FEA

All FEA computations were run on a 4-core i7 (2.4 GHz) machine with 16 GB of RAM. According to the FINE<sup>TM</sup>/Design3D User's manual (NUMECA International, 2014e) the grid generation process is parallelizable. It was confirmed that assigning more cores to the grid generation task improved the speed of the grid generation. The available 4 cores were thus assigned to the grid generation process. Generating one grid with the given settings took 12 minutes.

PARDISO is a direct solver and thus has high memory demands. 10 GB of RAM were used for solving with a mesh size of 380k cells. It took 4 minutes to solve one FE geometry.

## L.3 Coupled Optimization

The same machine and processor settings as used for the mechanical optimization were utilized for the FEA in the coupled optimization. The CFD task was split into 4 parts, one for each processor core. The CP calculation took 72 minutes for 1000 iterations including multi-grid initialization.

## APPENDIX M: BLADE CAMBER ANGLE COMPARISON

The camber metallic angles of the initial, aero-optimized and final design are graphed in Figure 55. The angles are measured from the  $dm/r$  axis in the  $dm/r-\theta$  plane; a clock-wise measurement being negative.

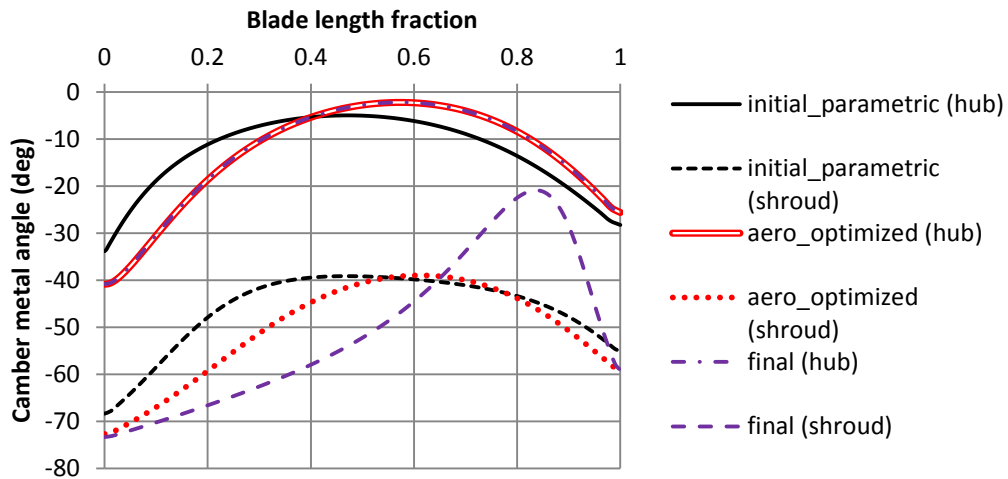


Figure 55: Blade camber angles of the initial, aero-optimized and aero-mechanically optimized design

**APPENDIX N: FINAL IMPELLER PERFORMANCE MAP**

CFD simulations of the final impeller design were completed at design speed of 95 krpm and three lower speeds in increments of 10 krpm. Results are shown in Figure 56.

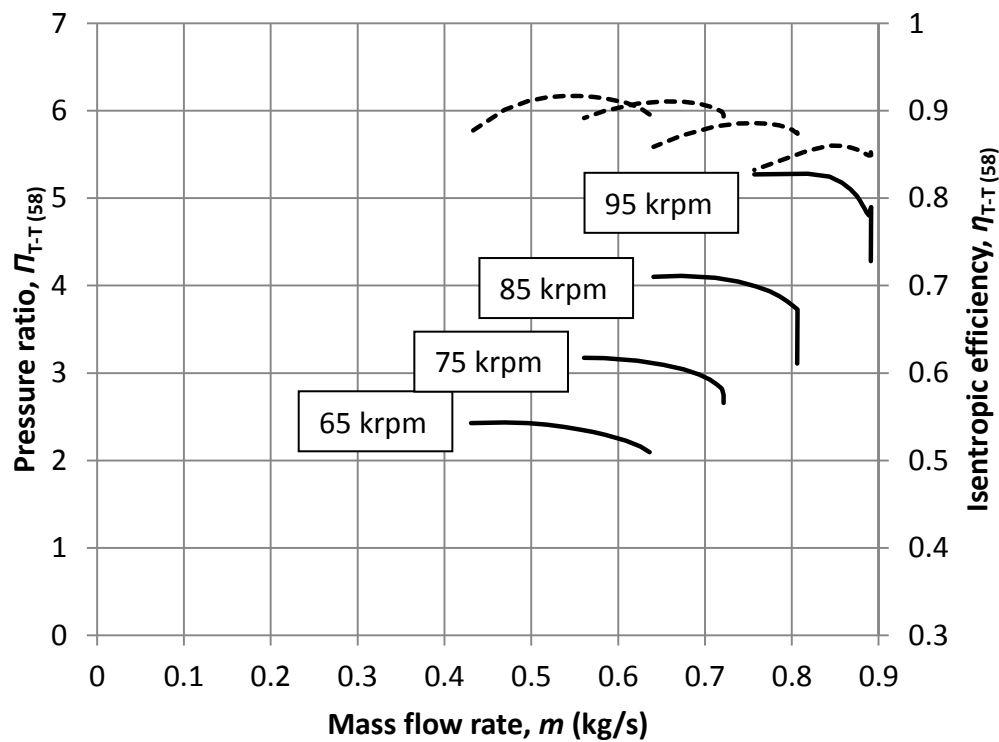


Figure 56: Compressor map of the final compressor impeller design

## APPENDIX O: INITIAL AND FINAL IMPELLER RENDER

Figure 57 and Figure 58 show 3-dimensional renderings of the baseline and final impeller design obtained in Autodesk Inventor.

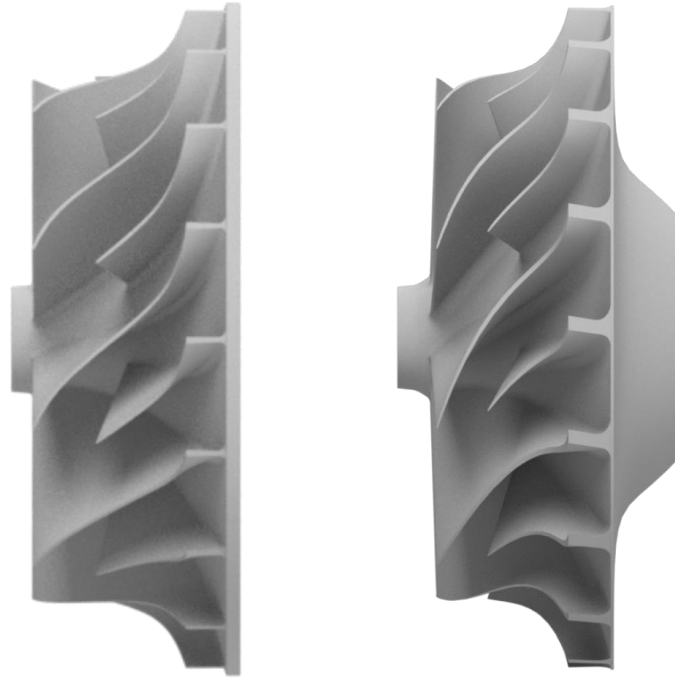


Figure 57: Side view of the baseline (left) and final impeller design (not to scale)

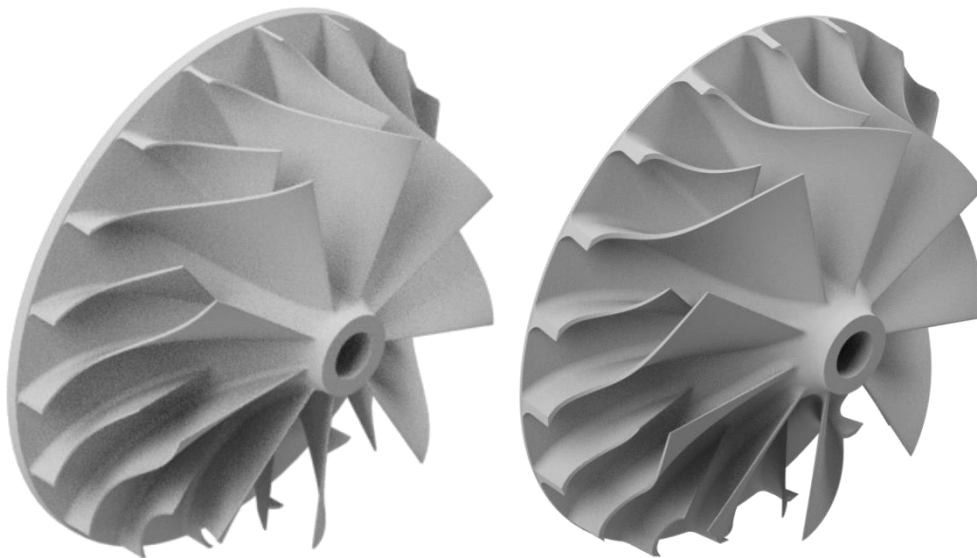


Figure 58: Isometric view of the baseline (left) and final impeller designs